ARO 24626.159-PH-UIR

(2)

ARO-URI Center for

OPTO-ELECTRONIC SYSTEMS RESEARCH

TECHNICAL REPORT

FABRICATION AND TESTING OF INDEX GRADIENTS IN FLUORIDE MATERIALS

Michael T. Houk

April 1990

The Institute of Optics
University of Rochester

Prepared for:

U.S. Army Research Office
ATTN: DRXRO-IP-Library
P. O. Box 12211
Research Triangle Park, NC 27709

FABRICATION AND TESTING OF INDEX GRADIENTS IN FLUORIDE MATERIALS

by

Michael T. Houk

Submitted in Partial Fulfillment
of the
Requirements for the Degree

DOCTOR OF PHILOSOPHY

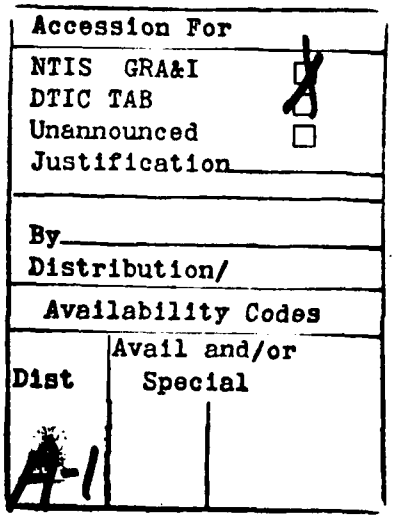

Supervised by
Dr. Duncan T. Moore
The Institute of Optics
College of Engineering and Applied Science

University of Rochester
Rochester, New York

1990

UNCLASSIFIED
SECURITY CLASSIFICATION OF THIS PAGE

REPORT DOCUMENTATION PAGE

1a. REPORT SECURITY CLASSIFICATION: Unclassified	1b. RESTRICTIVE MARKINGS
2a. SECURITY CLASSIFICATION AUTHORITY	3. DISTRIBUTION/AVAILABILITY OF REPORT: Approved for public release; distribution unlimited.
2b. DECLASSIFICATION/DOWNGRADING SCHEDULE	
4. PERFORMING ORGANIZATION REPORT NUMBER(S)	5. MONITORING ORGANIZATION REPORT NUMBER(S): ARO 24626.159-PH-UIR
6a. NAME OF PERFORMING ORGANIZATION / 6b. OFFICE SYMBOL (If applicable)	7a. NAME OF MONITORING ORGANIZATION: U. S. Army Research Office
6c. ADDRESS (City, State, and ZIP Code)	7b. ADDRESS (City, State, and ZIP Code): P. O. Box 12211, Research Triangle Park, NC 27709-2211
8a. NAME OF FUNDING/SPONSORING ORGANIZATION: U. S. Army Research Office / 8b. OFFICE SYMBOL (If applicable)	9. PROCUREMENT INSTRUMENT IDENTIFICATION NUMBER: DAAL03-86-K-0173
8c. ADDRESS (City, State, and ZIP Code): P. O. Box 12211, Research Triangle Park, NC 27709-2211	10. SOURCE OF FUNDING NUMBERS: PROGRAM ELEMENT NO. / PROJECT NO. / TASK NO. / WORK UNIT ACCESSION NO.

11. TITLE (Include Security Classification)

Fabrication and Testing of Index Gradients in Fluoride Materials

12 PERSONAL AUTHOR(S)

Michael T. Houk

13a. TYPE OF REPORT	13b. TIME COVERED	14. DATE OF REPORT (Year, Month, Day)	15. PAGE COUNT
Technical	FROM _____ TO _____	April 1990	189

16. SUPPLEMENTARY NOTATION

The view, opinions and/or findings contained in this report are those of the author(s) and should not be construed as an official Department of the Army position, policy, or decision, unless so designated by other documentation.

17. COSATI CODES			18. SUBJECT TERMS (Continue on reverse if necessary and identify by block number)
FIELD	GROUP	SUB-GROUP	Gradient index; fluoride materials

19 ABSTRACT (Continue on reverse if necessary and identify by block number)

Please see Abstract on page iv.

20. DISTRIBUTION/AVAILABILITY OF ABSTRACT ☐ UNCLASSIFIED/UNLIMITED ☐ SAME AS RPT. ☐ DTIC USERS	21. ABSTRACT SECURITY CLASSIFICATION: Unclassified
22a. NAME OF RESPONSIBLE INDIVIDUAL: Duncan Moore	22b. TELEPHONE (Include Area Code): 716-275-4922 / 22c. OFFICE SYMBOL

DD FORM 1473, 84 MAR — 83 APR edition may be used until exhausted. All other editions are obsolete.

SECURITY CLASSIFICATION OF THIS PAGE
UNCLASSIFIED

CURRICULUM VITAE

The author [redacted] After graduation from Bellevue High School in Michigan, he pursued a Bachelor of Arts degree from Kalamazoo College. He received the college's Hornbeck award for recognition of achievement in advanced physics studies and graduated with top honors from the physics department in 1982. After a brief respite as a custom woodworker, the author became a candidate for the Ph.D. degree in optics at the University of Rochester's Institute of Optics in 1983. He began his doctoral research in 1985 while holding departmental teaching and research assistantships and later held NYS CAOT and ARO-URI fellowships.

ACKNOWLEDGEMENTS

I am grateful to the following people for their ideas and contributions to this thesis, without them this work would not have been possible:

To Dr. Duncan T. Moore, my advisor, who provided me with the freedom of a well equipped lab and the encouragement to go wherever I thought the research led, while making his time and ideas available whenever I was stumped.

To Dr. Joe Miceli for his interest in my work, for his help in understanding the practicalities involved in actually growing a crystal, and for many helpful discussions on harmonic phase modulation.

To Brian McIntyre for his careful electron microprobe analyses of my crystals and for his many insightful comments and ideas on the subject of crystal growth (and on any other topic that I was willing to argue about).

To the entire GRIN group, especially Doug Kindred, Brian Caldwell, Ben Wooley, Leo Gardner, Dave Wang, and John Bowen, for their friendship and insightful discussions on everything ranging from the best way to coerce CODEV into optimizing realistic index gradients to the shortest distance from Palermo to La Zagarella.

To Dan Ouwleen, Scott Everts, Dave Lane, and the others at Kayex-Hamco of Rochester who donated the crystal growth equipment and their technical support, and who cheerfully answered my many questions about the CG800.

To the New York State Center for Advanced Optical Technology and the Army Research Office through its University Research Initiative for the generous funding I have received.

Beyond the technical contributions made by the people mentioned above, there are many others to whom thanks are due who have directly affected my life in a way that has made this work worthwhile and my life enjoyable even when things were tough.

I would like to thank my parents and family, who have loved me and encouraged me in all my endeavors, never doubting that I could finish whatever I started. I thank my in-laws for accepting me as one of the family and then supporting me in a way that only a loving family can do.

Thanks to the Rogers House community over the past four years for sharing themselves in a way that let me see myself more clearly, and for helping me to understand that God really is guiding my life.

Many thanks to Leah and Zachary who made it almost impossible to spend more than 10 hours a day in the lab and who, while doing so, made me realize more concretely that life doesn't have to be all optics.

Finally and most importantly, I would like to acknowledge the support that my wife, Marla, has given me. She has supported me by critically reading this manuscript, but more significantly, through her constant love and encouragement she has aided me in all aspects of this research in a way more encompassing and compassionate than could have anyone else. Thank you, Marla.

ABSTRACT

The feasibility of manufacturing and measuring gradient-index (GRIN) fluoride materials that transmit ultraviolet light is demonstrated. Conventional Czochralski crystal growing equipment is modified to allow controlled doping of the melt during the growth of a mixed crystal. This doping produces a composition that varies along the axis of the crystal in a predictable manner. Mixed barium fluoride and calcium fluoride crystals that transmit optical wavelengths to 210 nm are grown. The theory of crystal growth in conjunction with active doping is discussed and the appropriate equations governing the index profile as a function of growth parameters are derived. This method is of a general nature and is applicable to the production of controlled index gradients in a wide variety of materials whose phase properties include a solid solution.

In order to measure the index profiles in the ultraviolet region of the spectrum an achromatic moiré deflectometer is designed and built. To provide accurate phase information an automated phase retrieval scheme is implemented using a personal computer and the harmonic phase modulation method. The diffraction theory for the operation of the deflectometer is presented along with the theory of harmonic phase modulation that is used to extract phase information from the fringe pattern. An analysis of the effects of non-ideal phase modulation is also presented. Measurements of the index profiles of several GRIN materials are made at wavelengths from the visible to the UV and the results are presented with a discussion of possible sources of error and their removal or compensation. Calculation of the dispersion number of GRIN materials is carried out for two different types of materials and the results are compared with the theoretical predictions.

A highly non-linear gradient dispersion in the ultraviolet region of the spectrum presents difficulties when correcting chromatic aberrations. The use of a chromatic coordinate representation of the index of refraction is shown to be adaptable for GRIN materials and its use in designing achromatic singlets is demonstrated using Robb's graphical method.

TABLE OF CONTENTS

CHAPTER 4
GRIN Crystal Growth Results

CHAPTER 5
Deflectometer Theory

CHAPTER 6
Results of Measurements using the Moiré Deflectometer

CHAPTER 7
Conclusions and recommendations for future work

APPENDIX A
Growth procedures using the CG800

APPENDIX B
The Use of Chromatic Coordinates in Describing the Chromatic Properties of GRIN Materials

LIST OF FIGURES

LIST OF TABLES

CHAPTER 1

Introduction

1.1 Gradient-Index materials

Gradient-index (GRIN) materials are those materials in which the index of refraction varies in some prescribed manner as a function of position. The existence of GRIN optics in nature has been documented since the late 1800's when Exner[1] showed that the eyes of some insects contain GRIN elements. Since that time it has been recognized that GRIN optics exist in nature as components of the eyes of many higher creatures, including humans. The use of GRIN materials in commercial optical systems, however, is a fairly recent development, beginning with the SELFOC® rod, manufactured by Nippon Sheet Glass in the early 1970's. These rods are glass cylinders in which resident ions of thallium have been replaced by ions of potassium through a diffusion process carried out at a temperature near the softening point of the glass. This change in composition produces a corresponding change in the index of refraction, which varies as a function of the radial coordinate. More recently relatively large aperture glass singlets have been made commercially available by Gradient Lens Corp., again utilizing an ion diffusion process as the source of the index gradient, but with an index profile that varies as a function of distance along the optical axis.

This thesis is primarily concerned with the fabrication of gradient-index materials with a spectral transmission that extends into the near ultraviolet (uv) region of the spectrum. No previously existing materials in which index-gradients have been fabricated transmit uv wavelengths. The spectral transmission of optical glasses and GRIN materials fabricated from them is limited mainly to the visible and the near infrared (ir) regions of the spectrum. Several programs have been successfully carried

out to produce ir transmitting GRIN materials. Examples are Ge/Si alloys fabricated by J. J. Miceli[2] through a crystal growth process and ZnS/ZnSe[3] index gradients fabricated using a chemical vapor deposition process. One goal of this thesis is to carry out an investigation into a process and materials through which it is possible to fabricate uv transmitting index-gradients and to demonstrate the feasibility of this process.

1.1.1 Mathematical representation of the index profile

The index of refraction in a GRIN medium can be represented as a polynomial using the "University of Rochester" notation, as

$$\begin{aligned} N(\rho,z) &= N_{00} + N_{01}z + N_{02}z^2 + \ldots \\ &+\rho^2\left[N_{10} + N_{11}z + N_{12}z^2 + \ldots\right] \\ &+\rho^4\left[N_{20} + N_{21}z + N_{22}z^2 + \ldots\right] \\ &\vdots \end{aligned} \quad , \qquad (1.1)$$

where z is the direction parallel to the optical axis and ρ is the radial coordinate measured perpendicular to the z axis.

For the majority of applications gradient-index profiles fall into either of two categories, those dependent on the z coordinate only, known as axial gradients, and those dependent solely on the radial coordinate, known as radial gradients. Schematic examples of these two types of gradients are shown in fig. 1.1, where the dashed lines indicate the position of isoindicial surfaces. These surfaces of constant index are planes for the case of axial gradients and coaxial cylinders in the case of radial gradients.

1.1.2 Design advantages of GRIN elements

The effect of an axial gradient when it intersects the curved surface of an optical element is very similar to that of a homogeneous aspheric surface, due to the varying refractive power of the surface as a function of aperture. This effect can be used to control spherical aberration[4] or coma, for example. An additional advantageous aspect

of the axial gradient is the small chromatic effect it has, not found in aspheric surfaces, which can be used in balancing chromatic aberrations[5].

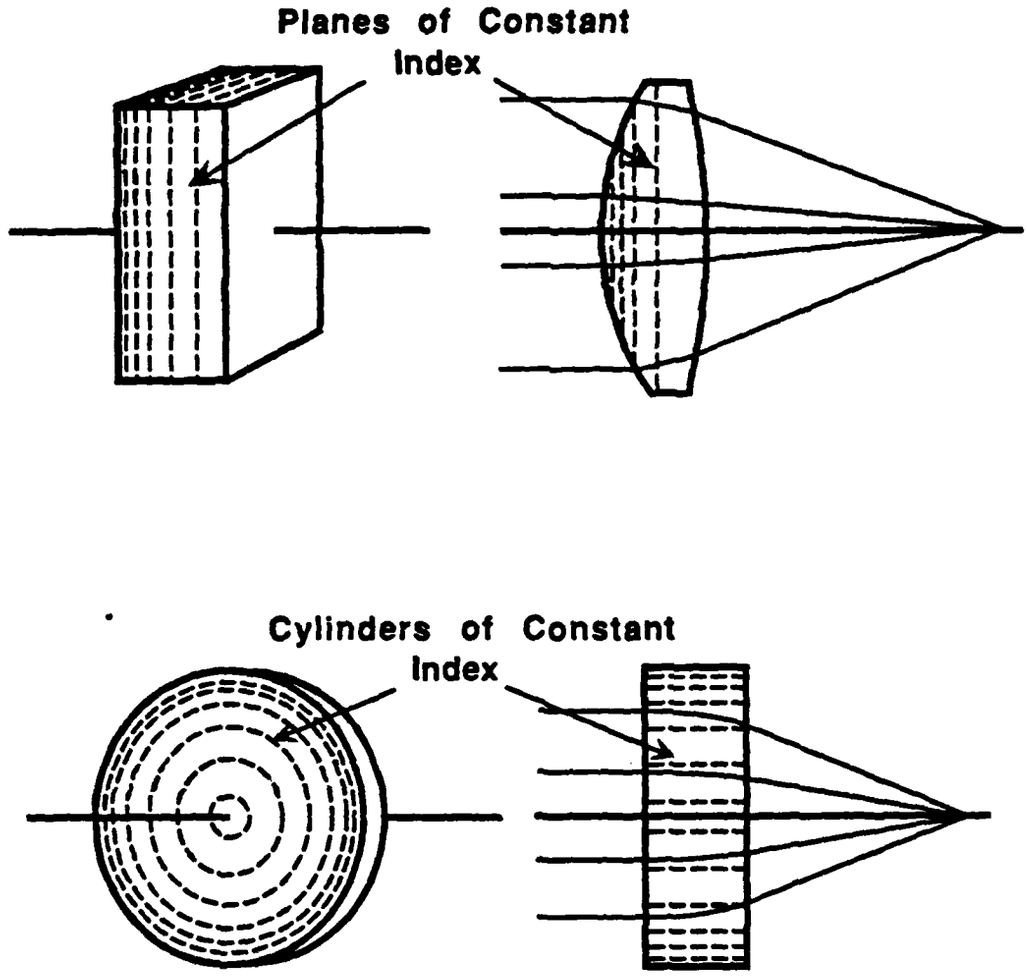

Figure 1.1
Schematic figures of axial (top) and radial (bottom) gradients and example lenses utilizing them. The axial gradient in conjunction with a spherical surface has an effect similar to that of an asphere. The radial gradient has optical power and can be used in elements with plano surfaces to focus light.

Radial gradient GRIN rods are the most widely used commercial GRIN elements. These rods are used singly in endoscopes and grouped in linear arrays for

imaging wide fields over short conjugates, as in compact photocopiers and facsimile machines. Because the radial index gradient has optical power, the ends of the GRIN rod can be plane parallel, in contrast to the conventional homogeneous lens which must have curved surfaces in order to focus light.

Both types of gradients have been shown to provide useful degrees of freedom in the design of optical systems. It is often possible to reduce the number of elements and/or increase the performance in an optical design by using one or more GRIN elements[6]. This has been demonstrated in the design of photographic objectives[7], zoom lenses[8], and many other optical systems[9].

More general types of GRIN index profiles have also been shown to be useful in specific cases. Examples of these profiles are tapers[10], in which the surfaces of constant index are concentric cones, or anamorphic radial gradients[11], in which the surfaces of constant index are ellipses. These have applications in fiber coupling and laser diode coupling, respectively.

Recently, systems have been fabricated utilizing GRIN elements other than the aforementioned SELFOC rod. These systems include binocular objectives[12], in which an axial gradient was used to reduce the number of elements and compact disc lenses[13], utilizing radial gradients.

A more complete coverage of GRIN systems and the mathematical methods for their analysis can be found in the books by Marchand[14] and Iga[15], and the review by Moore[16], also see recent work by Caldwell[17] and Wang[18] for general GRIN design "rules".

There are many applications that involve the use of ultraviolet transmitting optics that would benefit from the availability of ultraviolet transmitting GRIN materials. A current example is the lenses used in high resolution optical lithography.

The lithography industry is continually attempting to increase the resolution of the images made during the exposure of photoresist. One method of achieving this is to decrease the wavelength at which the exposure is made and to increase the numerical aperture. This implies either a complex achromatic optical system or a slightly less complex monochromatic one. Currently, to achieve linewidths as small as 0.5 μm, optical lithography steppers are being manufactured that operate at wavelengths from 404[19] nm to below 300 nm and require the use of very narrowband sources such as a stabilized KrF laser[20]. This application could benefit from the existence of a GRIN material that transmitted in this spectral region, both through the possible reduction in complexity of the lenses and through the possibility of achromatic operation over a bandwidth that would allow the use of non-stabilized ultraviolet sources. Other applications involving ultraviolet transmitting optics include spectral measurements of stellar objects, atmospheric spectroscopy, and ultraviolet microscopy.

1.2 Materials for the ultraviolet

Many materials exist that transmit in the visible portion of the spectrum, but very few of these transmit to any degree in the ultraviolet (uv). Optical glasses, with a few exceptions[21], do not transmit significantly below 350 nm. Materials that are transparent in the uv include quartz (or fused silica), sapphire, barium fluoride, calcium fluoride, strontium fluoride, and many of the alkali halides. Figure 1.2 shows transmission ranges both for these materials and for materials in which index gradients have previously been made.

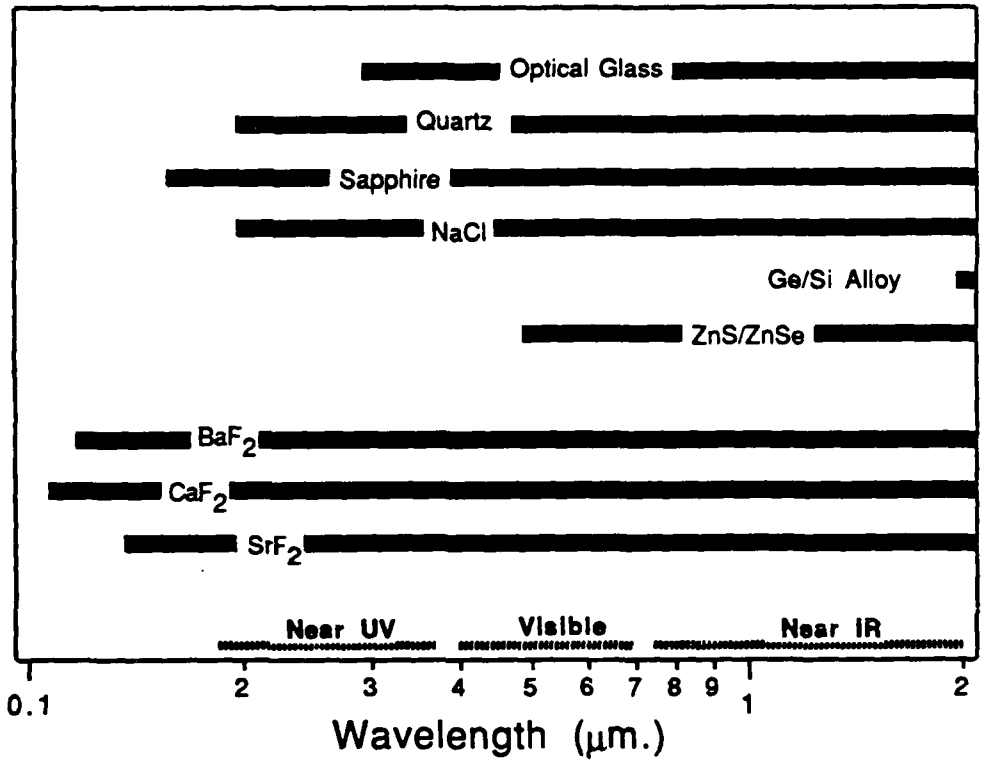

Figure 1.2
Spectral transmission for some representative optical materials with near uv transparency and some GRIN materials.

The first goal of this thesis was to discover materials in which uv transmitting index gradients could be fabricated which would be useful as lens materials. Not all of the above uv transmitting materials have desirable mechanical and chemical properties. The alkali halides tend to be soft and are often water soluble or even hygroscopic, and thus are eliminated from consideration. Optical glasses with any appreciable uv transparency[22] are not of a type in which ion diffusion is a possibility, or at least not with present techniques[23]. It is the fluorides which are the most interesting from a materials and optical properties standpoint.

Calcium fluoride, or fluorite, despite its low index of refraction, has been used extensively in microscope objectives[24] because of its transparency and low dispersion

(Abbe number of approximately 92) in the visible. It was also used as a prism material for vacuum uv spectrometers because it is very dispersive in the uv. Its use in large instruments was limited by the availability of naturally occurring large pieces. Such was the case until the advent of long focal length reconnaissance cameras during World War II made the production of large artificial fluorite a wartime priority. The dispersive properties of fluorite were needed to reduce the chromatic aberrations that limited the cameras' resolution. It was through research efforts at this time, both in the US and in the USSR, that large artificial fluorite crystals were first produced. D. Stockbarger[25] was the first to discuss methods and results for the growth of large artificial fluorite.

It was also at this time that barium fluoride began to be used as an optical material due to its similar properties and higher index of refraction. Barium fluoride does not occur naturally in any significant quantity and had escaped the interest of the optical community until it was produced artificially by the Stockbarger process.

1.3 Methods of growing crystals

There exist many different methods for producing crystals of any given material. The most common methods can be divided into two types: solution growth and melt growth. Solution growth involves the formation of the crystal from a saturated solution. Melt growth is the formation of the crystal by freezing from a molten liquid. Types of melt growth include Verneuil flame, Bridgman-Stockbarger, Kyropoulos, Czochralski, and zone melting. The types of growth most suitable for the production of optical quality crystals are the Bridgman-Stockbarger, zone melting, and Czochralski (or crystal pulling) methods. Each involves the formation of a crystalline structure onto a cooled seed of the same material placed in the melt (in some cases the seed is the first part of the melt that freezes).

Miceli[26] and Naughton[27] used the Czochralski process to grow mixtures of germanium and silicon. Their work took advantage of the natural tendency of one component of a mixed melt to solidify at a higher concentration in the crystal than its concentration in the melt. This tendency is known as segregation[28] and it occurs during the crystallization of mixtures of many different materials, including mixtures of barium fluoride and calcium fluoride. The result of this segregation is a compositional change along the growth direction of the crystal and, in most cases, a corresponding change in the index of refraction.

The major experimental work in this thesis involves the growth of Ba/CaF_2 mixtures for the fabrication of uv transmitting gradients. This thesis expands on the work of Miceli and Naughton not only through the use of a different material but also through the modification of a Czochralski crystal grower to allow the active doping of the melt. Active doping of the melt allows an additional degree of control over the concentration profile in the growing crystal and thus additional control over the index profile.

1.4 Measurement of the GRIN profile

Once a gradient has been fabricated there remains the problem of accurately measuring the index profile and its dispersion, or variation with wavelength. These measurements are necessary so that the optical designer has information on which to base the design of lenses and optical systems. Most precision measurements of index of refraction profiles have been carried out by placing a transverse (with respect to the direction of the index gradient) plane-parallel section of the sample in the reference arm of a Mach-Zehnder interferometer[29]. The fringe pattern viewed in the output of the interferometer is a contour map where each interference fringe corresponds to a line of constant index of refraction. The analysis of the fringe pattern for conversion to change

in index of refraction values is thus quite simple. The addition of a.c. techniques such as phase-locking[30] or N-bucket[31] phase stepping, along with computer based data acquisition and control have made analysis of fringe patterns quick and very accurate.

Because the main thrust of this thesis involves materials that transmit over a wide spectral range, it is a goal that measurements of the index profile will be carried out over a correspondingly large spectral range. There are several drawbacks to the use of a conventional interferometer for measurements over a wide spectral range that includes the uv. The first is that alignment is very difficult when the wavelengths used are outside the visible. Other minor difficulties include locating (and purchasing) light sources with sufficient temporal coherence at the desired wavelengths and designing wideband coatings for beamsplitters and other optics. The second major problem with a conventional interferometer is that when some type of phase modulation is used to accurately recover the phase, the modulation amplitude is based on the wavelength of the light. Because different wavelengths are used in a series of measurements on a sample, the phase modulation must then also be changed for each wavelength change.

An alternative method exists that involves the use of Ronchi rulings (or Ronchi gratings) that is simple to use and is independent of wavelength. The use of gratings in optical testing has a long history. The first "grating interferometer" was set up and used by V. Ronchi in 1922[32] to test the quality of optical mirrors for astronomical telescopes. Now known as the Ronchi test, it consists of placing a coarse grating at the center of curvature of the mirror to be tested. If the mirror is not perfect, an observer looking through the grating towards the mirror sees a fringe pattern on the surface of the mirror. Deviations of the mirror surface from the ideal cause the grating image to be distorted. The pattern seen by the observer is the moiré pattern formed by the superposition of the grating and its own distorted image[33].

Several authors have proposed the use of moiré techniques for the measurement of GRIN materials[34,35] (often liquid solutions). These techniques involve the placement of the sample to be measured between two Ronchi rulings or gratings and measuring the moiré fringe pattern that is formed. It can be shown that the fringe pattern is independent of the wavelength used, except for the dependence of the index gradient on wavelength. Similar techniques have been used in the field of mechanical engineering for the measurement of strain[36]. The advantages of this technique lie in its simplicity, in the ability to apply a.c. techniques for accurately recovering the phase of the fringe pattern, and in its independence from the illuminating wavelength.

This moiré technique is adapted in this thesis for the measurement of GRIN samples very accurately over a wide spectral range, from the uv to the near infrared. The data gathered using this technique is also used to calculate the dispersion of the GRIN index profile for several GRIN materials.

References for Chapter 1.

---

[1]S. Exner, *Die Physiologie der Facettierten Augen von Krebsen und Insekten*, Granz Deutiche, Leipzig und Wein (1891).

[2]J. J. Miceli, *Infrared Gradient-Index Optics: Materials, Fabrication, and Testing*, Ph.D. thesis, University of Rochester, 1982.

[3]M. A. Pickering, R. L. Taylor, and D. T. Moore, "Gradient Infrared Optical Material Prepared by a Chemical Vapor Deposition Process," Appl. Opt. **25** (1986) 3364.

[4]D. T. Moore, *Aberration Correction Using Index Gradients*, M.S. thesis, University of Rochester, 1971.

[5]D. S. Kindred and D. T. Moore, "Design, Fabrication, and Testing of a Gradient-Index Binocular Objective," App. Opt. **27** (1988) 492.

[6]D. T. Moore, *Gradient-Index Optics: Aspects of Design, Testing, Tolerancing, and Fabrication*, Ph.D. thesis, University of Rochester, 1974.

[7]L. G. Atkinson, S. N. Houde-Walter, D. T. Moore, D. P. Ryan, and J. M. Stagaman, "Design of a Gradient-Index Photographic Objective," Appl. Opt. **21** (1982) 993.

[8]D. Wang, University of Rochester, unpublished work, and Pat. No. 4,776,679, "Objective of Variable Focal Length," assigned to Canon of Tokyo (Oct. 11, 1988).

[9]Any review of the recent optics patent literature will yield many inventions based on GRIN technology. For example, Pat. No. 4,702,568 "Photographic Lens with Large Aperture Ratio," assigned to Asahi, of Tokyo (Oct. 27, 1987).

[10]J. N. McMullin, "The ABCD Matrix in Graded Index Tapers Used for Beam Expansion and Compression," Appl. Opt. **28** (1989) 1298.

[11]J. M. Stagaman, *Anamorphic Gradient-Index Lens Systems*, Ph.D. thesis, University of Rochester, 1985.

[12]D. S. Kindred and D. T. Moore, op. cit.

[13]H. Nishi, H. Ichikawa, M. Toyama, and I. Kitano, "Gradient-Index Objective Lens for the Compact Disk System," Appl. Opt. **25** (1986) 3340.

[14]E. Marchand, *Gradient-Index Optics*, Academic Press (1978).

[15]K. Iga, *MicroOptics*, Academic Press (1985).

[16]D. T. Moore, "Unusual Optical Forms", in *Geometrical Optics*, Proc. SPIE **531** (1985) 256.

[17]J. B. Caldwell, *Sol-Gel Methods for making Radial Gradient-Index Glass*, Ph.D. thesis, University of Rochester, 1989.

[18]D. Wang, "Third Order Aberrations of Thin GRIN Lenses," presented at the Eighth Topical Conference on Gradient-Index Imaging Systems, Kobe, Japan (1989).

[19]J.D. Buckley, "An Advanced H-Line Stepper," Sol. St. Tech. (1987) 87.

[20]V. Pol, "High Resolution Optical Lithography: A Deep Ultraviolet Laser-Based Wafer Stepper," Sol. St. Tech. (1987) 71.

[21]*Optical Glass Catalog*, Schott Glass Technologies, Inc., Duryea, Pa.

[22]T. S. Izumitani, *Optical Glass*, Am. Inst. Phys., New York (1986) 33.

[23]D. S. Kindred, University of Rochester, private communication.

[24]W. J. Smith, *Modern Optical Engineering*, McGraw-Hill, New York (1966).

[25]D. C. Stockbarger, "The Production of Large Artificial Fluorite Crystals", in *Crystal Growth, Discussions of the Faraday Society*, (1949).

[26]J. J. Miceli, op. cit.

[27]D. Naughton, *Fabrication and Testing of Infrared Gradient-Index materials*, M.S. thesis, University of Rochester, 1986.

[28]W. F. Pfann, *Zone Melting*, 2nd ed., J. Wiley and Sons, New York (1966).

[29]D. T. Moore, Ph.D. thesis (ref. 6).

[30]G. W. Johnson, D. C. Leiner, and D. T. Moore, "Phase-Locked Interferometry," Opt. Eng. **18** (1979) 46.

[31]J. H. Bruning, D. R. Herriot, J. E. Gallagher, D. P. Rosenfeld, A. D. White, and D. J. Brangaccio, "Digital Wavefront Measuring Interferometer for Testing Optical Surfaces and Lenses," Appl. Opt. **13** (1974) 2693.

[32]V. Ronchi, "Forty years History of a Grating Interferometer," Appl. Opt. **3** (1964) 437.

[33]*Optical Shop Testing*, D. Malacara (ed.), J. Wiley, New York (1978).

[34]Y. Nishijima and G. Oster, "Moiré Patterns: Their Application to Refractive Index and Refractive Index Gradient Measurements," JOSA **54** (1963) 1.

[35]Y. Nakano and K. Murata, "Measurements of Phase Objects Using the Talbot Effect and Moiré Techniques," Appl. Opt. **23** (1984) 2296.

[36]E. M. Weissman and D. Post, "Moiré Interferometry Near the Theoretical Limit," Appl. Opt. **21** (1982) 1621.

CHAPTER 2

The Theory of GRIN Crystal Growth

2.1. Introduction

The purpose of this chapter is to provide a theoretical basis from which to understand the processes that take place during the growth of gradient index fluoride crystals. The first section of this chapter describes the processes that occur on a macroscopic scale during the process of crystal growth from a doped melt. While examining the growth on a microscopic scale is vital to understanding effects such as lattice defects, formation of facets, or diffusion in the solid, a broad understanding of what happens during growth can be explained using macroscopic processes. When a binary melt freezes the phase changes and physical processes that occur are very complex, especially if the melt/crystal system is not a closed system. As freezing occurs one component may be either preferentially rejected or accepted into the growing crystal. If this segregation is partial and not complete, and there exists some solubility of one component in the other, a single phase mixture may form. This can lead to the formation of a gradient in composition and is the means by which gradient crystal alloys have been fabricated for the ir in semiconductor materials. The family of IIa fluorides - Ca, Ba, and Sr fluoride, show extensive segregation in their binary alloys. This, in combination with these materials' transparency in the ultraviolet and their generally good optical and mechanical properties, indicates that they are candidates for the fabrication of uv GRIN optical elements.

Understanding the phase diagrams for binary melts of fluorides is the first step toward understanding what happens during freezing. While much of the discussion on freezing and segregation is of a general nature and can be applied to situations involving

growth from the molten phase, the Czochralski process, or pulling from the melt, is the method used in this research and is of primary interest. The equations governing concentration profiles for crystals pulled from a binary melt are examined and previous research is reviewed.

Segregation is the effect of rejection of dopant by the growing crystal. In the Czochralski process the melt surface is accessible where it is not covered by the growing crystal. This makes controlling the concentration of some component in the melt relatively easy by directly adding dopant to the melt. In this way concentration changes either greater than or less than the normal concentration changes that occur because of segregation can be realized.

The last part of this chapter deals with defining the related rate equations governing the dopant concentration and finding either analytical solutions or computational schemes for dealing with them. The situation becomes quite complex when the diameter of the crystal is not constant, the solvent and solute have different densities and the segregation is a function of composition. The analysis presented here takes into account the effect these parameters have on the growth.

2.2. Methods of crystal growth

There are four major types of growth from the molten state that are satisfactory for the growth of fluoride crystals. They are the Kyropoulos, zone melting, Bridgman-Stockbarger, and Czochralski methods. Figure 2.1 shows schematics for each of these types of melt growth. In the Kyropoulos method a seed is brought into contact with the melt and allowed to melt slightly then a small neck is grown by slowly lifting the seed. At this point lifting ceases (or proceeds very slowly) and the temperature is gradually lowered while growth proceeds in a roughly hemispherical shape, along surfaces of constant temperature. This procedure is used to grow large crystals with a large

diameter to length ratio. The final crystal has a shape similar to the crucible but is somewhat smaller. It is important that the density of the solid be higher than that of the liquid so that the melt level drops, otherwise the crystal would grow outward and come into contact with the crucible. Another problem with this method is the large curved growth interface, which has many crystal faces, leading to strains and irregular growth in the presence of impurities. Typically this method is used to grow large (>20 kg) alkali halide crystals for optical uses in the IR (for example, large NaCl windows) where microscopic irregularities are not a problem.

The Bridgman-Stockbarger process consists of lowering a crucible through a sharp temperature gradient existing from temperatures above the melting point to temperatures below it. In this way the melt solidifies from the bottom up. Typical rates of travel are 1 to 30 mm/h. By shaping the crucible so that only a small region crystallizes first, the probability that the rest of the melt crystallizes with a single orientation is increased. This is usually accomplished by forming the bottom of the crucible into a conical shape. The freezing isotherm can be made to move through the molten charge in several different ways. One method is to move the crucible through a stationary heater, another is to move the heater along the crucible or to vary the power along the length of the heater as a function of time. This method has been the primary means of producing fluorite crystals since the 1930's and is still in extensive use today[1].

An important variation on the Bridgman process is the zone melting process described in detail by Pfann[2]. In the zone melting method the crucible or "boat" is placed with its long axis oriented horizontally while a short molten zone, which is smaller in length than the charge, traverses the length of the crucible. If the crystallizing solid preferentially accepts or rejects an impurity, the effect of the traveling

zone is to purify the charge by redistributing the impurity. Multiple passes of the molten zone

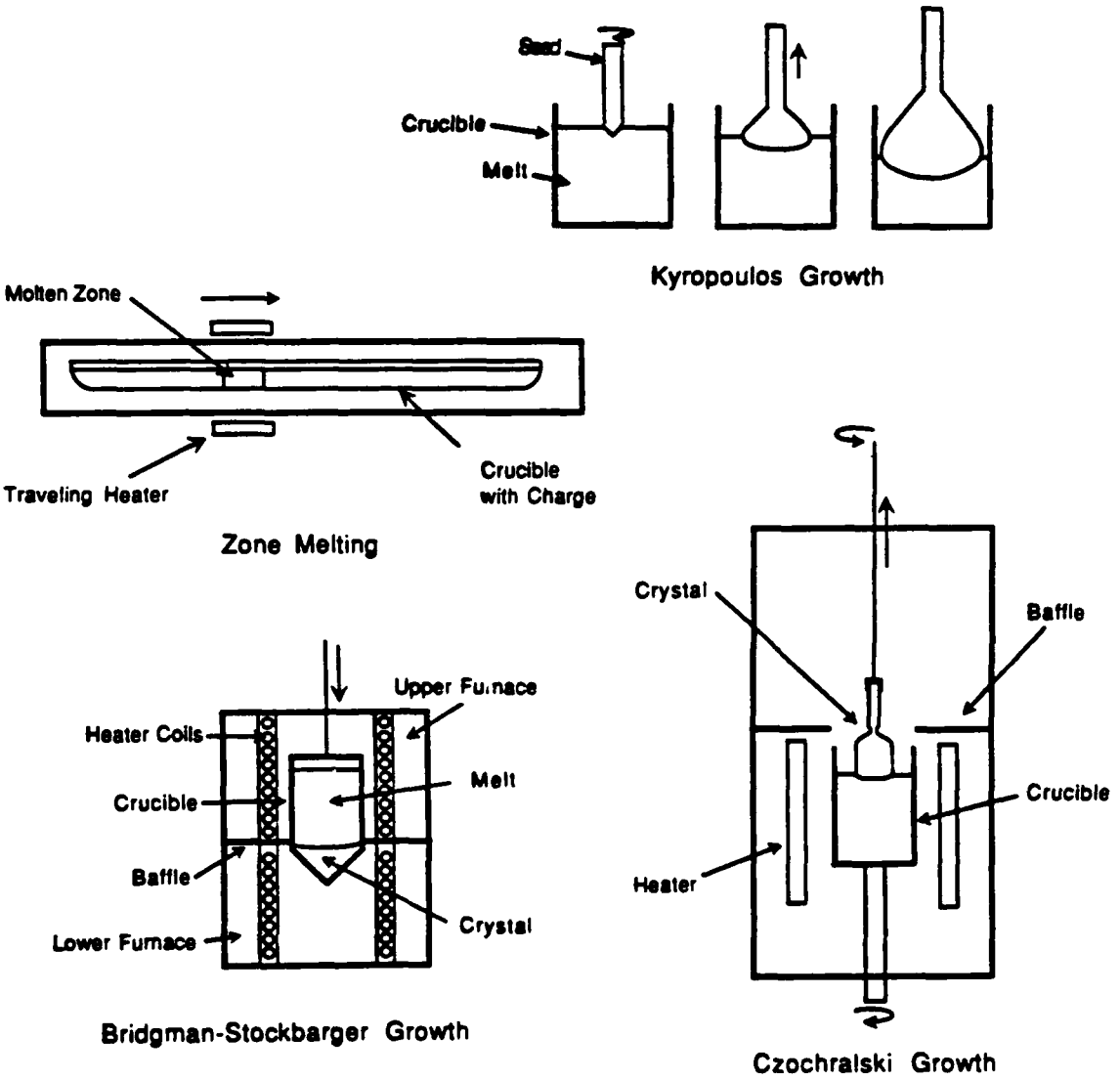

Figure 2.1
Various methods of crystal growth from the melt.

are used to highly refine some types of materials. The physical cause of this refining will be discussed in some detail later in this chapter, as it is an important mechanism in the formation of gradient index crystals.

The fourth method, and the one used in the research reported in this thesis is Czochralski's method, also known as pulling from the melt. Originally used in the study of crystallization of metals, it is similar in configuration to the Kyropoulos method but is more likely to produce a higher quality crystal[3]. A rotating seed is lowered into contact with a molten charge in an open crucible. The seed melts slightly and as heat flows up the seed growth begins. The seed is then raised. By varying the seed lift rate and the temperature of the melt, the desired diameter can be reached, usually after a thin neck is grown to increase the chances that only a single crystallographic orientation will grow. (Appendix A gives detailed procedures on the use of the Czochralski growth apparatus.) The limiting factor in the growth of larger diameter crystals by the Czochralski method is the large thermal gradient which can occur, causing strain and variations in the melt/solid interface. This is the most widely used method for growing silicon for the semiconductor industry where crystalline perfection is critical.

A feature of Czochralski growth that is important to this thesis is that the melt surface is readily accessible. The ability to access the melt surface for the addition of dopant is crucial if the melt is to be continuously doped during the growth of the crystal.

2.3. Criteria for GRIN crystal formation

This section describes the criteria for a binary alloy pulled from the melt to have a smoothly varying composition change. In most of the discussion that follows on freezing, it is easiest to picture a long cylinder of liquid freezing from one end, so that at any time the frozen part may be removed as a single piece. (It is assumed that diffusion in the solid is very slow or non-existent, which is the case for most ionic crystals, in which the ions are tightly bound.) This is described by Pfann as "normal" freezing and is analogous or equivalent to many crystal growth processes, especially to zone melting or Czochralski growth, where the grown crystal no longer interacts with, and is considerably cooler than, the melt.

In order to grow a crystal with a smoothly varying compositional change from a mixture of two components, it is necessary to understand the properties of the materials involved, both as a function of composition, and as a function of temperature, as they freeze from the molten state. The composition of the freezing solid depends on the composition of the melt and its constituents' phase properties relative to each other. Given that a melt consists of two species, a solvent compound and a solute compound, a crystal grown from such a melt is not necessarily uniform in composition. The crystal may reject the solute entirely, or it might consist of regions of one composition surrounded by a matrix of another composition, as is often the case with crystals grown from eutectic composition melts.[4] Another possibility is that the solute will be incorporated into the growing crystal in some other form, either through the formation of an intermediate compound, or as a solid solution. The latter is the situation desirable for the fabrication of index gradient materials. A solid solution is, just as it sounds, a homogeneous mixture of solute and solvent that exists as a crystalline phase. If this solid solution can be formed over some range in solute concentration, then the

possibility exists of fabricating a crystal with a smooth spatially varying composition and, if the index of refraction changes with composition, an index gradient.

2.3.1. Phase diagrams

A phase diagram shows which phases (solid, liquid, vapor) are present in a particular system as a function of temperature, pressure, and composition. These diagrams are usually determined by melting or freezing the compound of interest in a controlled system at near equilibrium conditions and carefully recording the temperature. The heat absorbed or released as a phase change occurs manifests itself as a discontinuity in the derivative of the temperature profile. This information, along with the help of relations derived from thermodynamic principles, gives insight into the phase state of the compound. Direct measurements of the crystalline phases present can also be made using x-ray diffraction[5]. Although pressure is an important parameter in the state of a compound, for most materials the placement of the phases are not significantly changed for pressures near one atmosphere. The fluoride phase diagram that is shown in this thesis is given as a function of temperature and composition with the pressure understood to be one atmosphere. Phases are shown on the diagram as labeled regions with solid lines separating different phases. The existence of a solid solution shows on the phase diagram as an intermediate region between liquid and solid phases. In most binary melts the solid that forms as the temperature is lowered is either an intermediate compound or pure crystal of solvent or solute. For a binary melt whose phase diagram exhibits a region of solid solution, the solid that forms depends primarily on the initial melt composition and the amount of segregation.

2.3.2. Fluoride materials' properties

By examining the phase diagrams for binary fluoride systems, it can be determined which composition regions are suitable for growing gradient-index crystals, with the priority being on solubility.

2.3.2.1. Solubility extent

Numerous theories and rules have been advanced to predict the solubility of one compound in another. The most straightforward is the Goldschmidt rule. The Goldschmidt rule states that a solid solution cannot form if the ionic radii differ by more than 15%. This rule is generally accepted for metal alloys. At first this would appear to preclude the possibility of substituting calcium ions for barium ions (0.99 Å and 1.15 Å, respectively). Fortunately this rule is not necessarily as true for inorganic solid solutions as it is for metals. The important parameter for inorganics is the specific volumes of the mixed substances. For example CaO and MgO exhibit limited solubility in each other even though Ca and Mg ions have radii of 0.99 Å and 0.65 Å (>15% difference)[6]. The lattice parameters of CaF_2 and BaF_2 are 5.464 A and 6.2001 Å, respectively, indicating that there is a region of solubility for each. Lanthanum fluoride, with an index greater than 1.6, also forms solid solutions with BaF_2 and CaF_2, but is birefringent. Other elements in the Lanthanide series (Eu, Ho, Gd) form solid solutions with either BaF_2 or CaF_2 but do not transmit in the ultraviolet. The figure on the next page shows the phase diagram for barium and calcium fluoride[7]. The vertical axis is temperature and the horizontal axis shows increasing concentration (as a mole fraction) of calcium fluoride. There are two regions of solid solution at either end of the diagram, so that one would expect to get a single phase mixture of barium/calcium fluoride in crystals grown from compositions in these regions.

One would then expect that either Ba rich or Ca rich solid solution fluorides could be grown. There appears to be some question as to the extent of the solubility of these two fluorides in each other. This phase diagram contradicts the diagram published two years earlier by M. Rolin and M. Clausier[8]. Their data indicated no solubility of BaF_2 in CaF_2. E. G. Chernevskaya and G. V. Ananeva[9] indicate that

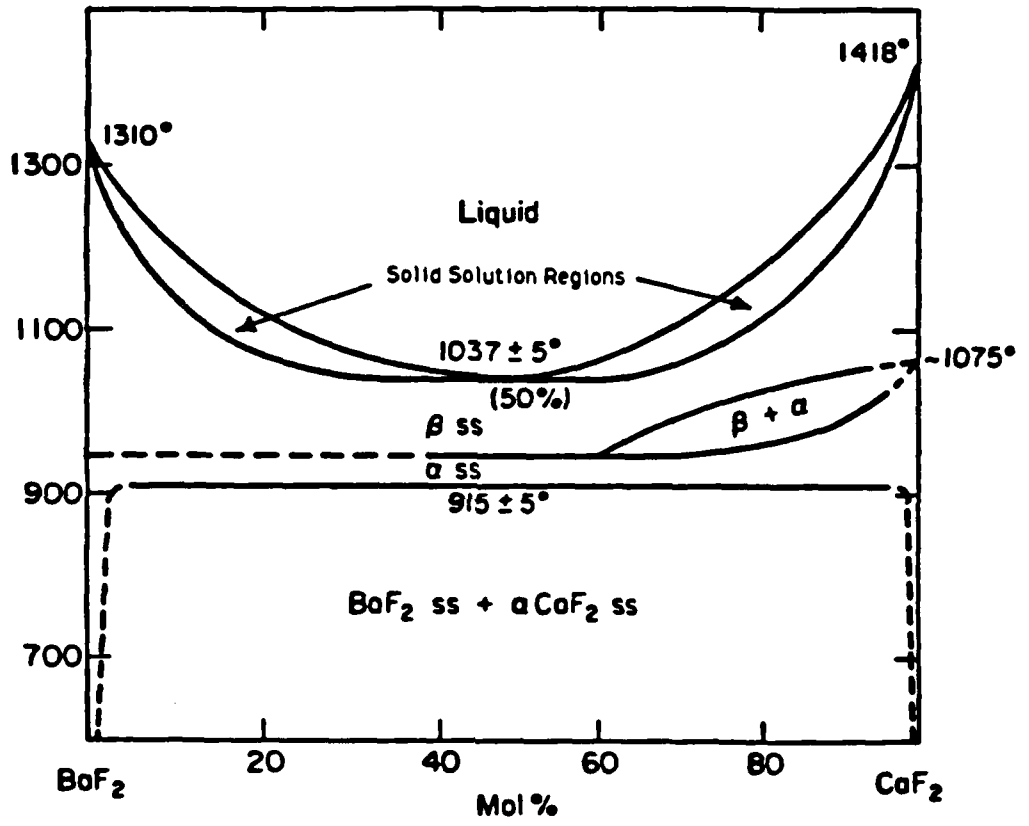

Figure 2.2
Phase Diagram for BaF_2/CaF_2.

there is a slight solubility for 1-2 mole % of BaF_2 in CaF_2 and a larger solubility (6-8 mole %) of CaF_2 in BaF_2. One caveat is noted by the editors of the compilation of phase diagrams from which fig. 2.2 was taken,

> "As originally drawn, subsolidus phase relations appear to disobey the phase rule. This probably reflects the lack of complete data rather than

an inconsistent diagram. One alternative possibility is the existence of an a-b two-phase region with a minimum near 60 mole %."[10]

Differing evidence is presented by thin film researchers as to the mutual solubility of these fluorides, although it is not clear how much of the thin film results are applicable to bulk properties. There exists considerable interest in the use of thin films of fluorides as dielectric insulators on semiconductors for device fabrication. Mixtures of fluorides are used to match the lattice parameter of the substrate (the assumption is that Vegard's law holds, i.e. the lattice parameter varies in direct proportion to the composition). P. W. Sullivan et. al.[11] have published experiments indicating that solid solutions of $Ba_x(CaF_2)_{1-x}$ form for x less than 0.2 in epitaxial thin films (5000 Å) on InP substrates. Graded composition thin Ba/Sr/CaF_2 films have been grown on silicon substrates by H. Zogg et al.[12] but they report a separation of the barium and calcium fluorides into separate phases. While the report of Sullivan would indicate the possibility of extended solid solutions, the fact that it was realized only in a thin film and that even that was contradicted by Zogg, leads one to doubt that bulk crystals can be grown beyond the 6-8 mole % found by Chernevskaya and Ananeva.

2.3.2.2. Other fluoride properties

Figure 2.3 shows the indices of refraction for BaF_2 and CaF_2. The difference in index is roughly constant at 0.05 across the uv and visible portions of the spectrum. It is important to note here that these two fluorides have the largest index difference among combinations of fluorides that are optically desirable. The theory for the expected change in index as a function of composition and wavelength is presented in Appendix B. But in general, when far from an absorption peak, a composite crystal will have a relative change in index approximately proportional to the relative change in the number of moles per unit volume.

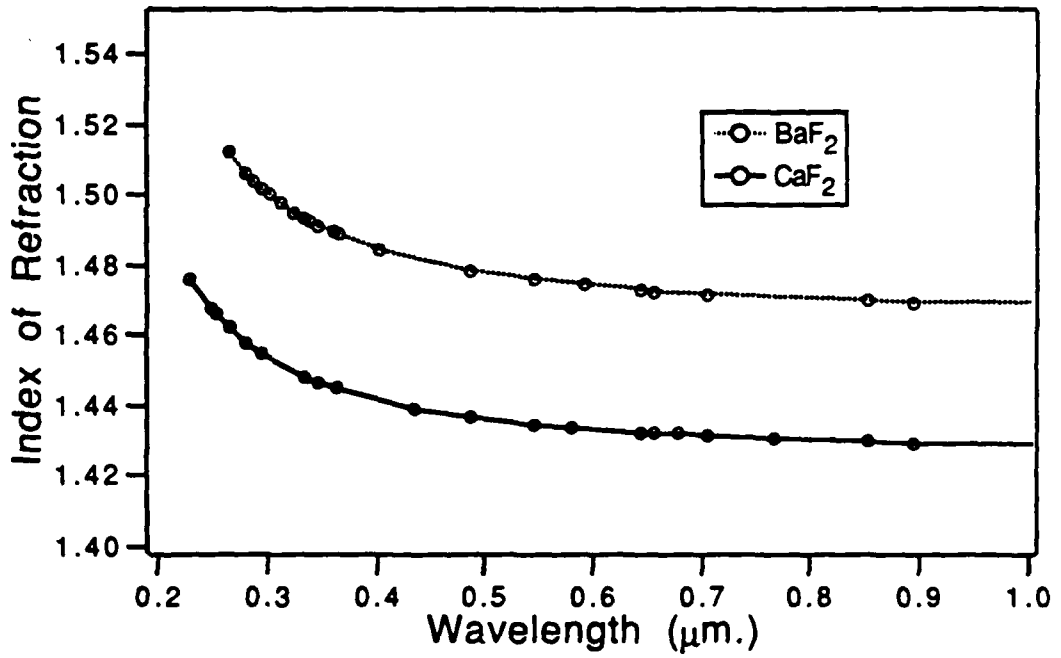

Figure 2.3
Index of Refraction vs wavelength for BaF_2 and CaF_2. Note the high dispersion in the uv portion of the spectrum relative to the visible portion of the spectrum [13].

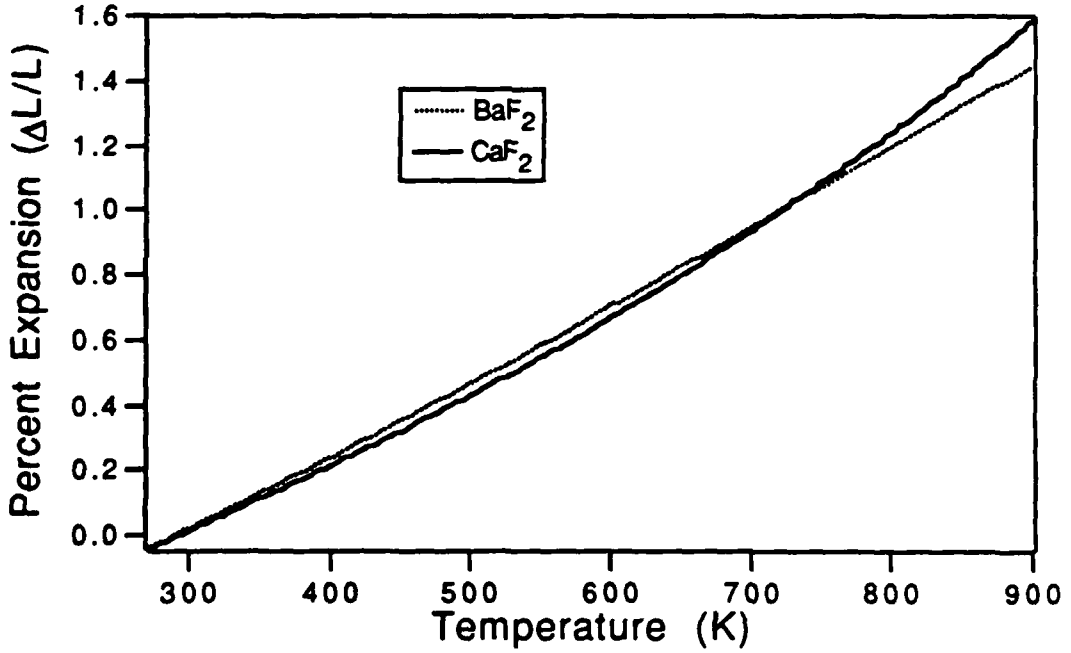

Figure 2.4
Linear expansion for barium fluoride and calcium fluoride as a function of temperature. [14].

During the growth large temperature gradients exist in the crystal; additionally there is a 1300 °C change in temperature from the melting point to room temperature. It is extremely important that the two fluorides have coefficients of thermal expansion that are similar over this temperature range so that stress in the growing and cooling crystal are minimized. Stress induced index changes and cracking are unwanted side effects of dissimilar thermal expansions. Data at temperatures higher than 900 degrees could not be found, but from the curves in fig. 2.4 it can be seen that the two fluorides have almost identical expansions at temperatures below 900 C and are therefore ideal. Other properties of BaF_2 and CaF_2 including their thermo-mechanical properties are summarized in Table 2.1 below.

material	Specific Heat (j/cm-^{0}C)	Thermal conductivity (w/cm-^{0}C)	Thermal diffusivity (cm^2/s)	Young's Modulus (10^6 psi)	Yield Strength (10^3 psi)	Thermal Stress Parameter (j/cm^3)
BaF_2	1.98	0.12	0.061	17.7	3.9	53
CaF_2	2.70	0.095	0.035	11	7-14	68

Table 2.1 Thermo-mechanical properties of BaF_2 and CaF_2.

All of the data presented thus far show that BaF_2 and CaF_2 are exemplary candidates for GRIN growth. To determine what actually takes place during the freezing process, it is necessary to examine in detail the effects of segregation and how the melt and crystal are affected by the presence of two components.

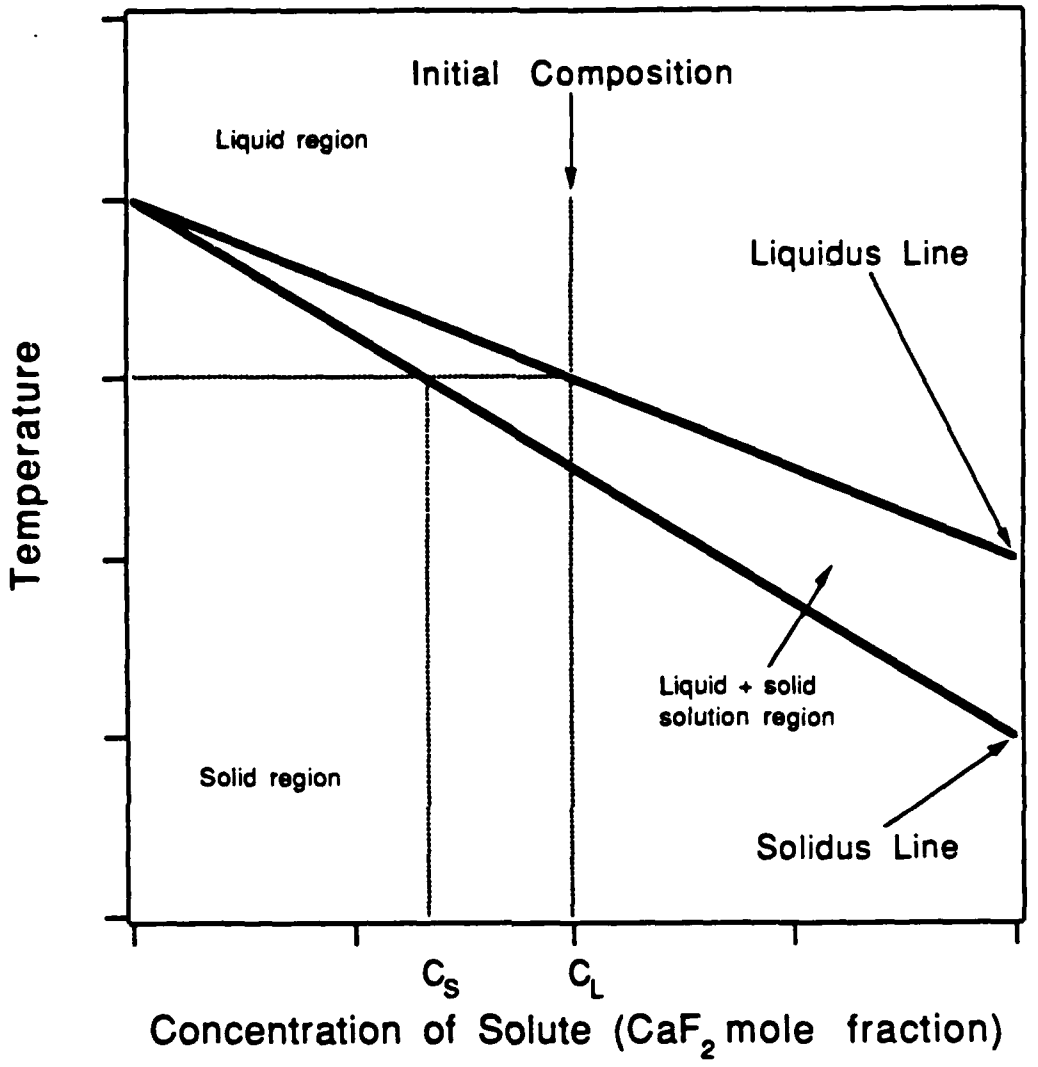

Figure 2.5
Schematic of the BaF_2 rich end of the Ba/CaF_2 phase diagram showing the effects of segregation and a region of solid solution.

2.3.3. Segregation

Figure 2.5 shows a schematic of the barium rich end of the Ba/CaF_2 phase diagram. Suppose one starts with a melt of BaF_2 (solvent) with some arbitrary amount of CaF_2 (solute) in it, say C_L; as the temperature is slowly lowered no changes occur until the temperature reaches the point of intersection of the vertical composition line

with the liquidus line. At this time a small amount of solid will form. Its composition can be found by moving horizontally (at constant temperature) to the solidus line and reading off the composition at that point. The solid that is formed is of concentration C_S and has a different composition from that of the liquid. CaF_2 has been incorporated into the solid at a lower concentration than existed in the liquid. This removal of solvent from the melt raises the overall melt concentration of solute and lowers the freezing point, which, as the temperature is lowered and freezing continues, follows the liquidus line. Similarly, the solid that forms has a variation in solute concentration that follows the solidus line. The effect of segregation in the solid then is to directly form a compositional change along the length of the crystal.

2.3.4. The segregation coefficient

The value quantifying the incorporation of the solute into the freezing solvent is known as the segregation (or distribution) coefficient. While the coefficient can be determined from the phase diagram, the actual segregation that occurs at the solid/liquid interface is highly dependent on the growth conditions. Ideally, the growth of a crystal from the melt is a normal freezing process with equilibrium being reached immediately in the melt (but not necessarily in the solid). In actuality, one of three conditions is likely to exist in the melt: 1) complete mixing in the melt, 2) partial mixing, or 3) no mixing via stirring or convection, diffusion being the sole mixing process.

Case 1) is the easiest to treat since equilibrium exists in the melt and the equilibrium value of the segregation coefficient, k_0, is defined as the ratio of the concentration of the solute in the solid phase to that of the solute in the liquid phase, ie.:

$$k_0 \equiv \frac{C_S}{C_L} . \qquad (2.1)$$

The value of k_0 for a specific melt composition is easily read from the phase diagram by taking the ratio of the concentrations at the intersection of a horizontal line representing the freezing temperature for that concentration with the liquidus line and the solidus line. For the Ba/CaF_2 system k_0 is approximately equal to 0.5.

As normal freezing progresses material is removed from the melt and the solute is partially rejected at the growth interface (for $k_0<1$), the concentration of solute builds up, leading to an ever increasing amount in the melt and an increasing amount being incorporated into the solid. The concentration in the solid at some position after a fraction g has solidified can be expressed as[15] :

$$C = kC_0(1-g)^{k-1} \quad , \tag{2.2}$$

where C_0 is the initial concentration of solute.

Figure 2.6 shows various concentration profiles to be expected for different values of k when normal freezing occurs. It is important to note that the segregation coefficient can also be a function of the growth parameters. For this reason the segregation coefficient is written as k, not k_0, in eq. (2.2) above. From data interpolated from the published phase diagram for Ba/CaF_2 the variation of the segregation coefficient with concentration can be plotted (although there is some risk in interpolating from figures that themselves have an intrinsic error of as much as 1% full scale in both temperature and composition[16]). Figure 2.7 shows the value of k_0 for Ba/CaF_2 as a function of calcium fluoride concentration in the melt.

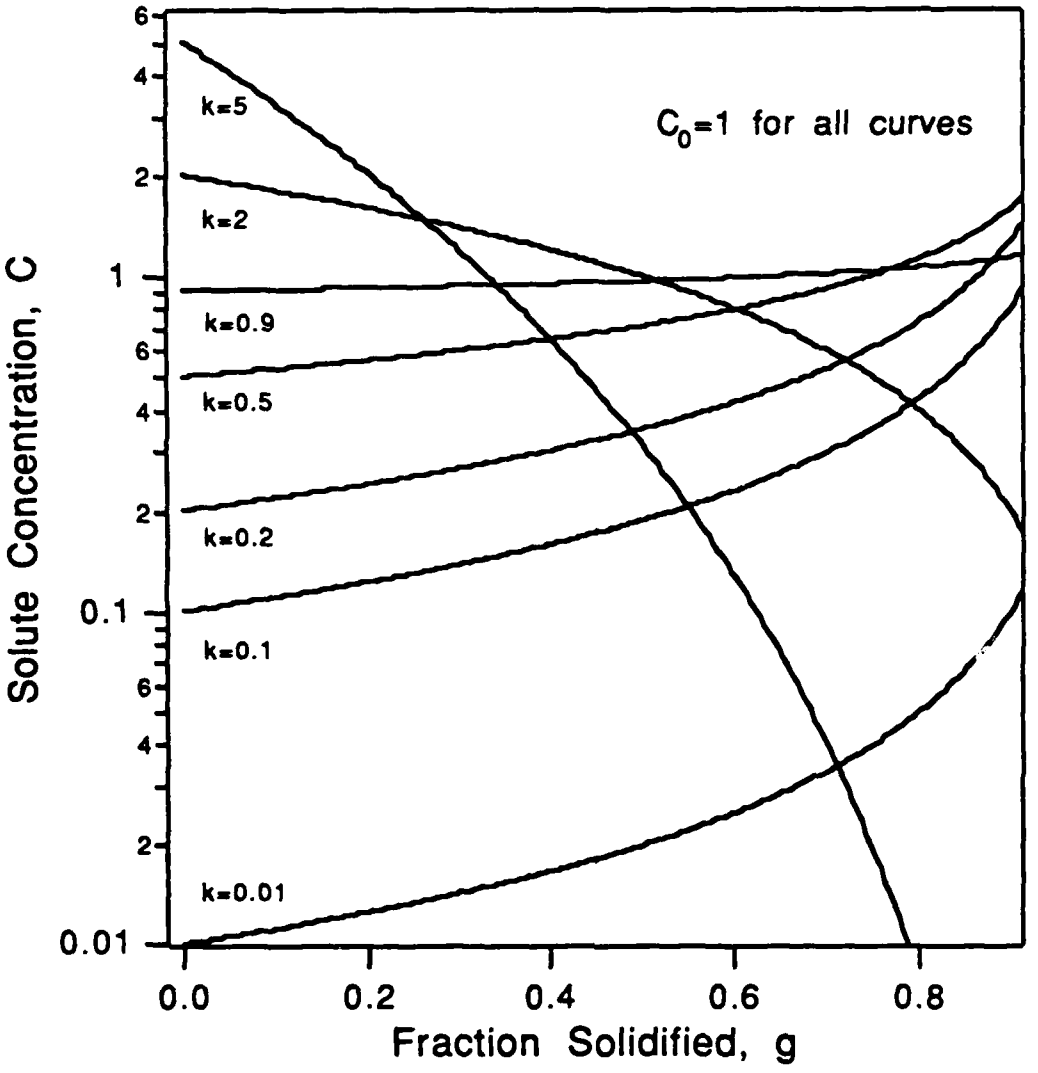

Figure 2.6
Plot of the concentration in the solid versus fraction of the melt solidified for various values of the segregation coefficient using eq. (2.2). (from Pfann).

In continuing the discussion of the effects of segregation it will be assumed that k_0 is a constant. This holds only for very small changes in solute concentration but doesn't greatly affect the value of the following discussions.

In case 3) diffusion is the main means of carrying solute to or from the growth interface. Solute is rejected (for k<1) by the growing crystal and the concentration increases until the amount of solute rejected matches the amount removed by diffusion.

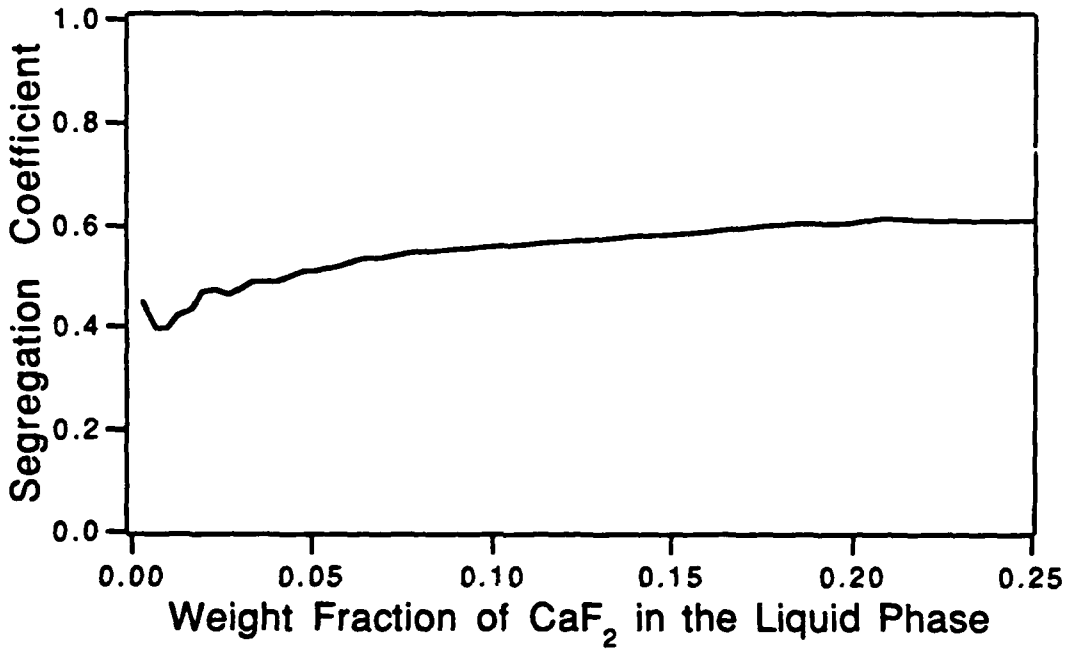

Figure 2.7
Plot of k vs concentration of CaF_2 for the system Ba/CaF_2.

Burton, Prim, and Slichter (BPS)[17] have described this theory mathematically for crystals pulled from the melt, under certain simplifying assumptions. They showed that if mass transport is by diffusion only, the effective segregation coefficient will become equal to one, and no composition gradient will form in the solid (although one exists in the liquid). It is seldom, however, that transport in a molten liquid is dominated by diffusion. Heat driven convection plays a major role in stirring the melt as does motion caused by the rotation of the crucible and the growing crystal[18]. The most likely situation to be encountered is case 2). Mixing occurs, but in a region near the crystal the component of the fluid velocity is zero perpendicular to the crystal and

the flow is laminar and parallel to its surface. Diffusion is then the sole means of mass transport across the laminar flow region. If the melt is otherwise well mixed, BPS have shown that the effective segregation coefficient becomes

$$k_{eff} = \frac{k_0}{k_0 + (1 - k_0)e^{\frac{-f\delta}{D}}} , \qquad (2.3)$$

where D is the solute diffusivity, f is the growth rate, and δ is the thickness of the boundary layer. Formulas for the computation of δ are given by BPS for the flat end of a rotating cylinder being withdrawn from the melt (as an idealization of Czochralski growth). This relation emphasizes the importance of slow growth rates and good mixing in the melt.

Ideally the interface between the growing crystal and the melt is a planar surface perpendicular to the growth direction. Macroscopic changes in shape (ie. concave, convex) do not usually affect segregation except as they lead to faceting, however, microscopic changes in the growth habit can have a very large effect on segregation and the phases present in the solid.

2.4. Interface shape

The shape of the interface between the growing crystal and the liquid melt has been studied extensively[19] since its shape has an effect on the defect density in semiconductor crystals and the stresses in the final product. The importance of the interface shape for GRIN fabrication is that the crystal will have surfaces of constant concentration (and index) that match the interface shape. Macroscopically the interface forms along an isotherm. The shape of the isotherm may be planar, concave, or convex, and is largely a function of the thermal characteristics of the growth system. If the growing crystal has radial radiative losses that are greater than the axial heat flow

the edge of the crystal is cooler and the interface tends to be concave (with respect to the solid). After-heaters are often employed to reduce radiative losses during the growth of materials with high emissivities and low thermal conductivities. Rotation of the crystal can affect the fluid flow in the melt and hence the temperature distribution to the extent of the formation of nonmixing cells near the crystal[20]. This nonhomogeneity in the temperature distribution affects the shape of the interface[21] (and the distribution of impurities in the melt, which is discussed later).

As a liquid unidirectionally freezes, several things may occur at the growth front with respect to the microscopic shape of the solid-liquid interface. Ideally one would like the interface to be smooth. The surface of the interface is a function of freezing rate and concentration of solute. At low freezing rates or solute concentrations the interface is smooth. If either one is raised, supercooling may occur and the increased growth rate results in an increased (for $k_0<1$) amount of solute at the interface[22]. If this process exceeds the speed with which the liquid concentration can equilibrate by mixing, hexagonal substructures appear that confine the solute[23]. Further increases in freezing rates or solute concentration results in the formation of dendrites projecting from the surface and further trapping of the solute. The overall effect is an increase in k_{eff} and an undesirable substructure in the crystal.

2.5. *Profile control in crystals pulled from a binary melt*

An examination of the Ge/Si phase diagram indicates that these are excellent materials from which to form an alloy with a composition gradient, and, given the different indices of refraction for these two, a correspondingly large index gradient. Miceli[24], and later Naughton[25], investigated the fabrication of GRIN alloys of germanium and silicon. They pulled crystals from a melt containing 1-2 atomic percent silicon using the Czochralski process. The resultant crystals had index gradients extending over a distance of 10 mm with an index change of 0-0.15. These materials have good transmission in the region of 2-10 μm but are opaque in the visible portion of the spectrum. The GRIN alloys are measured at 10.6 μm using a Mach-Zehnder interferometer and show excellent correspondence between the measured index profile and the theoretical profile.

In the work of Miceli and Naughton the concentration profiles that are obtained are dependent only on the diameter of the crystal and the segregation coefficient. The concentration profiles follow the normal freezing curves in fig. 2.6 with the only deviations being due to changes in crystal radius. The effect of a changing diameter on the concentration profile is profound, as a change in the radius can be related to a change in the profile as a function of the increased volume of crystal being removed (even though the lift rate is unchanged). Control of the composition profile is important in order to provide index profiles that are useful for optical elements. Although profile control through some programmed change in diameter is feasible, the dynamic range of values the diameter can take are limited and exact control of a variation in diameter is difficult. The ability to change the concentration profile by directly changing the melt concentration is an attractive idea that was originally developed to reverse the effects of segregation during the growth of Ge/In[26] .

2.6. *Active doping*

Czochralski growth has an advantage over other melt growth methods in that the melt is accessible during growth. This opens up the possibility of actively changing the melt composition by adding material to the melt to achieve the desired profile. Actively doping a BaF_2 rich melt by adding CaF_2 forces a concentration change that is greater than would be obtained through normal freezing with a fixed amount of solute. The effects of segregation can be either aided or hindered. A phase diagram published previous to the one in fig. 2.2 for Ba/CaF_2 [27] indicates a segregation coefficient fairly close to one. This would mean a small change in concentration over the length of the crystal. If k were indeed one, the crystal composition would follow the melt composition exactly, giving a simple relationship between the growth rate, the doping rate and the crystal composition. Since the actual segregation coefficient is not unity, the effect of adding solute is similar to increasing k (for $k<1$). It is important to be able to determine what form the concentration profile takes as a function of the growth parameters in order to be able to grow profiles that are useful for optical components.

2.7. *Calculation of dopant concentration in the melt*

The concentration of dopant in the melt as the growth run progresses is a function of the amount of dopant being added, the segregation coefficient, and the growth rate. The form of the calculation is not very complex, as it is essentially a two part related rate problem. The solution, however, becomes increasing more complex as more parameters are added to make the calculation model more realistically related to the growth process. The following calculation initially assumes an identical density for the solvent and the solute, a constant growth rate for the crystal, and a constant melt height. While these first simplifying assumptions are not the case for fluorides, the results

provide insight as to the shape of the concentration profiles to be expected in the final crystal.

The concentration as a weight fraction of the calcium fluoride in the melt is calculated by accounting for the material added (as dopant/solute) and for the material removed (as part of the grown crystal). The concentration of CaF_2 (weight fraction) in the melt can be written as:

$$[CaF_2]_M = \frac{\text{total } CaF_2 \text{ added} - \text{ weight } CaF_2 \text{ taken out}}{\text{total melt weight}} , \qquad (2.4)$$

where the subscript M refers to a quantity in the melt. Defining the terms Λ_X and Λ_C as Λ_X = pull rate of the crystal in g/s (positive for material being pulled from the melt), and Λ_C = pull rate of the calcium fluoride dopant in g/s (positive for material being added to the melt), then the weight of CaF_2 removed at time t, assuming that the initial amount of CaF_2 is zero, is

$$CaF_{2\,out} = \int_0^t [CaF_2]_X \Lambda_X dt . \qquad (2.5)$$

The total weight of CaF_2 added is then $\Lambda_C t$. After changing the subscripts in the equation for the segregation coefficient (eq. (2.1)) to match this notation:

$$k \equiv \frac{C_X}{C_M} = \frac{[CaF_2]_X}{[CaF_2]_M} , \qquad (2.6)$$

the concentration in the melt can be written as

$$[CaF_2]_M = \frac{\Lambda_C t - k\int_0^t [CaF_2]_M \Lambda_X dt}{i + \Lambda_C t - \Lambda_X t} , \qquad (2.7)$$

where i is the initial melt weight. In order to solve eq. (2.7) explicitly for the concentration in the melt as a function of time, the following terms can be defined:

$$\alpha \equiv \frac{\Lambda_C}{\Lambda_X} \quad \text{and} \quad I \equiv \frac{i}{\Lambda_X} \ , \tag{2.8}$$

$$y' = [CaF_2]_M \ , \tag{2.9}$$

and

$$y = \int_0^t [CaF_2]_M \ . \tag{2.10}$$

Substituting these terms into eq. (2.7) the concentration in the melt becomes

$$y' = \frac{\alpha t - ky}{I + t(\alpha - 1)} \ . \tag{2.10}$$

This is a first order linear differential equation. The solution to the homogeneous part of eq. (2.10) can be shown to be

$$y_h = \left[(I + t(\alpha - 1))\right]^{\frac{k}{1-\alpha}} . \tag{2.11}$$

A particular solution to eq. (2.10) is

$$y_p = \frac{\alpha}{k}\left(\frac{I - tk}{1 - (k + \alpha)}\right) . \tag{2.12}$$

The final solution is the sum of the particular solution plus some multiple of the homogeneous solution, fit to the boundary condition that at $t = 0$ the amount of CaF_2 in the melt is zero ($y' = 0$). Thus the concentration in the melt is

$$[CaF_2]_M = \frac{\alpha}{1 - (k + \alpha)}\left\{\left[1 + \frac{t(\alpha - 1)}{I}\right]^{\frac{k}{1-\alpha}-1} - 1\right\} . \tag{2.13}$$

Figure 2.8 shows the various profiles to be expected for different ratios of the amount of solute being added to the amount of crystal being removed, assuming k = 0.5. Note that for values of α less than one the melt will be depleted and the

concentration will build up slowly until the amount of melt is small. If α is larger than one, the concentration increases asymptotically to 100%. For real systems the curves would be abbreviated at the concentration corresponding to maximum solubility.

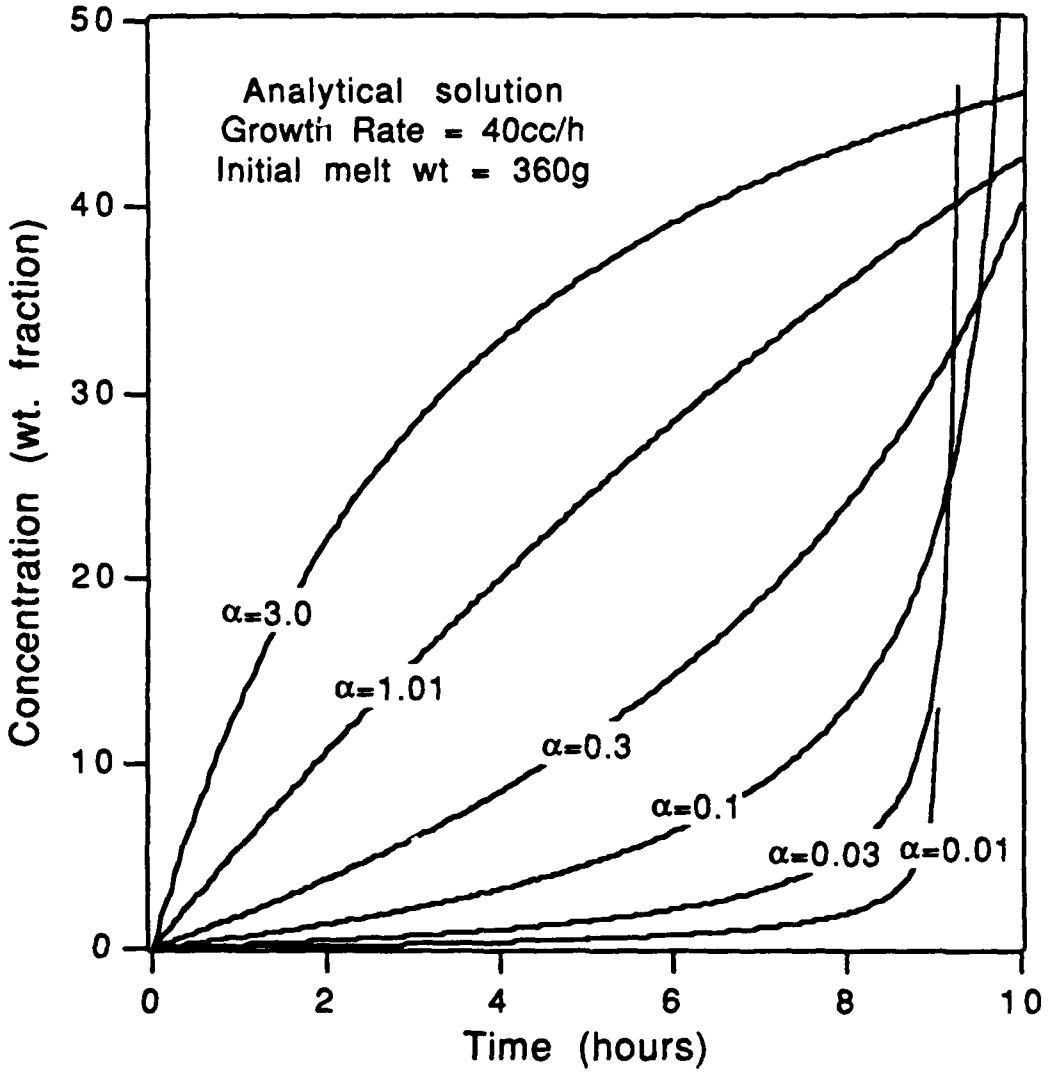

Figure 2.8
Solute concentration in the crystal with k=0.5 as a function of time for different values of α, the ratio of the doping rate to the lift rate.

2.8 A realistic model of crystal growth

To more realistically model the growth process there are three important parameters that were not taken into account in the preceding derivation that must be included. They are that the densities of CaF_2 and BaF_2 are different, that the melt height changes during the growth, and that k, the segregation coefficient, is a function of concentration.

The different densities of CaF_2 and BaF_2 cause the mass fraction of CaF_2 in the melt to not correspond in a simple way to the volume fraction of CaF_2 in the crystal. This means that the growth rate cannot be easily measured for a crystal with an unknown and changing density.

The one parameter that *can* be easily measured is the volume of the crystal as a function of vertical distance after the growth is completed. Unfortunately, the simple product of the lift rate and the cross-sectional area of the crystal does not equal the actual volume rate at which material is being incorporated into the growing crystal. This is due in part to the changing melt height which effectively changes the lift rates for the crystal and the dopant. A realistic model of the growth process must include the effects of the changing melt height. This is dependent on the lift rates and cross-sectional areas of the crystal and dopant. The crystal is assumed to not extend below the surface of the melt.

The third parameter to be included in this model is the functional dependence of the segregation coefficient on concentration, as can be seen graphically in fig. 2.7. A polynomial fit to the segregation coefficient as a function of volume fraction of CaF_2 in the melt can be used. In order to model the concentration in the melt while including these parameters, the concentration can be most simply written as a volume fraction. To explicitly indicate this change of units, the symbol $\mathcal{V}_X$ is used to indicate the volume

fraction of CaF_2 in the crystal while the subscript M refers to the melt in the following derivation.

The symbol A refers to the area in mm^2, V is the volume in mm^3, ρ_C and ρ_B are the densities of CaF_2 and BaF_2, respectively, in g/mm^3, while v is a pull rate in mm/s. For all parameters the subscripts X, M, and C refer to the crystal, the melt, and the CaF_2 dopant, respectively.

A short differential equation can be written that describes the changing melt height by equating differential volumes. A convenient reference point is the point from which the crystal volume is measured. Defining the distance from this point to the initial melt height to be h, the melt position is assumed to have moved a distance l. Any position z along the crystal can then be written as

$$z=h-l \ , \tag{2.14}$$

so that

$$dz=dh-dl \ . \tag{2.15}$$

The differential melt volume added (or removed) due to a differential volume of dopant being added and a differential volume of crystal being removed during a time dt is

$$A_M dl=A_C\left(v_C dt+dl\right)-A_X(z)\left(v_X dt-dl\right) \ , \tag{2.16}$$

where the dependence of A_X, the crystal area, on position has been indicated explicitly. An important assumption being made here is that the crystal does not extend below the surface of the melt.

Using eq. (2.15) in eq. (2.16) to remove dl, dt can be expressed solely in terms of constants and the differential change in the crystal volume, $A_X(z)dz$, as

$$dt=\frac{(A_M - A_X(z) - A_C)}{A_M v_X - (v_C + v_X)}dz \quad . \tag{2.17}$$

Now explicitly writing the volume fraction of CaF_2 in the melt as the ratio of the volume added by doping and the volume removed in the crystal to the total melt volume,

$$\mathcal{V}_M(z)=\frac{\int A_C(v_C dt + dl) - \int A_X(z)\mathcal{V}_X(z)dz}{V_0 + \int A_C(v_C dt + dl) - \int A_X(z)dz} \quad , \tag{2.18}$$

where V_0 is the initial volume of BaF_2. This should be compared with eq. (2.7), representing the weight fraction in the melt. Analogous to the case of the weight fraction segregation coefficient, a volume fraction segregation coefficient can be defined as

$$k^v = \frac{\mathcal{V}_X}{\mathcal{V}_M} \quad , \tag{2.19}$$

where the superscript v serves as a reminder that the coefficient is not the same as the weight fraction coefficient defined and used earlier. Taking the derivative with respect to z of both sides of eq. (2.18) after using eqs. (2.15) through (2.17) to express dt and dl as functions of dz, and using the definition of k^V (eq. (2.19)), the volume fraction in the crystal can now be written as the solution to the linear differential equation

$$\mathcal{V}_X'(z) + \mathcal{V}_X(z)\frac{(\gamma + k^v)A_X(z) + \beta}{V_0 + \gamma V_X(z) + \beta z} - k^v \frac{(\gamma + 1)A_X(z) + \beta}{V_0 + \gamma V_X(z) + \beta z} = 0 \quad , \tag{2.20}$$

where V_X is the volume of the crystal as a function of z, so that

$$V_X(z) = \int A_X(z)dz \quad . \tag{2.21}$$

The additional substitutions

$$\gamma = -\left(1 + \frac{A_C(v_C + v_X)}{A_M v_X - A_C(v_C + v_X)}\right) , \tag{2.22}$$

and

$$\beta = \frac{A_C A_M v_C}{A_M v_X - A_C(v_C + v_X)} . \tag{2.23}$$

have also been made. A_C, A_M, v_C, and v_X are all assumed to be constant.

Although eq. (2.20) is a linear first order differential equation, it is not easily solved analytically. Because of this and the different shape of $A_X(z)$ for each crystal grown, it was deemed expeditious to compute the changing concentration in the melt using a numerical integration of the equation. The form the integration takes is quite straightforward. The position along the grown crystal is incremented differentially and the current crystal area and total volume are calculated. These values are then used to calculate γ, β, and the differential increase in the volume fraction of CaF_2 in the crystal. This is used to calculate the volume of CaF_2 removed from the melt. This process is then iterated while also accounting for the change in melt height, which changes the effective lift rates for the dopant and the crystal.

Beyond the point where doping is halted the concentration continues to rise in a way similar to that predicted by eq. (2.2) for normal freezing. This algorithm is used to predict the concentration profiles that are actually grown in the Ba/CaF_2 crystals. These predictions of the profiles based on the actual growth parameters and the measured crystals' volumes, along with the measured index and concentration data, are presented in Chapter 3. A direct comparison is made between the grown profiles and the theoretical predictions.

2.9. Summary

Different types of melt growth have been reviewed and the process of segregation during normal freezing has been described.

The criteria for choosing the phase properties of materials in a two component system such that a concentration gradient can be fabricated through the normal freezing process have been presented along with the theory governing the form that the concentration profiles would be expected to take based on those properties.

Fluorides of barium and calcium have been found to be ideal materials because of their transparency and phase properties that allow the formation of a solid solution under the proper conditions. Several other fluorides also have solid solutions in combination with calcium fluoride and/or barium fluoride. These include fluorides of lanthanum, strontium, and yttrium. The barium/calcium fluoride combination was chosen because of its relatively large difference in index of refraction and good mechanical and thermal properties.

To effect additional control over the concentration profile the addition of a dopant during the crystal growth has been proposed. The equations governing the concentration profile during the growth of the crystal have been adapted to incorporate the effect of an external source of one of the melt components. These equations have been solved analytically for certain cases, and an iterative means of solution has been implemented for cases with less tractable forms, including the more realistic solution involving a changing melt level.

References for Chapter 2.

[1]*Optical Crystals by Optovac*, Handbook 82, Optovac Inc., North Bookfield, MA. (1982).

[2]W. F. Pfann, *Zone Melting*, 2nd ed., J. Wiley and Sons, New York (1966).

[3]J. C. Brice, *Crystal Growth Processes*, J. Wiley & Sons, New York (1986).

[4]K. A. Jackson and J. D. Hunt, Lamellar and Rod Eutectic Growth, Trans. of the Metallurgical Soc. AIME **236** (1966) 1129.

[5]*Introduction to Phase Equilibria in Ceramics*, C. Bergeron and S. Risbud, American Ceramic Society, Columbus, OH (1984).

[6]A. I. Kitaigorodsky, *Mixed Crystals*, Springer-Verlag, New York, NY (1984).

[7]*Phase Diagrams for Ceramists* **VI**, American Ceramic Society, Inc., Columbus, OH (1986) Fig. 5782.

[8]M. Rolin and M. Clausier, Rev. Int. Hautes Temp. Refract. **4** [1] , (1967) (Fig. 4813 in Phase Diagrams for Ceramists).

[9]E. G. Chernevskaya and G. V. Ananeva, "Structure of Mixed Crystals Based on CaF_2, SrF_2, and BaF_2," Sov Phys.-Sol. St. **8** (1966) 169.

[10]*Phase Diagrams for Ceramists*, Loc. cit.

[11]P. W. Sullivan, R. F. C. Farrow, and G. R. Jones, "Insulating Epitaxial Films of BaF_2, CaF_2, and $Ba_xCa_{1-x}F_2$ Grown by MBE on InP Substrates," J. Crystal Growth **60** (1982) 403.

[12]H. Zogg, P. Maier, and H. Melchior, "Graded IIa-Fluoride Buffer Layers for Heteroepitaxy of Lead Chalcogenides and CdTe on Si," J. Crys. Growth, **80** (1987) 408.

[13]*Handbook of Chemistry and Physics*, 57 ed., R. C. Weast (ed.), CRC Press Inc. (1976) p 7-83 and p 7-87.

[14]*Thermal Expansion - Nonmetallic Solids*, Touloukian et al. (eds.), Plenum, New York, NY (1977) 1021,1025.

[15]Pfann, op. cit. p 10 eq. (2.1).

[16]Brice, op. cit., p 51

[17]J. A. Burton, R. C. Prim, and W. P. Slichter, J. Chem. Phys. **21**, (1953) 1987.

[18]J. R. Carruthers, "Dynamics of Crystal Growth," in *Crystal Growth: A Tutorial Approach*, Bardsley, Hurle, and Mullin (eds.), North-Holland (1979).

[19]J.C. Brice, "Analysis of the Temperature Distribution in Pulled Crystals," J. Crys. Growth **2** (1968) 395.

[20]J. R. Carruthers and K. Nassau, "Nonmixing Cells due to Crucible Rotation during Czochralski Crystal Growth," J. Appl. Phys. **30** (1968) 5205.

[21]C. D. Brandle, Czochralski Growth of Large Oxide Crystals, in *Crystal Growth, a Tutorial Approach,* Bardsley, Hurle, and Mullin (eds.), North-Holland (1979).

[22]Pfann, op. cit., p 22-23

[23]D. A. Petrov and B. A. Kolachev, "Impurity Redistribution During Crystallization and the Way this Appears in the Crystal Structure," in *Growth of Crystals,* v.**1**, Shubnikov and Sheftal (eds.) Moscow (1957).

[24]J. J. Miceli, *Infrared Gradient-Index Optics: Materials, Fabrication, and Testing*, Ph.D. thesis, University of Rochester, 1982.

[25]D. Naughton, *Fabrication and Testing of Infrared Gradient-Index materials*, M.S. thesis, University of Rochester, 1986.

[26]H. Nelson,"Continuous-Process Apparatus for Growing Single-Crystal Germanium," in *Transistors I*, RCA Laboratories (1956) 66.

[27]Rolin and Clausier, op. cit.

CHAPTER 3

Experimental Apparatus and Procedures

3.1. Introduction

An important and crucial aspect of the research presented in this thesis is the experimental work. A large part of this investigation is aimed at controlled alteration of the axial composition profile of fluoride crystals by actively doping the melt from which they are grown. In this chapter the experimental apparatus and procedures used to grow GRIN fluoride crystals are described. In addition, some of the problems that occurred while conducting the experiments and how these problems were overcome are also presented.

The chapter is divided into three parts. The first part describes the actual growth apparatus. The form of the mechanical apparatus used to pull crystals has not changed radically since it was introduced by Czochralski in 1918[1]. The crystal puller consists of a vacuum furnace chamber with provisions for lowering a seed crystal into the melt and then slowly lifting it upwards. Improvements in crystal growth of fluorides have come about more through advances in the areas of process control and purity of starting materials than through changes in the basic grower design. The grower used for this research is the Kayex-Hamco CG800, a relatively small commercial grower built for the growth of single crystal silicon boules for the semiconductor industry. The fabrication of a GRIN crystal is accomplished through a modification of the grower that allows dopant material to be added to the melt in a controlled manner.

The second part of this chapter discusses the materials used for the growth runs. In most growth processes purity of the starting material and the avoidance of

contamination during growth is crucial to the success of the growth. In the Czochralski method the crystal being grown comes in contact solely with the atmosphere in the growth chamber. Only the melt is in contact with the crucible. A careful choice of ambient atmosphere and crucible is as important as the purity of the starting materials for the elimination of contaminants from the final crystal.

The third and final section of this chapter describes in some detail the steps taken in growing a GRIN crystal by Czochralski's method and the aspects that are unique to this project. This section, along with appendix A, which explicitly describes the steps necessary to operate the CG800, may prove to be valuable to anyone using this apparatus, since documentation on actual growth procedures in the user's manual are scanty at best, and the general literature does not provide information specific to growth using this particular machine.

3.2. Crystal Grower

A detailed description of most of the crystal grower and its control systems can be found in the operator's manual for the CG800. In the interest of providing both background and a self contained document for the reader, the prominent features and components of the grower and their functions are described below.

3.2.1. Mechanical

The CG800 crystal grower consists of 3 main systems: the furnace chambers and hot zone, the control console, and the lift mechanisms for the crucible and seed crystal. The furnace chamber is in two parts, an upper section and a lower section with an O-ring seal between them. The upper chamber is equipped with a hydraulic lift to raise the chamber up and give access to the interior. The main function of the upper chamber is to provide space for the pulled crystal. The lower furnace chamber

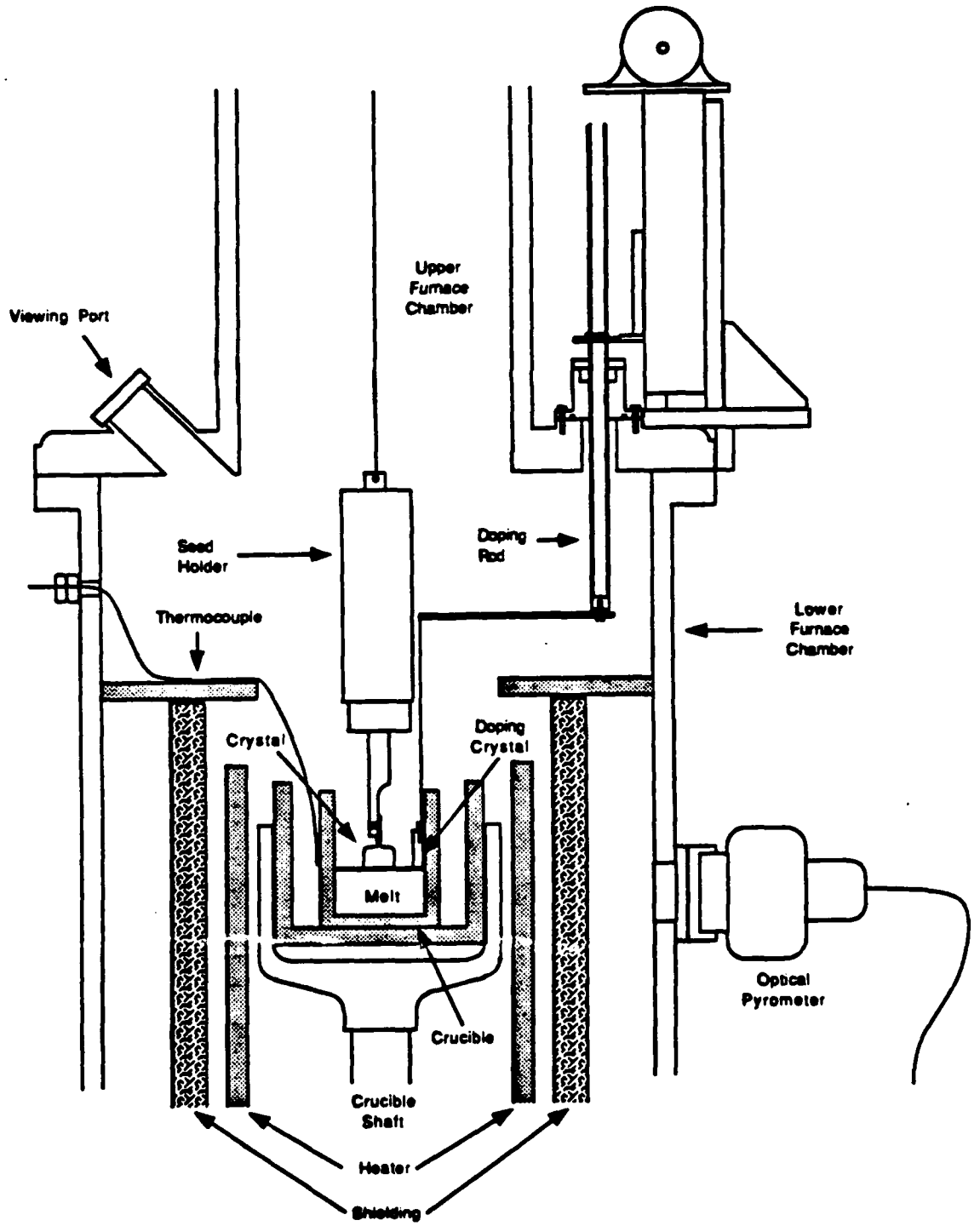

Figure 3.1
Cut-away view of the CG800 Crystal grower with modifications to allow doping of the melt.

contains the "hot zone", the crucible shaft, and the crucible. The hot zone consists of several graphite elements: a resistance heater, crucible supports, and the graphite and fused silica parts for insulation and spacing. For reference see fig. 3.1, a scale diagram of the modified CG800 grower.

Viewing ports of fused silica in the top of the lower chamber allow the operator to observe the growing crystal. Because of the intense thermal radiation emitted by the hot zone, a shield consisting of a quartz plate coated with a thin film of gold acts as a hot mirror, reflecting most of the radiation above 0.60 μm back into the chamber while transmitting enough visible light to allow comfortable viewing.

The furnace chambers, the power leads and transformers, the line to the vacuum pump, and the crucible shaft are all water cooled since the melting point of silicon, (and CaF_2) are near the softening point of steel.

The seed lift mechanism in the CG800 is a major departure from the traditional rod based seed lift. In most growers reported in the literature and most commercial growers on the market, a hydraulic system or other means are used to raise and lower the seed holder. In the CG800 system the seed holder is attached to a steel cable which is wound on a spool mounted on a platform at the top of the upper furnace chamber. The whole platform rotates at speeds from 0 to 50 rpm. The seed lift can be set to raise or lower the seed holder at a constant speed between 0.00 and 20.00 inches per hour in increments of 0.01 iph. The crucible can co-rotate or counter-rotate relative to the seed holder to reduce the effects of any spatial variations in heater temperature. The crucible itself can be raised or lowered and can be linked electronically to the seed lift rate. As the crystal grows the melt volume is reduced and the melt height in the crucible falls. For the diameter control system to accurately track the crystal diameter the melt height must remain constant. To maintain a constant melt height the crucible lift rate can be set

to be some factor times the seed lift rate so that variations in seed lift rate are tracked by the crucible lift rate. Assuming a constant density for the liquid and solid, the multiplying factor is the ratio of the melt surface area to the cross-sectional area of the growing crystal. This value is set once the desired diameter of the crystal is reached.

3.2.2. Control systems

Control of the furnace temperature is provided by a commercial digital controller that adjusts the power to the heater and uses the temperature in the hot zone as feedback. The temperature is sensed by an optical pyrometer that is focused on the outer surface of the heater shield. While this does not give an accurate reading of the temperature in the hot zone, it does allow the temperature to be held to less than a $\pm$ 0.3 ^{o}C deviation from a chosen set point (for temperatures near the melting point of barium/calcium fluoride). The controller set point is in units of millivolts, corresponding to the voltage output of the pyrometer. This set point can be ramped either up or down at rates of 0 to 5 set points per minute. To obtain an accurate reading of the temperature at the crucible ($\pm$ 5 ^{o}C), a thermocouple was fabricated from tungsten-5% rhenium and tungsten-26% rhenium wires threaded through ceramic insulators and was installed via a homemade feed-through at the back of the growth chamber. The thermocouple junction was placed next to the outer wall of the crucible, giving a much more accurate reading of the melt temperature. Placing the junction inside the crucible (or in the melt itself) was done for a period of time but was discontinued due to corrosion of the ceramic insulators by fluoride fumes.

This grower was originally manufactured for growing semiconductors, thus it is equipped with a diameter control system that optically detects the position of the meniscus at the edge of the growing crystal. The meniscus is seen as brighter than the rest of the surface of the melt[2], giving a bright reference ring from which to measure

the diameter of the crystal. The curvature of the meniscus reflects the bright crucible walls making it stand out from the melt surface and the crystal. The interior of the crucible is then imaged onto a screen where two photo-diodes can be positioned on the meniscus image when it has reached the desired diameter.

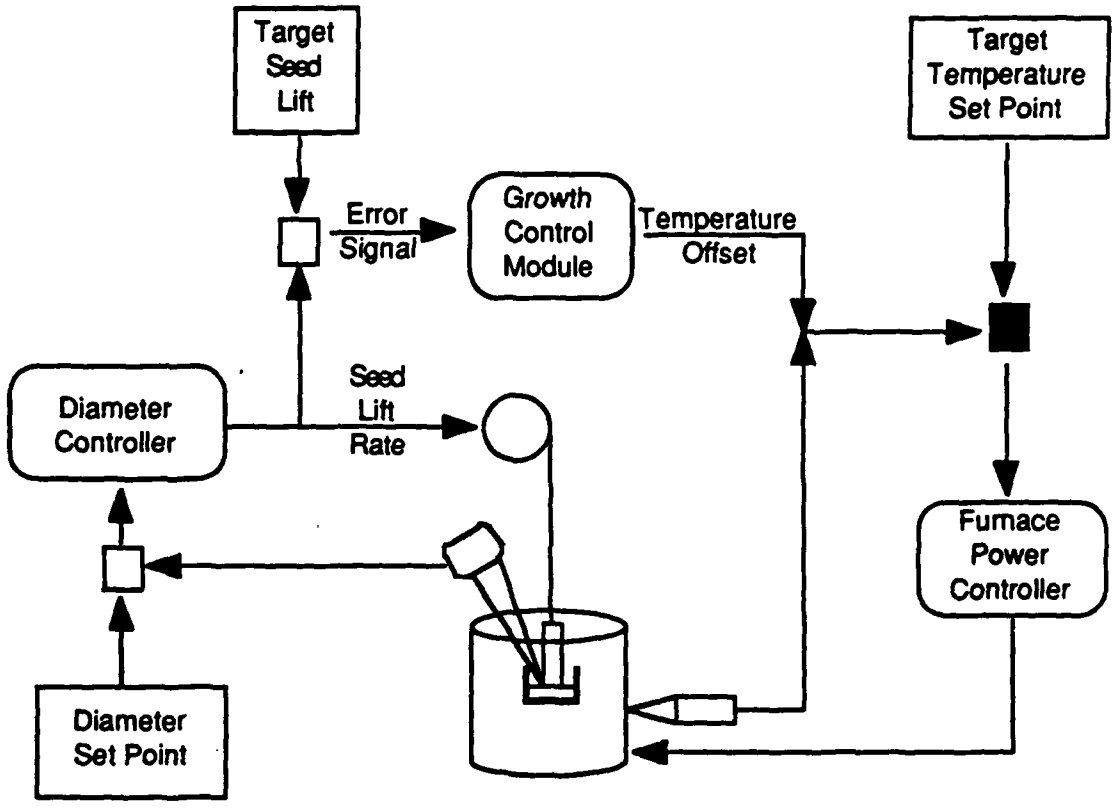

Figure 3.2
Control flow diagram for the CG800.

A second digital controller uses the signals from the photo-diodes as feedback when varying the seed lift and thereby maintains a constant diameter of the growing crystal. The lift rate, seed diameter, and heater control systems are all linked through the "growth control panel". This control allows a target seed lift rate to be set, and then varies the heater power with feedback from the diameter controller. As the heater power changes there is a corresponding change in the growth rate, causing the diameter

to change. The diameter controller then varies the seed lift to hold the diameter constant. A three way balance is maintained between the lift rate, the crystal diameter, and the heater power (see fig. 3.2) while maintaining both the target diameter and the target seed lift rate.

The problem with this diameter control system for the growth of fluorides, which are transparent both in solid and liquid form, is that the meniscus is extremely difficult to observe. (Imagine an icicle being lifted from a glass of water, while you watch from a distance through an orange filter, and you will have some feeling for the difficulties involved.) This limitation can be overcome by constantly weighing either the crucible or the crystal[3] during growth and using that value as feedback in maintaining a constant diameter. Unfortunately the crystal grower used for this research does not have facilities for weight sensing. As a result, the operator must watch the growth and manually adjust the lift rate and/or the heater power to keep the desired crystal diameter. This subject is discussed further in the section on growth procedures.

3.2.3. Doping Rod

Finding a mechanism for adding dopant to a corrosive melt when the growth takes place in a low pressure, high temperature chamber is difficult. One method is to simply drop pieces of dopant into the melt[4] from a suspended container with control provided by some type of vacuum feed-through. Other workers have either replenished the melt[5], or added dopant[6], in the form of a rod that is directly linked to the seed lift mechanism. The former method is not directly applicable to the doping of fluoride melts for several reasons. Simply dropping the dopant into the melt is too disruptive to the growth process (in small crucibles) and doesn't lend itself to a uniformly changing

melt concentration. Not having independent control of the dopant removes the freedom of the experimenter to vary the doping rates at will.

The method adopted for the doping of the fluoride melts is shown in fig. 3.1. A stainless steel water-cooled rod enters the lower furnace chamber through a flanged port in the cover that has been fitted with a rotary vacuum seal to hold the rod. A molybdenum wire is used to attach the calcium fluoride dopant crystal that is to be lowered into the melt to a stainless steel support that in turn is fastened to the bottom of the rod. Because the rod can rotate through approximately 40 degrees, the dopant can be positioned over the crucible after the growth has started without interfering with the crystal and seed holder. Raising and lowering of the rod is accomplished through the use of a "fork lift" that fits a collar attached to the rod. The lift is attached to a Velmex[7] motorized positioning stage and controller. The stage and rod can be raised or lowered at speeds between 10 and 270 mm/h. The total possible travel is 120 mm (which could be extended if necessary by reducing the size of the cooling water plumbing at the upper end of the rod).

3.3. Materials used for the Czochralski growth of fluorides

The discussion on growth materials includes the atmosphere in the furnace chamber and the crucibles used, since their materials' properties are very important to the growth process.

3.3.1. Charge

The charge is defined as the starting materials loaded into the crucible at the beginning of a growth run. Starting materials for crystal growth can be selected pieces of natural fluorspar (CaF_2) or synthetically produced reagents, usually in powder form. Reagent grade BaF_2 and CaF_2 powder, 99.9% pure from Johnson Matthey Inc. were used as starting materials. Investigators during the first half of this century found that only the natural crystalline form would produce high quality crystals when melted. Synthetic preparations gave opaque crystals. Fluoride powders prepared by precipitation from a mixture of carbonates and hydrofluoric acid can contain significant amounts of water[8]. The main difficulty in growing synthetic fluoride crystals from these powders is the prevention of incorporation of oxygen into the melt (or "charge") via hydrolysis. The oxygen can be initially present in the furnace atmosphere or in the starting material as water. Calcium or barium oxide is formed and hydrogen fluoride gas is given off. The reaction with water is

$$Ca / BaF_2 + H_2O \longrightarrow Ca / BaO + 2HF\uparrow$$

This process actually occurs well before the charge melts, even at temperatures as low as 100 ^oC[9], so that evaporating the water by slow heating prior to melting the charge is not feasible. Enough water is present in a charge that is in powder form, even after being held in a vacuum, that it can be detected in the melt. CaO is a white opaque solid with a melting point much higher than that of CaF_2. Its presence is troublesome

not only in the grown crystal as opaque inclusions, but also during the start of growth because it forms a thin layer on the top of the melt and blocks the seed from contacting the melt surface. If the temperature of the melt surface is low enough, it can form sites for the nucleation and growth of "islands" on the surface of the melt.

A second form which oxygen contamination can take is the direct replacement of a fluorine ion with an oxygen ion in the crystal lattice. At low levels this leads to an absorption at 0.210 μm[10] and an absorption in the visible at high levels[11]. The presence of large quantities of oxygen in the melt can be seen as a brown discoloration of the crystal.

To avoid contamination by oxygen and the formation of Ca/BaO, a "scavenger" must be used in the charge to remove these contaminants. Stockbarger and also Stepanov[12] used PbF_2 to scavenge oxygen from the melt and the same process was found to be satisfactory for the preparation of Ba/CaF_2 for this thesis. In the presence of water, hydrogen fluoride and lead oxide is formed preferentially over calcium or barium oxide. This compound and any excess PbF_2 then evaporates below the melting point of Ba/CaF_2, leaving a pure melt. (boiling point of PbF_2 is 1290 ^{o}C).

All of the above effects were significant problems during the early part of this research and were overcome with the use of the PbF_2 scavenger. Approximately 2% PbF_2 by weight was found to be satisfactory, in accordance with the 0.25 to 3.0 % used by Stepanov and Stockbarger, respectively. The largest source of melt/crystal contamination was out-gassing of oxygen from the graphite crucible which is discussed in the section on crucibles.

3.3.2. Atmosphere

Having an inert gas flow through the growth chamber has important effects on a number of processes that are secondary or unwanted that take place during a growth

run. The furnace chamber is not a high vacuum system in the sense that its seals are not of high integrity, thus some outside air may leak into the chamber. When pumping down before a growth run the pressure rarely goes below 50 millitorr. (Although exact locations were not ascertained, the most likely sources for leaks are the feed-throughs for the thermocouple and the doping rod, and the ball valve on the pump line.) A large amount of fumes evolve from the charge, especially during fusion. Graphite evaporates from the surface of the heater. The vapor pressure of the melt causes an increasing amount of melt lost as fumes with decreasing chamber pressure.

The effect of each of these processes is to either contaminate the melt, coat the viewing ports, or remove material from the melt. Having an atmosphere of flowing inert gas reduces evaporation of the melt by increasing the chamber pressure; it helps remove room air that may be present due to chamber leaks, and it keeps fumes from coalescing onto the viewing ports by flowing across the ports as it enters the chamber.

The second purpose that the atmosphere in the chamber fulfills is the continued fluorination of the melt and crystal for removal of impurities, especially oxygen. A combination of HF and some inert gas such as He, Ar, or N_2 is often used for this purpose[13].

Due to problems involving the corrosivity of a fluorinating atmosphere, an inert atmosphere of pure N_2 is used. A corrosive atmosphere would seriously shorten the life of the valves and fittings in the vacuum lines of the grower, and would also shorten the life of the silica viewing ports. The N_2 gas flows through a chamber containing a moisture absorbing material and then through a molecular sieve to keep it clean and dry. Chamber pressures are in the vicinity of 15-50 torr with the gas flowing at a rate of approximately 20 cfh at 30 psi. This flow keeps the viewing ports clear but is not

enough to keep fumes from coating the inner surfaces of the furnace chamber. These fumes are easily removed after the chamber is opened at the end of each growth run.

3.3.3. Seed Preparation

The seed provides a structure onto which the crystal begins growing and also dictates the orientation of the crystal lattice in the growing crystal. It is possible for portions of the crystal to grow with several (or many) regions, each with its own orientation. The occurrence and origin of these regions depends initially on the seed and later on defects that occur in the crystal as it is growing. If the seed consists of only one orientation it is called a "single" crystal, and a crystal grown from it, at least initially, is single. Once growth is started a narrow "neck" is grown with a diameter of 2-3 mm and several centimeters in length, to encourage the growth of the crystal from a region of the seed with one orientation. There is also evidence from the semiconductor industry that microscopic defects in the crystalline structure propagate outwards during the growth of the neck, leaving the bulk of the crystal defect-free.

Changes in orientation of the crystal lattice do not have any effect on the optical properties of the crystal unless the crystal is not isotropic. For most optical purposes it is not essential that crystals be single unless the application calls for a very high degree of homogeneity or lack of scattering. Scattering at the boundary between two different orientations of the crystalline lattice sometimes occurs when the segregation coefficients for the two orientations are very different. For example, solute can build up at one interface for a particular orientation and then be incorporated into the crystal as a different orientation begins growth.

Seeds used to grow GRIN crystals were fabricated by melting an appropriate amount of BaF_2 powder with PbF_2 scavenger in a large diameter crucible. Since the seed holder is designed to accept rectangular seeds with a 6 mm square cross-section,

enough powder was melted to give a depth of 6 mm in the crucible and then the resultant "pancake" was cut into 6x6x50 mm seeds. Their length was not crucial, but needed to be greater than approximately 20 mm to both clear the end of the seed holder and still leave enough to be tied securely to the holder. Since obtaining single crystals was not an objective of this work, most of the crystals grown were multiply oriented and the orientation of the seed was not critical.

BaF_2 seeds were used instead of CaF_2 seeds because of the decision to work in the high BaF_2 end of the Ba/CaF_2 phase diagram. A CaF_2 seed would be dissolved by a BaF_2 melt, lowering the local freezing point and preventing the growth of a crystal.

3.3.4. Crucibles

The crucible is the only part of the growth system that actually comes in contact with the fluoride, either solid or liquid, thus its properties are extremely important. It needs to be inert, have good thermal conductivity, and must not release any impurities into the melt. This last criterion is particularly important, as the high chemical activity of molten fluorides leads to the formation in the melt of fluorinated compounds of any impurities in the crucible, especially metals. This incorporation of impurities into the melt by fluorides is effective to the extent that a suggested method for reducing the impurity levels in graphite crucibles is to melt a fluoride in the crucible[14]. The crucible material should have a high thermal conductivity so that heat transfer to the melt is as uniform as is possible.

3.3.4.1. Results for various crucible materials

The types of crucibles reported in the growth literature for use with fluoride melts include platinum, platinum/rhodium, boron nitride, molybdenum, and various forms of graphite. All of these materials are inert to Ba/Ca fluoride melts at temperatures near the melting point of CaF_2.

Platinum crucibles were undesirable for this research not only because of their expense, but because they are subject to attack by lead fluoride[15], which is used in the purification process during melt-down. Both boron nitride and molybdenum crucibles were used but are wetted by the barium fluoride melt and appeared to react with it. The interior of the boron nitride crucible chipped and flaked, with small pieces adhering to the frozen melt. The melt itself was colorless but translucent. No further analysis was attempted.

The barium fluoride melted in the molybdenum crucible was not transparent when molten, and was extremely difficult to remove from the crucible after cooling. The frozen charges were brown or gray and translucent. Yellow fumes were found on the graphite heater and other hot zone parts. Electron microprobe analysis showed that these fumes were molybdenum. It was not clear what caused this, although oxidation may have played a part. The only obvious difference between this research and that reported by Abrahams and Herkart[16], who successfully melted CaF_2 in a molybdenum crucible, was the atmosphere. They used pure He as opposed to the N_2 used for this research.

Graphite is perhaps the most widely used crucible material for the growth of all types of fluoride crystals. The growth of large fluoride crystals by the Bridgman-Stockbarger method was originally done in graphite crucibles by Stockbarger and they are still used by the crystal manufacturing industry today. Graphite is not wet by molten fluorides and is not reactive to a reducing atmosphere. Several different types of graphite crucibles were used for the crystals grown for this thesis.

Two problems can occur with the use of a plain graphite crucible. The first is that the graphite, being porous, absorbs oxygen from the atmosphere while the charge is being loaded. Unless the crucible is carefully out-gassed before melting the charge,

the oxygen is slowly released into the melt during growth. This effect is first noticed as a gradual discoloration of a CaF_2 melt as it is repeatedly used for the growth of several small homogeneous crystals. The melt eventually becomes gray/white and opaque, although the crystals grown from it have relatively good transparency, to at least 0.210 μm. For this reason it is important that the crucible and the graphite parts of the hot zone be kept under vacuum after the initial bake-out, or in an inert atmosphere while not in use, in addition to being out-gassed after being charged. This problem of the incorporation of oxygen also points out the aforementioned importance of a scavenger in the charge when the crucible is loaded with pieces of crystal from previous growth runs.

The second problem encountered in using a plain graphite crucible is the presence of graphite dust on the surface of the melt[17]. This interferes with the growth process and forms nucleation sites for the growth of other crystals which then float on the surface of the melt and later may freeze onto the sides of the growing crystal. Several methods have been devised and reported in the literature for removing dust or other contaminants from the surface of the melt. One straightforward solution is to use a long, manually operated rod with a pointed tip that can be dipped into the melt to pick up dust[18]. A second, more complex solution devised by E. Schultheiss et al.[19] for the growth of $BiLiF_4$ is to first dip a platinum wire into the melt, letting the surface contaminants freeze onto it. Next the melt is pulled using a second platinum wire as a seed so that any contaminants adhering to the crucible walls are released as the melt level drops. This crystal is then remelted and the newly exposed and now floating contaminants are again picked up by the platinum wire. In contrast to this detailed procedure, it is found that careful cleaning and vacuuming out of the interior of a plain

graphite crucible usually yields good results, with only a small amount of dust showing up on the melt surface.

The above problems can be overcome entirely by using a vitreous carbon crucible[20]. These crucibles are pure carbon in a glassy form. The chemical properties are the same as graphite, while the surface is very smooth and non-porous. Unfortunately these crucibles are subject to breakage due to mechanical and thermal stresses during cool-down. The coefficient of thermal expansion and its mechanical strength are similar to those of graphite, but the vitreous carbon is both brittle and unavailable in sizes thicker than 3 mm so that a larger graphite crucible is more durable.

One vitreous carbon crucible was used for four growth runs before it shattered. The melts were very clear and free from surface contamination. A compromise was found that incorporates the best of both crucible types by having the interior of a plain graphite crucible coated[21] with vitreous carbon. The resultant crucible was lower in cost than the pure vitreous carbon crucible with the same properties relative to the melt while maintaining the mechanical and thermal robustness of the thicker plain graphite. These vitreous carbon coated crucibles lasted for 8-12 runs before the coating wore off or evaporated and had to be replaced.

3.4. Experimental procedures for the growth of a GRIN crystal

This section describes the procedures and methods used in pulling a barium fluoride crystal from the melt while actively doping the melt with calcium fluoride. A more detailed description of the growth procedures is located in Appendix A.

After the crucible is charged with BaF_2 and PbF_2 the power to the heater is turned on and slowly increased until the charge begins to melt. Before melting the charge fuses, or sinters, and its volume decreases. The melt then bubbles initially as any remaining lead oxides or fluorides evaporate (or as the crucible releases gas into the melt and HF evolves). If any graphite dust remains on the surface of the melt, it can be removed by repeatedly carrying out the following two steps until no dust remains: 1) allow the surface of the melt to freeze and then push the "island" with the dust on it under the surface; the higher density solid then sinks to the bottom with the dust; 2) raise the temperature to completely melt the charge again. An equivalent method is to allow the dust to adhere to the side of the seed where it won't interfere with the growth. These methods are admittedly crude, but the alternative is either ending the growth run or making alterations to the grower to allow some mechanical means of clearing the melt surface.

The seed is dipped into the melt, which is at a temperature just above the freezing point of BaF_2. After a small amount of the seed melts, without having it lose contact with the melt, the seed lift mechanism is started. As growth progresses a thin neck is grown, and then the lift rate is reduced so that the diameter increases to the final desired diameter. This diameter is then maintained by manually increasing the pull rate. Pull rates used in this research were between 2.5 and 15 mm/h. The crucible and seed were counter-rotated at 2 and 15 rpm, respectively.

Czochralski growth is an inherently unstable process when examined from the point of view of crystal diameter control[22]. It is this aspect of crystal pulling that has helped maintain the perception of crystal pulling as an "art" instead of a science. Until the advent of accurate temperature and diameter control systems the crystal quality was highly dependent on the operator's skill at maintaining a constant diameter under fluctuating growth conditions.

Manual control of the crystal diameter works sufficiently well for fast pull rates (>25 mm/h), but at low rates (<15 mm/h) it is very difficult to keep the variations less than 20 percent of the diameter. The reason for this is that the edge of the growing crystal can be distinguished from the melt and meniscus only after it has cooled slightly and changed in color. This change in color occurs a few millimeters above the melt surface. At low lift rates the time between a sudden diameter change and the operator's becoming aware of it and reacting, may be on the order of 10 to 15 minutes, which is too long a time period for good control.

Once the desired crystal diameter is reached and a homogeneous region has been grown, doping of the melt can begin.

3.4.1. Doping the crystal

The dopant, CaF_2, is cut into rectangular pieces approximately 8x8x20 mm. The starting material is produced in the same way as the BaF_2 seeds discussed earlier. The dopant is then attached to a molybdenum wire and suspended over the crucible and charge before sealing the furnace chamber.

Considerable difficulties are encountered upon introducing dopant into the melt. The problem is that CaF_2 has a lower density than BaF_2 and tends to float on the top of the melt. Small amounts of CaF_2 are observed to remain on the surface for periods of approximately one minute before mixing with the rest of the melt. While this is not a

long time relative to a slow growth rate, it is long enough for the CaF_2 to "dissolve" some of the grown crystal. Addition of CaF_2 to BaF_2 depresses the melting point of the mixture. The effect of this local lowering of the melting point can reverse the growth and can be severe enough to cause the crystal to completely lose contact with the melt. To overcome this problem a co-axial crucible has been designed and built. The crucible consists of a standard cylindrical crucible with a second, smaller diameter, thin walled cylinder placed inside. Holes around the periphery near the bottom of the cylinder allow the flow of liquid from the outer to the inner portions of the crucible.

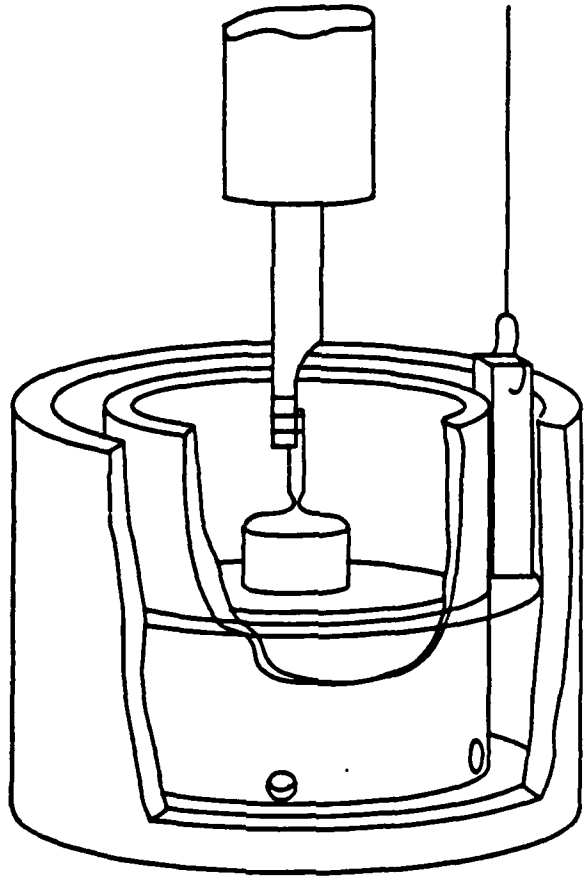

Figure 3.3
Cut-away view of the double walled crucible.

Figure 3.3 shows a cut-away view of this design. CaF_2 is lowered into the outer portion while the crystal is pulled from the inner portion. This crucible eliminates the problem of interaction of the CaF_2 with the crystal before it is thoroughly mixed with the melt. An important limitation of an inner cylinder that is not mechanically attached to the bottom of the crucible is that, because of the low density of graphite relative to BaF_2 (1.8 gm/cc vs 4.89 gm/cc, respectively), the melt depth is limited to a height that is below the point at which the cylinder would float. This means that for BaF_2, the maximum melt depth must be less than 0.37 times the cylinder height.

Once CaF_2 has begun to be incorporated into the melt, as is noted previously, the freezing point is depressed, following the liquidus line on the Ba/CaF_2 phase diagram. If the heater power is not decreased in concert with the increase in concentration, the growth slows and eventually stops and, assuming a constant lift rate, the crystal loses contact with the melt entirely. The rate at which the temperature should be reduced can in theory, knowing the growth rate, be read directly from the phase diagram.

Linear ramps in set point are used once the doping of the crystal has begun. The rate is approximately 2 set points per minute for the successful runs, and is dependent on the initial melt weight and the rate at which dopant was being fed into the melt. Too fast a decrease in temperature results in an uncontrolled increase in diameter while too slow a decrease results in growth stopping and the crystal melting free of the surface.

Growth of the crystal continues until either the dopant has been wholly introduced into the melt or growth is terminated for some other reason. The seed lift rate is then increased along with the heater power and growth continues until the crystal

is free from the melt. At this point great care is needed to prevent cracking of the crystal as the furnace cools to room temperature.

3.4.2. Cool-down cycle for fluoride crystals

Because the voltage output of the pyrometer, or equivalently, the set point of the temperature controller, is dependent on the incident radiation from the furnace, a linear ramp-down in set point results in an inverse fourth power drop in temperature. (pyrometer output is proportional to T^4 - Stefan-Boltzmann law). While this is not crucial during the actual growth of the crystal, it is important to take this into account during the annealing and programmed cool-down. At temperatures below 800 ^{o}C the pyrometer sensitivity is very low, thus the W/Re thermocouple was used from that point down to room temperature. Best results are achieved for temperature cycles similar to the one shown in fig. 3.4, used to cool a 30 x 40 mm crystal. After a short annealing period the temperature is linearly ramped to room temperature. Faster cooling, especially in the lower temperature regions, results in cracked crystals.

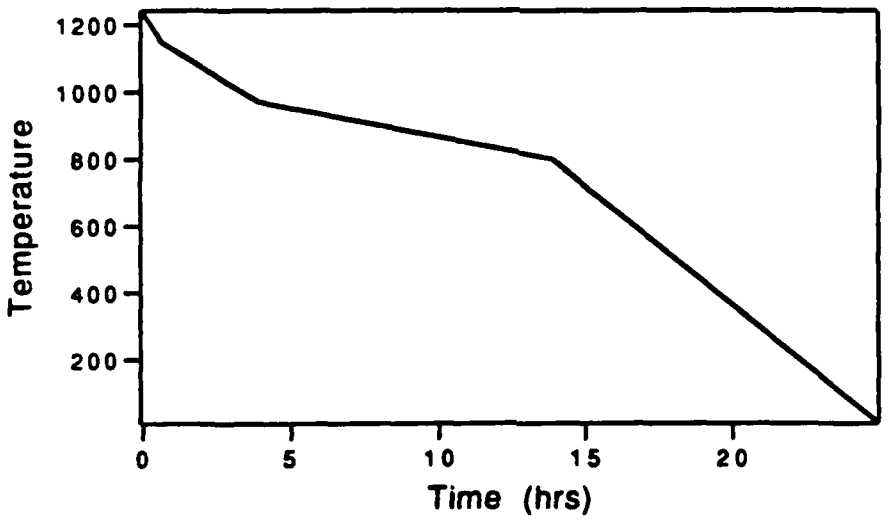

Figure 3.4
Temperature cycle for cool-down of a GRIN crystal.

Crystals of pure CaF_2 are much more thermally robust than the BaF_2 crystals, while combinations of the two are harder than either (as evidenced by effects seen during polishing and by conversations with optical shop personnel at Harshaw crystal Co.)

3.5. Summary

The experimental apparatus consisting of the KAYEX CG800 grower and the doping rod/motor combination that was used as a modification to the grower has been described.

The atmosphere and method of purifying the starting materials was presented along with the results of using different crucible materials. The best crucible material was found to be a graphite crucible with a thin vitreous carbon coating on the inner surface. The shape of the crucible was an important parameter in the growth process. A double walled crucible was fabricated and used to insure mixing of the dopant with the melt.

The procedures that were used to successfully grow a GRIN crystal are outlined. Important factors include control of the diameter of the crystal and a proper cooling cycle.

References for Chapter 3.

---

[1]J. Czochralski, Z. Physik. Chem. **92** (1918) 219.

[2]Meniscus is brighter than the melt due to its concave shape reflecting the brighter, hotter crucible walls (see K. E. Domey, *Solid State Tech.* **41** (1971)).

[3]T. H. Johansen, "On the Theory of the Weighing Method for Automatic Crystal Shape Control in Czochralski Growth," J. Crys. Growth **80** (1987) 343.

[4]A. R. Moore, "Preparation of Single and Multiple P-N Junctions in Single Crystals of Germanium," in *Transistors I*, RCA Laboratories (1956) 77.

[5]H. Nelson, "Continuous-Process Apparatus for Growing Single-Crystal Germanium," in *Transistors I*, RCA Laboratories (1956) 66.

[6]D. A. Petrov and V. S. Zemskov, "Apparatus and Methods for Growing Single Crystals of Semiconductors," in *Growth of Crystals*, Shubnikov and Sheftal (eds), Academy of Sciences Press, Moscow (1957) 207.

[7]Velmex Corp, East Bloomfield, NY.

[8]D. C. Stockbarger, "The Production of Large Artificial Fluorite Crystals," in *Crystal Growth, Discussions of the Faraday Society* (1949) 249.

[9]Ibid.

[10]R. Fauch, R. Reimann, and G. Schwotzer, "Coloration and Luminescence of Oxygenated CaF_2 Crystals," Phys. Stat. Sol. (a) **23** (1974) 69.

[11]Dr. Terry Nestor, Harshaw Crystal Corp., private communication.

[12]I. V. Stepanov and P. P. Feofilov, "Growing of Crystals, Apparatus and Method: Artificial Fluorite," in *Growth of Crystals*, Shubnikov and Sheftal (eds), Academy of Sciences Press, Moscow (1957) 181.

[13]R. Ubrin, R. F. Belt, and V. Rosati, "Preparation and Crystal Growth of Lithium Yttrium Fluoride for Laser Applications," J. Crys. Growth **38** (1977) 38.

[14]John Dodd, Southern Graphite corp., private communication.

[15]Barbara Darnell, Optovac Corp, private communication.

[16]M. S. Abrahams and P. G. Herkart, "Effects of Growth Parameters on Dislocations in CaF2," J. Appl. Phys. **36** (1965) 274.

[17]R. C. Pastor, M. Robinson, and W. M. Akutagawa, "Congruent Melting and Crystal Growth of $LiRF_4$," Mat. Res. Bull. **10** (1975) 501.

[18]Bill King, Cz. growth of MgF_2 at Harshaw Crystal Co., private communication.

[19]E. Schultheiss, A. Scharmann, and D. Schwabe, "Single Crystal Growth and Structure Analysis of $BiLiF_4$," J. Crystal Growth **80** (1987) 261.

[20]Atomergic Chemetal Corp.

[21]Vitre-Graf Corp., subsidiary of HITCO, Gardena, CA.

[22]T. Surek, "Theory of Shape Stability in Crystal Growth from the Melt," J. App. Phys. **47** (1976) 4384.

CHAPTER 4

GRIN Crystal Growth Results

4.1. Introduction

This chapter is devoted to presenting data on the gradient-index (GRIN) crystals that were grown during the course of this research. Many fluoride crystals were grown, both homogeneous crystals of calcium fluoride or barium fluoride and also crystals with compositional and index changes. Homogeneous crystals were grown primarily to become familiar with the procedures necessary for growing a crystal by Czochralski's method and to determine experimentally the extent of the existence of a solid solution of CaF_2 in BaF_2. The homogeneous crystals grown also gave a baseline from which to judge the performance of the GRIN crystals in terms of transparency and homogeneity.

Several types of measurements are made to determine the magnitude of the compositional/index change. A Mach-Zehnder interferometer is used to measure the index profiles. These profiles are compared to the data from a quantitative electron microprobe analysis of the composition. The index profiles are then compared to the index profiles predicted by the algorithm developed in Chapter 2, which is based on the growth parameters. Further measurements are made using a moiré deflectometer which gives information on the index profiles and dispersion of the GRIN crystals in the visible and ultraviolet regions of the spectrum. The deflectometer measurements are presented in Chapter 6, after the theory for the deflectometer has been presented.

4.2. Homogeneous Crystals

A primary concern in the growth of solid solutions from a two component system is the extent of the solubility of one component in the other. As a starting point for determining the solubility extent of CaF_2 in BaF_2 a series of small charges were carefully melted in the grower furnace and allowed to freeze in the crucible without pulling a crystal. These crystals were for the most part, once oxygen contamination had been reduced, colorless for concentrations less than 5 weight percent CaF_2. At 6 weight percent concentrations and higher the melts became increasingly more cloudy, and when frozen showed Rayleigh scattering. This is roughly in accordance with the data of Chernevskaya and Ananeva[1] which showed via X-ray analysis that for concentrations above 6 to 8 percent the solid separated into two phases: a BaF_2 rich phase and a CaF_2 rich phase. The presence of these two microscopic crystalline phases, each with a different composition and a different index of refraction, accounts for the scattering. Scattering that is noticeable to the unaided eye at any level is not acceptable. The degradation of the wavefronts passing through the crystal, which increases with decreasing wavelength causes the crystal to become for all practical purposes opaque at uv wavelengths. With this in mind, it was decided to only attempt to dope the melts to concentrations not exceeding approximately 4 weight percent CaF_2.

4.2.1. Growth of homogeneous fluoride crystals

The first crystals grown were composed of pure calcium fluoride or pure barium fluoride. The starting materials were either "random cuttings" from optical grade crystals from Harshaw Crystal Co., or 99.95 % "phosphor grade" CaF_2 powder or "reagent grade" BaF_2 powder, both from Johnson Matthey. The major difference found when melting these two forms of crystalline material was that the powder form rarely fused and melted without incorporating some oxide into the melt, probably due to

the presence of water in the powder. Using PbF_2 as a scavenger eliminated this problem (see Chapter 3). The cuttings from Harshaw consistently melted into a transparent liquid without any evidence of Ca/BaO on the surface. Either form of starting material demonstrated oxygen absorption from the graphite crucible if the crucible had not been prepared properly. Differences between the two types of materials due to impurity level differences were not evident. For these reasons and because the price differential was an order of magnitude or more, the powder from Johnson Matthey was used as the starting material for the bulk of the growth runs carried out. A drawback to this choice was that the main impurity in the BaF_2 powder was SrF_2 (its presence was determined by a semi-quantitative electron microprobe analysis) and this caused the BaF_2 to become more brittle[2] and more easily subject to breakage from thermal stress induced strain.

The first experiments pointed out the importance of careful preparation of the graphite crucible. Crucibles moved into room air from a vacuum for even a short period (while loading the crucible, for example) absorbed gas into the porous structure of the crucible. The crucible slowly released this absorbed gas into the melt during the growth run unless it was held in a moderately high vacuum for several hours prior to heating. This effect was reduced by keeping the crucible in an atmosphere of nitrogen between growth runs, as opposed to keeping it under vacuum, and by introducing nitrogen gas instead of room air when bringing the furnace chamber to room pressure. When two or more crystals were pulled from a melt contaminated with oxygen, the crystals grown with slower lift rates showed a greater rejection of the oxygen. This rejection was evident as the lighter color or absence of color altogether in the more slowly pulled crystals as opposed to the tan or brown color of crystals grown at higher lift rates.

4.2.2. Properties of homogeneous fluoride crystals

Several pure CaF_2 crystals that were colorless and transparent were pulled from the melt. Many BaF_2 crystals, also colorless and transparent were pulled while learning to use the CG800 apparatus and while determining the best crucible type and the best crucible/hot zone configuration.

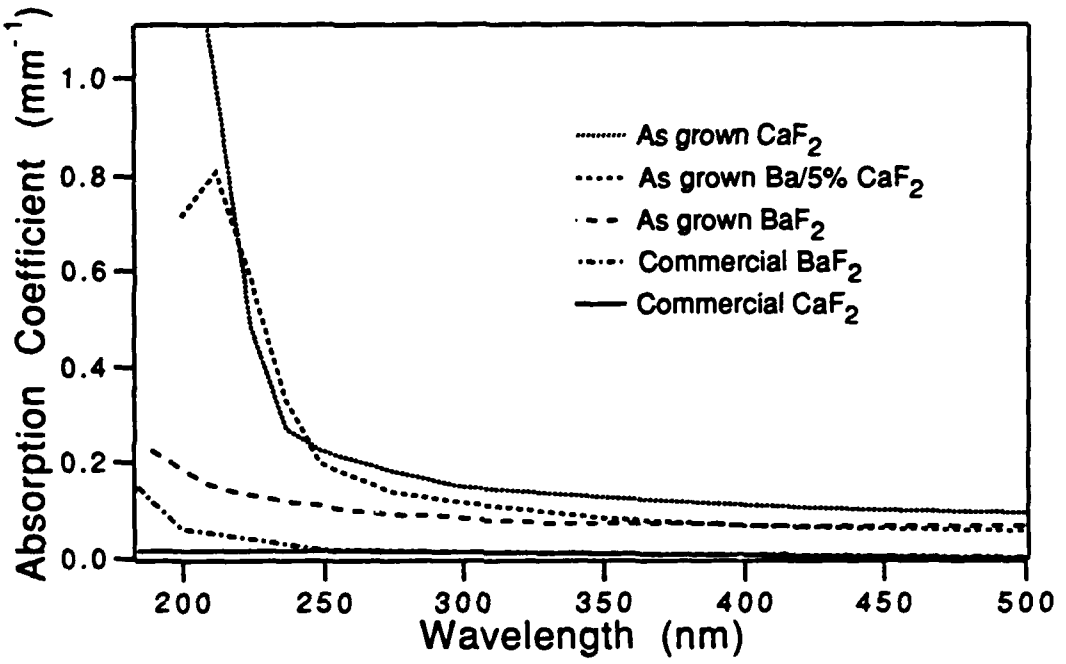

Figure 4.1
Absorption for crystals of various compositions.

Figure 4.1 shows plots of absorption versus wavelength for homogeneous pulled crystals of BaF_2 and CaF_2, and for a 5 mole % Ca/BaF_2 homogeneous composite that was made by melting a mixture of the two components together and then slowly cooling the result. Data is also included for commercially available fluorides[3]. Data were taken using a Perkin-Elmer model 330 spectrophotometer. The transmission data was then converted to absorption data while also compensating for Fresnel losses. While these crystals did not transmit far uv wavelengths to the extent that the

commercial crystals did, they are more than adequate for the spectral region of interest, namely 0.250 - 0.400 μm This data also demonstrates that the addition of small amounts of CaF_2 to BaF_2 does not affect its transmission in the spectral range measured, beyond reducing its transmission to the level of the pure CaF_2.

The homogeneous CaF_2 crystal is not quite colorless, having a slight tan hue, indicating the presence of oxygen. This conclusion is substantiated by the above data, which shows the 210 nm oxygen absorption as is discussed in Chapter 3, along with a uniform baseline shift in absorption. The use of the vitreous carbon crucible considerably reduces the coloration and presumably also the oxygen. This change is reflected in the excellent absorption curves of the "as grown" BaF_2 crystal.

Care in handling both the CaF_2 crystals and the BaF_2 crystals had to be exercised since both types had a cleavage on the (111) plane. This was most evident when cutting the crystals in preparation for analysis. A Buehler Isomet diamond saw was used to slice sections of the crystals. Fractures would often start on the cut face with small sections cleaving off if the cutting speed were too fast. It was found that approximately 3 cm/h was an appropriate cutting speed for a 3 to 4 cm diameter crystal.

4.3. Growth of GRIN crystals

Once the charge had been melted and a small amount of homogeneous BaF_2 crystal had been grown, the CaF_2 doping material was lowered into the melt. Lowering rates for the dopant were between 5 and 20 g/h, while pull rates for the growing crystal varied from 2.5 to 20 mm/h, with most of the better quality crystals being grown with pull rates < 10 mm/h.

During the course of this research approximately 40 crystals were grown; 33 homogeneous crystals and 7 crystals with a composition gradient. The number of GRIN crystals grown was not large but was sufficient to demonstrate the feasibility of fabricating uv transmitting index gradients by this method. The information presented on the GRIN crystals was limited to three crystals which were typical of the crystals grown in general, based on transmission properties and shape. These three also had the best index of refraction profiles of the GRIN crystals grown, in terms of smoothness of the profile. This was primarily due to careful growth control during their fabrication (without periodically removing the crystal from the melt, which was sometimes necessary to determine the diameter during quickly changing growth conditions).

crystal	initial melt	pull rate (mm/h)	CaF_2 added	size (dia.x len.)
mh46	479 g	12.5	14.4 g	5 x 30 mm
mh721	341 g	5.0	6.5 g	20 x 50 mm
mh614	350 g	7.6	16.6 g	20 x 30 mm
crucible rotation: 2 rpm ccw			crystal rotation: 15 rpm cw	

Table 4.1
Growth parameters for 3 GRIN crystals.

4.3.1. GRIN crystals' properties

4.3.1.1. Transmission

The homogeneous (BaF_2) region of most of the crystals grown has a spectral transmission that is the same as for the homogeneous crystals grown earlier. The gradient region of the GRIN crystals also appears colorless and transparent.

Accurate spectral transmission measurements of the GRIN regions, especially in the uv, was not possible using the Perkin-Elmer spectrophotometer that was used to measure the homogeneous samples. It is quite difficult to measure the transmission of a GRIN sample using a standard spectrophotometer because of the tendency of the index gradient to deflect light out of the optical system of the spectrophotometer. Because this effect is wavelength dependent, the transmission data obtained is not reliable. Measurements of the transmission of homogeneous Ba/CaF_2 crystals discussed in the previous section indicate that the transparency of a crystal is not adversely affected by the presence of the dopant, to the extent that it has transmission similar to that of the pure CaF_2 crystals grown during the course of this research.

4.3.1.2. Index Profile measurements

Initial measurements of the GRIN profiles that were fabricated were carried out using a Mach-Zehnder interferometer. This interferometer was built at The Institute of Optics for the measurement of GRIN index profiles. It has a precision error of approximately 1 percent for index changes similar in magnitude to those of the crystals grown. Figure 4.2 shows a photograph of the actual Mach-Zehnder (single-pass) fringe pattern for a section of crystal mh614 cut parallel to the growth direction. The scan of the index profile was made at a wavelength of 632.8 nm. The thickness of the sample is 2.39 mm.

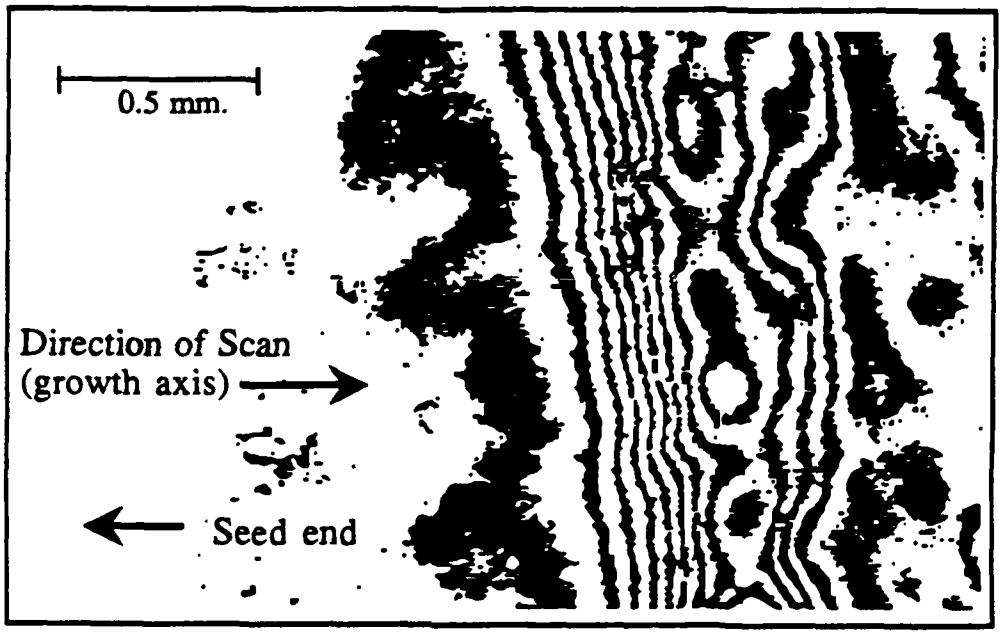

Figure 4.2
Fringe pattern in the image plane of the Mach-Zehnder interferometer for the index gradient region of crystal mh614.

As can be seen in the photograph, the fringe pattern initially consists of fairly straight line fringes. After several fringes the pattern shows the existence of "islands" or "bumps" in the index profile. These bumps are most likely caused by a variation in the value of the segregation coefficient which then causes local variations in the concentration of dopant. As is discussed in Chapter 2, this variation in segregation can be attributed to a growth rate that is too fast for the rate of mixing in the melt. A fast growth rate can occur when the furnace temperature is lowered too quickly and supercooling results. In this case portions of the interface grow faster than others and these projecting areas crystallize with a higher concentration of dopant than adjacent, more slowly growing regions[4]. This substructure is hexagonal in cross-section and can become quite large.

Hexagonal regions as large as 1 mm were observed at the growth interface of a Ba/CaF_2 composite crystal that was suddenly lifted from the melt and allowed to cool. This crystal, mh421, was grown with a pull rate of 12 mm/h with a concurrent lowering of the heater temperature which caused an increase in the growth rate. The starting melt composition for mh421 was 40 mole % CaF_2. The presence of substructures of this type points out the importance of accurate control of the growth rate of the crystal to avoid their occurrence.

Figure 4.3
Fringe pattern in the image plane of the Mach-Zehnder interferometer for the index gradient region of crystal mh721.

Crystal mh721 was grown with less dopant and at a slower growth rate to avoid the above problems, resulting in a shallower index profile, shown in fig. 4.3. The sample thickness was 3.92 mm and the wavelength was 632.8 nm.

Scans of the refractive index profiles for three crystals are shown in figs. 4.4a - 4.4c. Corresponding data from quantitative electron microprobe analyses of the

concentration of calcium and barium are overlaid on each profile. The microprobe data is an average over three scans. The error bar shown in each figure represents the mean value of the standard deviation for the three scans. The concentration data is converted into index data using a linear model. The model assumes that the index scales linearly with composition when the composition is expressed as moles per unit volume. This model is discussed in detail in Appendix B.

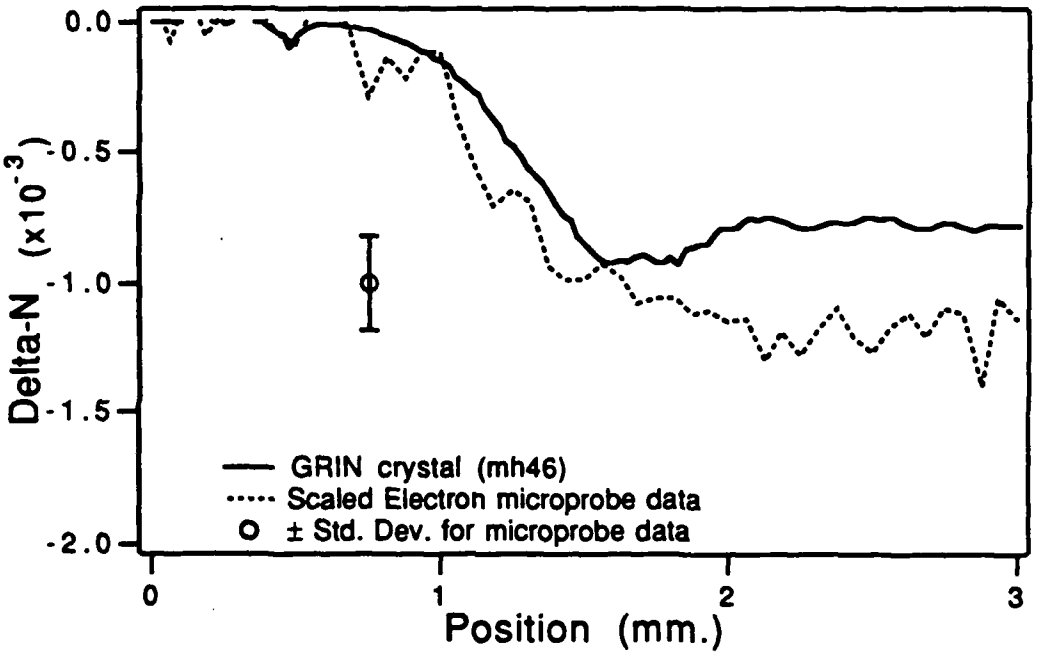

Figure 4.4a
Data for sample mh46.

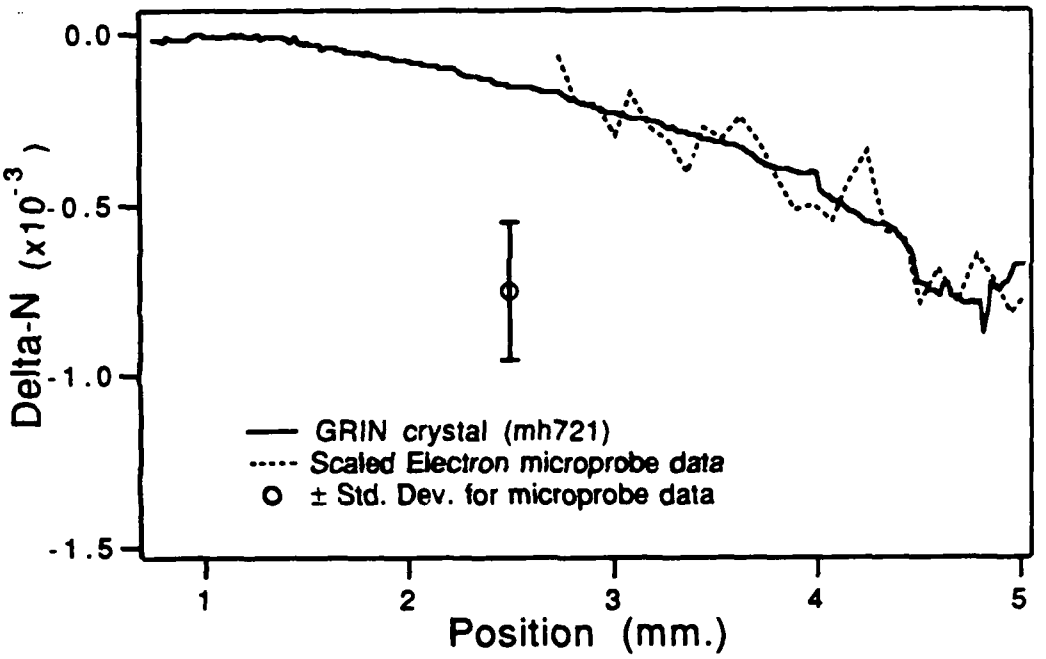

Figure 4.4b
Data for sample mh721 (see fig. 4.3).

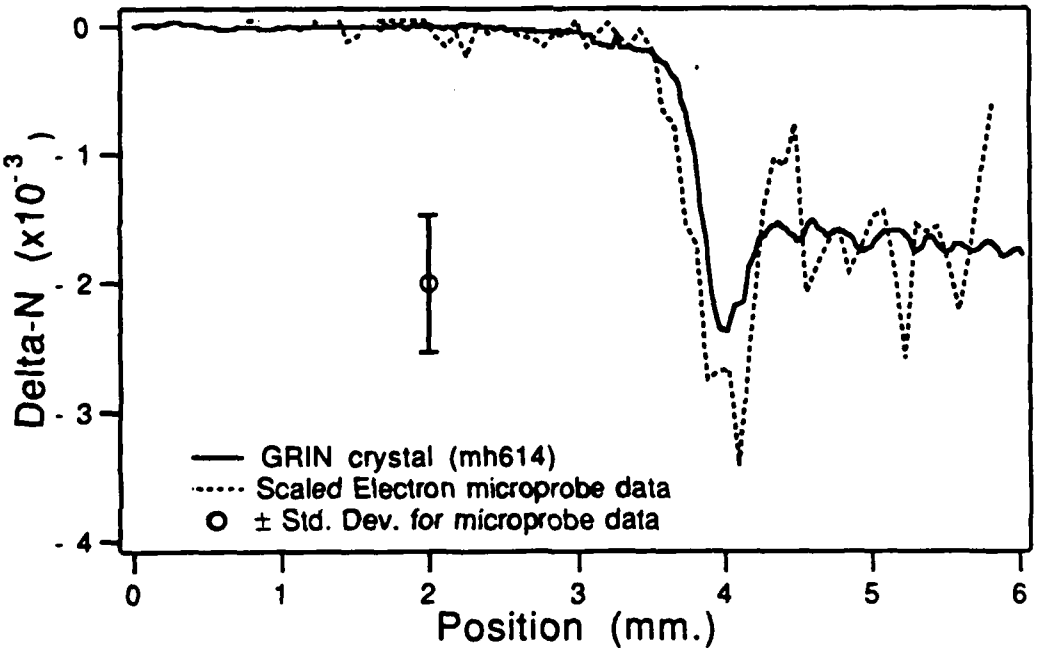

Figure 4.4c
Data for sample mh614 (see fig. 4.2).

In each of these figures it can be seen that the microprobe data for the composition profiles closely follows the shape of the index of refraction profiles. The relatively large size of the standard deviation for each set of microprobe data is due to a combination of the statistical fluctuations in the x-ray counts and irregularities in the surface of the crystal. An additional source of differences between the two types of scans is that they were registered spatially relative to each other to approximately ±25 μm. As can be seen in fig. 4.2 there is a variation in index profile as a function of scan position across the gradient region. Differences of the magnitudes seen in figs. 4.4a-c can easily be explained by small registration differences between the microprobe scan and the interferometer scan. The important point to be made by comparing these two types of data is that the index of refraction profiles are caused by actual changes in composition, and are not caused by some other mechanism such as stress.

The expected concentration profiles can be determined from the theoretical model described in Chapter 2, which is based on the actual growth parameters. The modelled concentration profiles are shown in figs. 4.5a and 4.5b, along with the index profiles for comparison. The calculated concentration profiles are again scaled using the linear model discussed in Appendix B to allow a direct comparison with the measured index profiles.

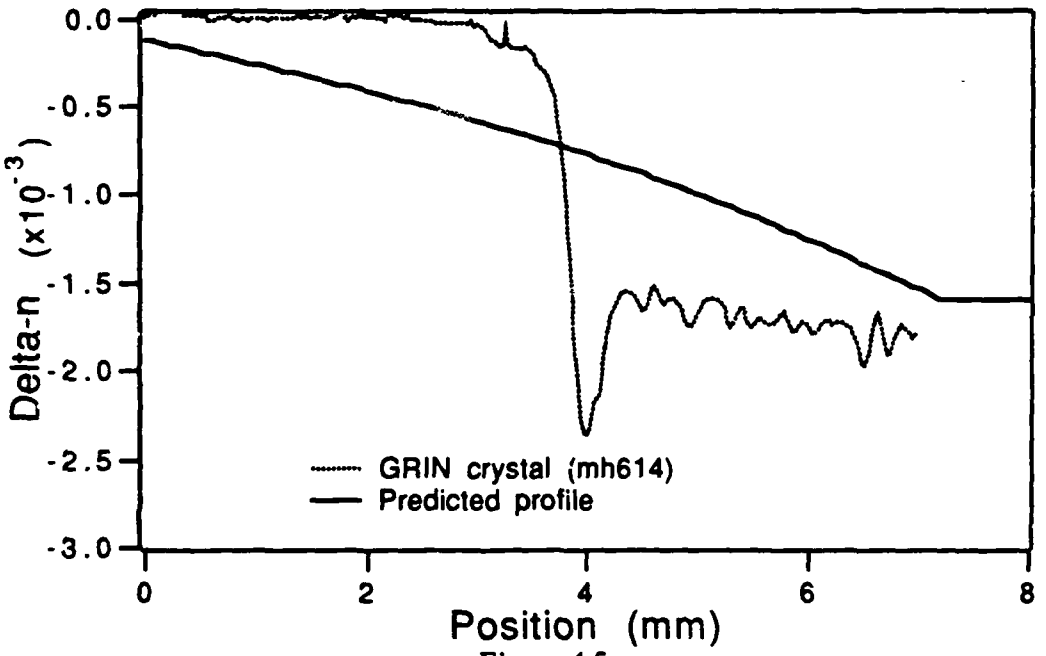

Figure 4.5a

Modelled index profiles based on growth parameters, compared with the measured profile for mh614.

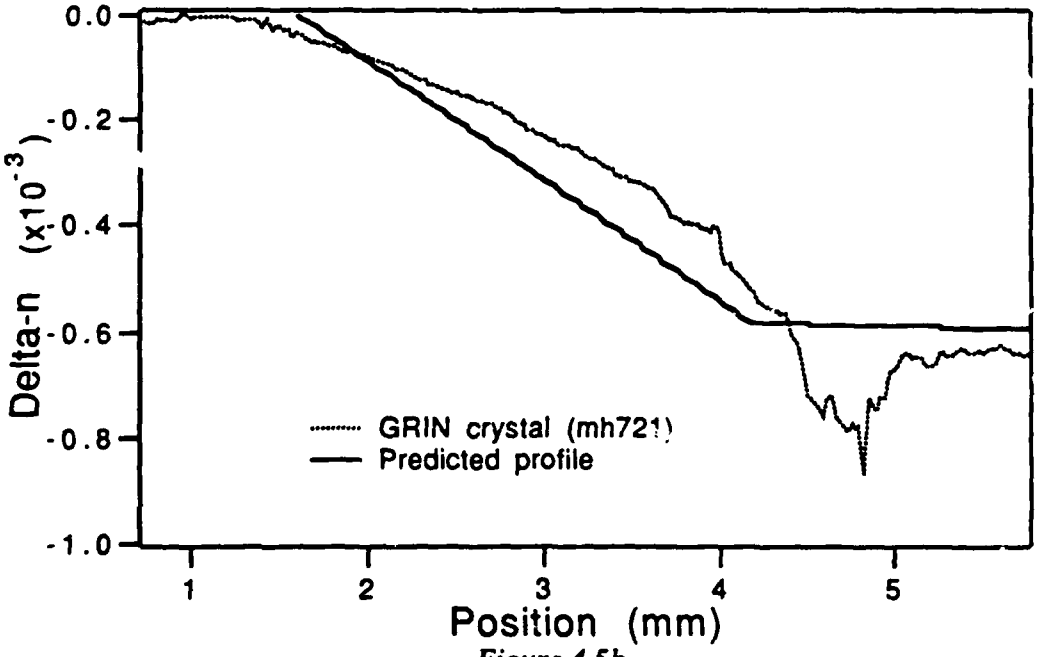

Figure 4.5b

Modelled index profile based on growth parameters compared with the measured profile for mh721.

The theoretically predicted profiles are very close to the actual profiles in terms of the magnitude of the change to be expected for both crystals. The predicted profile for crystal mh614 however, is not at all similar in shape to the measured profile. To determine what might cause this difference, various parameters were varied to determine their effect on the predicted profile. It is found that a change in the growth rate parameter in the model changes the slope of the predicted curve without greatly changing the maximum index change reached. From this it can be deduced that the actual growth rate must have been slower than that indicated by the pull rate and the crystal diameter. This is in fact known to be the case because the addition of calcium fluoride depresses the freezing point of the melt.

The growth rate can be determined from the pull rate and the diameter of the crystal as a function of time. Even though the height of the crystal is carefully noted as a function of time during growth, this value does not take into account the amount (or height) of crystal that extends below the melt surface. This can be a non-trivial distance if the melt/crystal interface is non-planar, as is the case for the current furnace arrangement. The effect of not knowing the exact size of the crystal pulled as a function of time is that the exact melt size is unknown. The theoretical profiles shown are dependent on the size of the melt and thus the uncertainty in the growth rate can be translated into an uncertainty in the predicted profile.

For sample mh721, grown with a slower pull rate and a more uniform diameter, the predicted profile follows the measured profile much more closely.

There are many other factors affecting the actual shape of the index profile and the extent to which it differs from the theoretically predicted shape. One factor is that complete mixing is not achieved immediately between the outer portion of the crucible where the CaF_2 is added and the inner portion where the crystal is pulled. This results

in a temporal lag between concentration changes in the outer crucible area and concentration changes in the crystal. This could also cause a more complex variation in the shape of the concentration profile, depending on the functional form of the mixing rate between the inner and outer portions of the crucible. A second possible cause for the disparity in the shape of the predicted profile versus the grown profile is that mixing in the inner portion of the crucible may not be complete. The existence of non-mixing cells in the crucible during Czochralski growth is demonstrated both theoretically and experimentally by Carruthers and Nassau[5]. The presence of non-mixing cells causes a positional dependence of the CaF_2 concentration in the crucible and also affects the shape of the concentration profile in the crystal. Unfortunately, it is beyond the scope of this thesis to investigate the actual effects of fluid flow variations on the concentration profile.

Despite the possible existence in this growth system of the above non-ideal mixing mechanisms, the agreement between the two profiles for both crystals demonstrates that the actual growth processes can be fairly well described using the assumptions made in Chapter 2. These assumptions are that 1) the crystal does not extend below the surface of the melt, 2) the growth is slow enough that the effective segregation coefficient is close to that of the ideal segregation coefficient, and that 3) mixing occurs immediately between the two regions of the crucible.

4.3.2. Other GRIN fluoride crystals

The phase diagrams for several other mixtures of fluorides show promise for the formation of a solid solution GRIN crystal. Among these are combinations of either CaF_2 or BaF_2 and many of the Lanthanides. In particular, the LaF_3/BaF_2 phase diagram looks interesting both because of the existence of a solid solution and because of the large index of refraction difference between LaF_3 and BaF_2 (0.1264 at a wavelength of 546.1 nm). Unfortunately, LaF_3 is very birefringent. Nonetheless it was decided to pull a composite crystal, allowing the segregation that occurs naturally to determine the form that the concentration change would take. The segregation coefficient at this concentration is approximately 2.0. Several crystals were grown with starting compositions of 5 weight percent LaF_3. The largest of these was 25 mm in diameter by 30 mm in length. Quantitative interferometric analysis of the crystal was not possible because of its polycrystalline nature. Each crystalline region appears to have a different orientation from that of its neighbors. Thus each region presents an optical path length that is different, for a given direction, from its neighboring region. The phase change due to the varying birefringence is greater than that of the index change from the compositional variation, which causes an unrecognizable fringe pattern in the image plane of the interferometer.

A second choice for the manufacture of uv transmitting GRIN crystals is the combination of BaF_2 and SrF_2. Although the difference between the indicies of refraction is not as large as for CaF_2 and BaF_2, there exists a solid solution of these two components over a wider compositional range, thus possibly giving a larger index of refraction variation. No experiments were conducted using this fluoride combination.

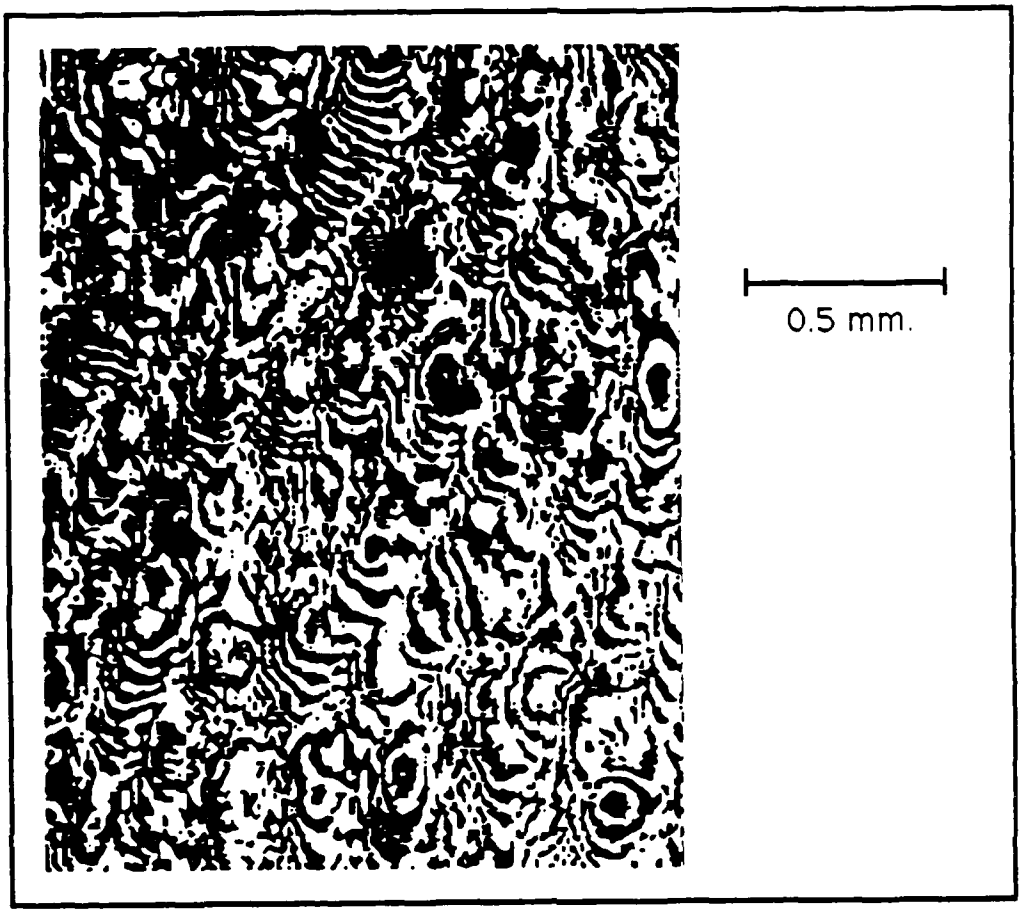

Figure 4.6
Interferogram of a section of a LaF_3/BaF_2 composite (using He-Ne laser). The sample thickness is 3.75 mm.

4.4. Summary

The results of the growth of homogeneous and GRIN fluoride crystals have been presented. It was found that the spectral transmission of homogeneous mixtures of barium and calcium fluoride was satisfactory from the visible down to a wavelength of 230 nm in the uv. The presence of an absorption peak due to the incorporation of oxygen was most likely the limiting factor in the uv transmission of these mixtures.

Several GRIN crystals were grown with varying amounts of calcium fluoride. Quantitative electron microprobe analysis of the concentrations of barium and calcium confirmed the presence and magnitude of the index changes and verified that the interferometrically measured index changes were not due to stress in the crystal.

It was found that the model for the concentration as a function of the growth parameters developed in Chapter 2 qualitatively matched the index profiles that were grown. The primary limiting factor in modelling the growth of the crystals was found to be the difficulty in controlling the growth rate as the growth conditions changed during the doping process.

References for Chapter 4.

[1]E. G. Chernevskaya and G. V. Ananeva, "Structure of Mixed Crystals Based on CaF_2, SrF_2, and BaF_2," Sov. Phys.-Sol. St. **8** (1966) 169.

[2]G. Bastien, Harshaw Crystal Co., private communication.

[3]*Harshaw Crystal Optics*, Engelhard Corp., 1988.

[4]D. A. Petrov and B. A. Kolachev, "Impurity Redistribution During Crystallization and way this Appears in the Crystal Structure," in *Growth of Crystals*, v.**1**, Shubnikov and Sheftal, eds., Moscow (1957).

[5]J. R. Carruthers and K. Nassau, "Nonmixing Cells due to Crucible Rotation during Czochralski Crystal Growth," J. App. Phys. **39** (1968) 5205.

CHAPTER 5

Deflectometer Theory

5.1. Introduction

The purpose of this chapter is to examine in detail the theory of the moiré deflectometer and present an analysis of its use in precision measurements of index of refraction profiles. Throughout this chapter the word "grating" is used interchangeably with "Ronchi ruling" or "Ronchi grating" and, in either case, refers to a transparent plate with an overlying pattern consisting of alternating opaque and transparent bars of equal thickness. The theory presented here differs from other analyses given in the literature, primarily due to variations in the optical configuration used for the deflectometer but also due the method of recovering the phase of the moiré fringe pattern. The phase of the fringe pattern is recovered using a quasi-heterodyne method known as harmonic phase modulation. A thorough theoretical analysis of this method is presented along with an investigation of the types of errors that can arise from incorrect phase modulation.

5.1.1. The Talbot interferometer

The Talbot interferometer[1] is the direct historical predecessor of the moiré deflectometer and, while the differences between the two are not major, they are important. The basic Talbot interferometer consists of a collimated beam of light followed by two separated identical gratings, parallel to each other, with a transparent object which is to be analyzed placed between them. A real fringe pattern can then be seen immediately beyond the second grating. The fringe pattern in simplest terms is the moiré pattern formed when the first grating's shadow, distorted by its passage through

the object, falls on the second grating. In practice the analysis is not so simple because diffraction plays a large role for geometries in which the gratings are separated by any appreciable distance. A very short distance behind the first grating the overlap of the different diffraction orders quickly blurs any "shadow" the bars of the grating might have. The degradation due to this blurring can be overcome by taking advantage of a phenomenon known as self-imaging. At periodic distances behind the grating high contrast images of the grating form without the use of any intermediate optics. This self-imaging phenomena is termed the Talbot effect because Talbot[2] was the first to describe the self-imaging of periodic objects.

Nishijima and Oster[3] discuss the use of the Talbot interferometer for the measurement of index of refraction gradients and the measurement of lens aberrations. Oster et al.[4] discuss the interpretation of the moiré patterns formed by the Talbot interferometer and also analyze different configurations of the gratings and the phase object, including having the object precede the first grating so that the wavefront is distorted before passing through the first grating. This configuration of the Talbot interferometer, with the object between the source and the first grating, is termed a "moiré deflectometer" by Kafri[5] (who claims to have invented the method), with the addition of a ground glass screen placed immediately after the second grating. The name moiré deflectometer is a more descriptive designation for this configuration since in a geometrical analysis it is ray deflections by the object under test that cause the formation of a moiré pattern in the output plane of the instrument. Figure 5.1 shows a schematic of the moiré deflectometer.

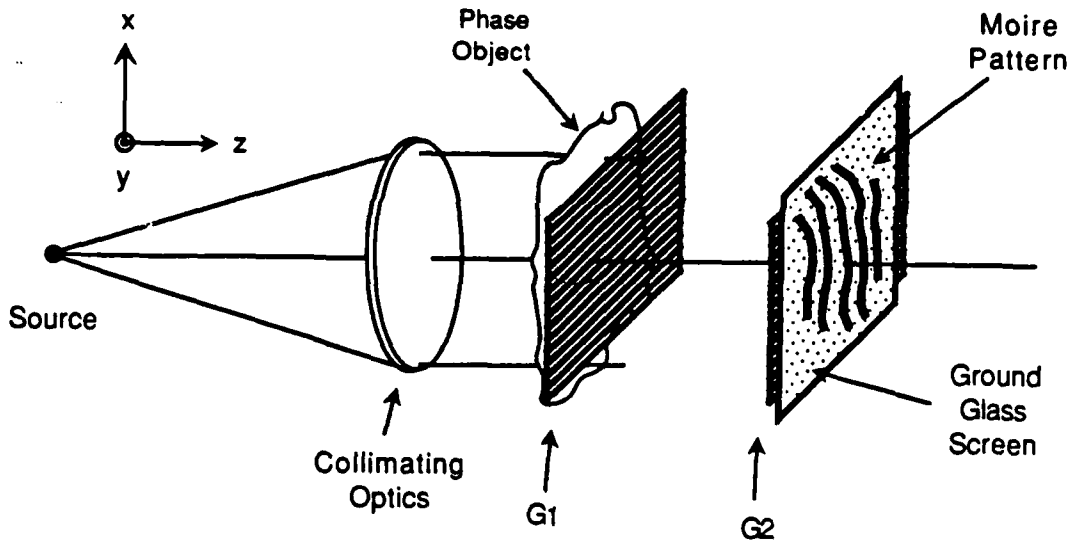

Figure 5.1
Schematic of the moiré deflectometer. The moiré deflectometer differs from the Talbot interferometer only in the placement of the object and in the addition of a ground glass screen after the second grating.

5.2. Deflectometer Theory

5.2.1. Ray-based analysis

To begin the analysis of the moiré deflectometer it is informative to start with the general form for the moiré pattern formed when two gratings, or Ronchi rulings, are placed on top of each other with an arbitrary orientation relative to each other. The coordinate system is chosen so that the y direction is parallel to the first grating's lines and the z direction is parallel to the normal to the grating plane. The second grating is oriented so that its lines are running at an angle φ relative to the first grating. Figure 5.2 shows this arrangement. Moiré fringes are formed with the fringes running at an angle of $\frac{\varphi}{2}$ relative to the x axis. This is analogous to the case of two plane waves interfering at an angle of φ.

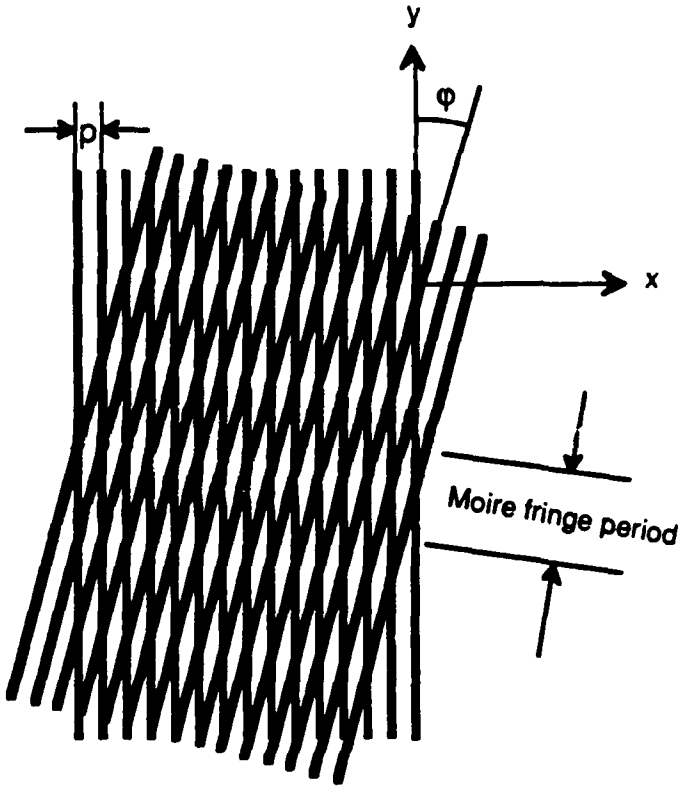

Figure 5.2
Two Ronchi gratings placed on top of each other with one grating rotated by an angle φ.

For ease of analysis the moiré deflectometer is operated in the "infinite fringe" mode, where φ is zero and the first moiré fringe is located at infinity. In this case the only fringes that are present are ones due to ray deflections caused by the sample. Fringes that are present due to a relative rotation of one grating are the moiré equivalent of tilt fringes in an interferometer. Their presence can aid in the visual analysis of a fringe pattern but are usually not helpful when an automated fringe analysis is carried out.

5.2.1.1. Path through gradient sample

Figure 5.3 shows the path a ray of light follows as it travels through a plane-parallel slab of gradient-index material. The index gradient is assumed to be in the x

direction, perpendicular to the initial ray path which is parallel to the surface normal of the slab.

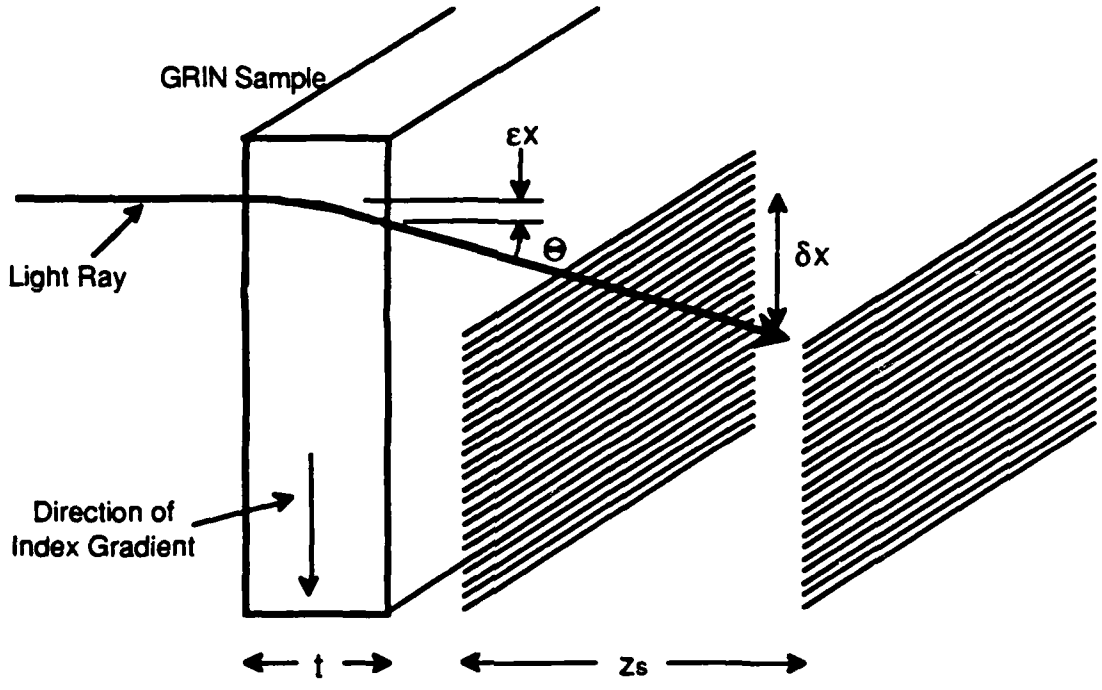

Figure 5.3
Exaggerated ray path through GRIN slab.

After refraction at the planar first surface, the ray path does not change direction but as it continues to travel through the medium it gradually bends towards the region of higher index of refraction. A mathematical treatment of the ray path for gradient-index media is given by Gregorka[6]. For the case discussed, that of a plane parallel slab, the ray undergoes a vertical translation of ε_x as it moves through a slab of thickness t. The ray exits the slab at a (paraxial) angle to the horizontal of

$$\Theta = t\left(\frac{n_{out}}{n_{in}}\right)\frac{\partial n}{\partial x} \quad . \tag{5.1}$$

where n_{in} is the index at the point where the ray enters the sample and n_{out} is the index at the point where the ray exits the sample. In thin slabs where the index gradient is

small, the distance ε_x can be considered negligible and n_{in} is approximately equal to n_{out}. For example, in a sample with a linear change in index of refraction of 0.10 over a distance of 3 mm (which is a relatively large index gradient) with a slab thickness of 1 mm, ε_x is 63 μm and $\frac{n_{out}}{n_{in}} = 1.00130$. While there is a small error in the calculated position of the ray using this approximation the error in calculating the exiting ray angle is negligible. It is this ray angle deviation from the horizontal, Θ, that is measured by the moiré deflectometer. As the ray continues through the first grating to the second grating it can be seen that the ray is deflected in the x direction by an amount

$$\delta x = \Theta z_s \tag{5.2}$$

relative to an undeviated ray with the same initial height and direction. This is the amount that the local "shadow" of the first grating has shifted. It is this shift in the apparent position of the lines of the first grating that forms a moiré pattern with the lines of the second grating. These fringes are straight and parallel to the y direction. A full fringe can be seen on a screen behind the second grating when the ray has been translated a distance $\delta x = p$, where p is the period, or pitch, of the gratings. Thus if m is the number of moiré fringes present, the index gradient is related to the number of fringes by

$$\frac{\partial n}{\partial x} = \frac{mp}{tz_s} . \tag{5.3}$$

This is very similar to the relationship for a lateral shearing interferometer[7].

From eq. (5.3) it can be seen that the sensitivity of the deflectometer for a given sample is proportional to the separation of the gratings and inversely proportional to the grating period. If δm is the minimum fractional fringe that can be detected, the minimum angle that can be detected is

$$\delta\Theta = \delta m \frac{p}{z_s} . \tag{5.4}$$

If δm is 0.01, for a grating with a period of 25 μm and a separation of z_s= 10 mm, then $\delta\Theta$ = 2.5 x 10^{-5} rad. (= 5.0 arcsec.) which indicates that the moiré deflectometer can be extremely sensitive to ray deflections.

There are several important points to be made at this time. The first point is that the only requirement on the source size is that it be small enough that it is well collimated. A lack of collimation results in a reduction in the contrast of the fringe pattern as the shadow of the first grating's bars on the second grating is blurred. Following this reasoning, achieving high contrast for a particular experimental configuration is equivalent to requiring that the source size, s, is such that

$$s \leq \frac{fp}{4z_s} . \tag{5.5}$$

Thus s must be less than 150 μm, (where f (= 300 mm) is the focal length of the collimating lens, p (= 25 μm) is the grating period, and z_s (= 12.5 mm) is the grating separation) which is an acceptable size for a pinhole.

The second point to be made by this analysis is that the deflectometer sensitivity and the fringe pattern are independent of any direct dependence on the wavelength of the source illumination. The only place wavelength dependence plays a role is in the wavelength variation of the index of refraction profile. The wavelength independence of the fringe pattern is an important feature of the moiré deflectometer, especially if dispersion measurements of the index of refraction profile are to be made.

5.2.1.2. Phase Retrieval

Once the phase of the fringe pattern has been recovered, the index of refraction, apart from a constant, can be calculated. The relationship between the index of refraction at a point located at x and the recovered phase is

$$n(x,\lambda) = \frac{p}{t z_s} \int_0^x \text{phase}(x,\lambda) dx + \text{constant} \ . \tag{5.6}$$

Since the phase is sampled at N discrete points the equation for the calculated index of refraction becomes

$$n(x_m,\lambda) = \frac{p}{t z_s} \sum_{m=1}^{N} \text{phase}(x_m,\lambda) \delta x_m + \text{constant}. \tag{5.7}$$

The constant of integration (or summation) is the base index of refraction and is assumed known.

5.2.2. Diffraction analysis

The preceding discussion neglects any role diffraction might play. This is not necessarily a good assumption even when gratings with relatively coarse periods are used. For the above deflectometer arrangement the first diffracted order of the first grating has deviated a distance of $\delta x = \frac{\lambda}{p} z_s$ from the zeroth order. For λ = 500 nm, p = 25 μm,. and z_s = 10 mm, δx = 200 μm, which is quite large relative to the grating period. It is not immediately clear in this case whether or not the preceding ray based analysis holds, except when very coarse gratings are used or when the second grating is located at one of the self-images of the first grating. It is also not clear what effect the phase distortions introduced by the object have on the position and/or quality of the self-images. In order to determine more precisely what form the image at the detector

takes, it is necessary to perform a wave based analysis of the deflectometer for an arbitrary phase object.

5.2.2.1. Image plane distribution

In this section the diffraction theory for the electric field amplitude as it traverses a gradient-index sample and then passes through the deflectometer is examined. The sample is assumed to act as a transparent phase object and the wavefront exiting it is represented as an angular spectrum of plane waves.

The transmission functions of the two parallel gratings G_1 and G_2 can be written as the pair of infinite series

$$G_1 = \sum_{n=-\infty}^{+\infty} C_n \exp\left[\frac{2\pi i}{p} nx\right]$$

and

$$G_2 = \sum_{m=-\infty}^{+\infty} C_m \exp\left[\frac{2\pi i}{p} m(x+\Psi)\right], \tag{5.8}$$

where p is the grating's period and Ψ is the spatial shift of the origin of the second grating relative to the first grating. The field distribution immediately after the first grating is u(x,y,0+) and is simply the product of the transmittances of the grating and the object, U_0:

$$u(x,y,0+) = U_o G_1 \ . \tag{5.9}$$

In order to determine the field at the second grating, positioned a distance z_s along the optical axis, it is convenient to work in Fourier space using an angular spectrum representation[8] of the field and of the transmittances of the gratings. The angular spectrum of a function F(x,y) is defined as (using the Fourier transform)

$$\tilde{F}(\nu,\mu) \equiv \iint_{-\infty}^{+\infty} F(x,y) \exp(-2\pi i(\nu x + \mu y)) dx dy \ .$$

Each grating is then represented as a series of shifted delta functions in Fourier space:

$$\tilde{G} = \sum_{n=-\infty}^{+\infty} C_n \delta\left(\nu - \frac{n}{p}\right)\delta(\mu) \quad , \tag{5.10}$$

and translation along the z axis becomes multiplication in Fourier space by the function T(z), where

$$T(z) = exp\left[\frac{2\pi i}{\lambda} z\sqrt{1-\lambda^2\left(\nu^2+\mu^2\right)}\right]. \tag{5.11}$$

The angular spectrum of the field after the second grating can then be written as

$$\tilde{u}(\nu,\mu,z_s+) = \left\{\left(\tilde{U}_o * \tilde{G}_1\right)T(z_s)\right\} * \tilde{G}_2 \quad , \tag{5.12}$$

in which the convolution theorem has been invoked twice (convolution is denoted here by an asterisk (*)).

The image plane of the optical system used for this research is not conjugate to a ground glass screen located immediately after the second grating, as is usually the case for moiré deflectometry. The ground glass screen is absent and the image plane is instead conjugate to the phase object positioned at z = 0. In order to calculate the image plane distribution it is necessary to determine the virtual field at the plane z = 0 that gives rise to the calculated field at $z = z_s+$ (eq. (5.12)). This virtual field, v(x,y,z=0), also represents the object field distribution in the plane of the detector. Thus, apart from a magnification factor and the effects of the finite pupil of the imaging optics,

$$\tilde{v}(\nu,\mu,\text{image}) \cong \left\{\left(\tilde{U}_o * \tilde{G}_1\right)T(z_s)\right\} * \tilde{G}_2 T(-z_s) \, . \tag{5.13}$$

Explicitly writing out the spectrum of the image plane field distribution:

$$\tilde{v}(\nu,\mu,\text{image}) \cong \sum_{n=-\infty}^{+\infty}\sum_{m=-\infty}^{+\infty} C_n C_m \tilde{U}_o\left(\upsilon - \frac{m+n}{p},\mu\right) exp\left[2\pi i\lambda m z_s\left(\frac{\upsilon}{p} - \frac{m^2}{2p^2}\right)\right], \tag{5.14}$$

where the term under the radical sign in eq. (5.11) has been approximated by the first two terms of its series expansion.

The inverse transform of eq. (5.14) is

$$v(x,y,\text{image}) \cong \sum_{n=-\infty}^{+\infty} \sum_{m=-\infty}^{+\infty} C_n C_m U_o\left(x + m\frac{\lambda z_s}{p}, y\right) \times$$
$$exp\left[2\pi i\left(\frac{m+n}{p}x + \frac{z_s\lambda}{2p^2}\left((m+n)^2 - n^2\right) - \frac{m\Psi}{p}\right)\right] , \qquad (5.15)$$

which can be interpreted as interferences between an infinite number of sheared versions of the object, multiplied by a phase factor. The shear distance for each object is a multiple of the distance Δ, where

$$\Delta \equiv \frac{\lambda z_s}{p} , \qquad (5.16)$$

which can be seen to be a paraxial expression of the grating equation. The complexity of the exponential phase factor in eq. (5.15) can be reduced by noting that if the distance z_s is chosen such that

$$z_s = z_T \equiv k\frac{p^2}{\lambda} , \text{ where } k = 1,2,3\ldots , \qquad (5.17)$$

then the portion of the field representing the gratings is the same as if the gratings were placed on top of each other without any separation between them. The distance z_T for $k = 1$ is known as the Talbot distance and the planes corresponding to multiples of z_T are known as Talbot planes. When k is equal to an odd integer, the fringe pattern undergoes a contrast reversal but otherwise is the same as the pattern with k equal to an even integer.

The contrast reversal of the field and the position of the discrete self-images of the grating at the Talbot planes can be easily seen with a microscope if the illumination

is monochromatic and collimated. As the focus of the objective is moved axially away from the grating successive self-images can be seen, including the contrast reversal on alternate images. For a Ronchi grating with a period of 25 μm illuminated with light of wavelength 500 nm the Talbot distance is 1.25 mm. The importance of the separation z_s being equal to z_T is emphasized by Kafri[9]. If the second grating is not located at a Talbot plane (a plane located at some multiple of the Talbot distance) of the first grating, the image is of low contrast and it is very difficult or impossible to discern any moiré fringes. An interesting method described by Patorski[10] involves a tilted first grating to reduce inter-order interference, but is limited in its effectiveness by the variation in Talbot distance and shear across the aperture of the deflectometer.

In traditional shearing interferometry only two wavefronts are present: $U_o(x,y)$, the original object field, and $U_o(x+\Delta,y)$, a duplicate of the wavefront, shifted spatially by an amount Δ. Equation (5.15) shows that in the image plane of the deflectometer there exist an infinity of sheared wavefronts, each identical to the original object field but shifted by an amount $m\Delta$, where $m=0,\pm1,\pm2,\pm3,\ldots$. In actuality, the image plane distribution is not quite so complicated. Several observations can be made that corroborate this assertion. The first observation is that for a Ronchi ruling consisting of alternating opaque and clear regions of equal width, the coefficients C_m are

$$C_m \equiv \left\{ \begin{array}{cc} \frac{2}{m\pi} sin\left(\frac{m\pi}{2}\right) & \text{m odd} \\ 0 & \text{m even} \end{array} \right\}, \qquad (5.18)$$

from which it can be seen that the coefficients rapidly decrease in amplitude as m increases, and that the even diffraction orders are nonexistent. The second observation is that the finite size of the entrance pupil of the imaging optics (or equivalently, their

finite spatial frequency response) limits the diffraction orders that pass unhindered through the system. The total effect of decreasing amplitude with increasing order along with filtering of the image is that the number of sheared images that make up the final image is greatly reduced from the infinity of images represented above.

In order to determine what effect the orders that do arrive at the image plane have on the image content and contrast it is necessary to examine the contribution made by each order, both separately and in concert. Once a determination has been made as to which orders are to be allowed to contribute to the image it is relatively simple to use a spatial filter to remove any unwanted orders.

5.2.2.2. Optical filtering to improve the image contrast

The usual moiré deflectometer configuration has a "real" image on a ground glass screen placed immediately after the second grating, which precludes any optical filtering. This limits the separation of the gratings[11] and ultimately, the sensitivity of the deflectometer. Investigations using the Talbot interferometer differ both in that the object is placed between the gratings and also in that most researchers do not impose the limitation of a ground glass screen after the second grating.

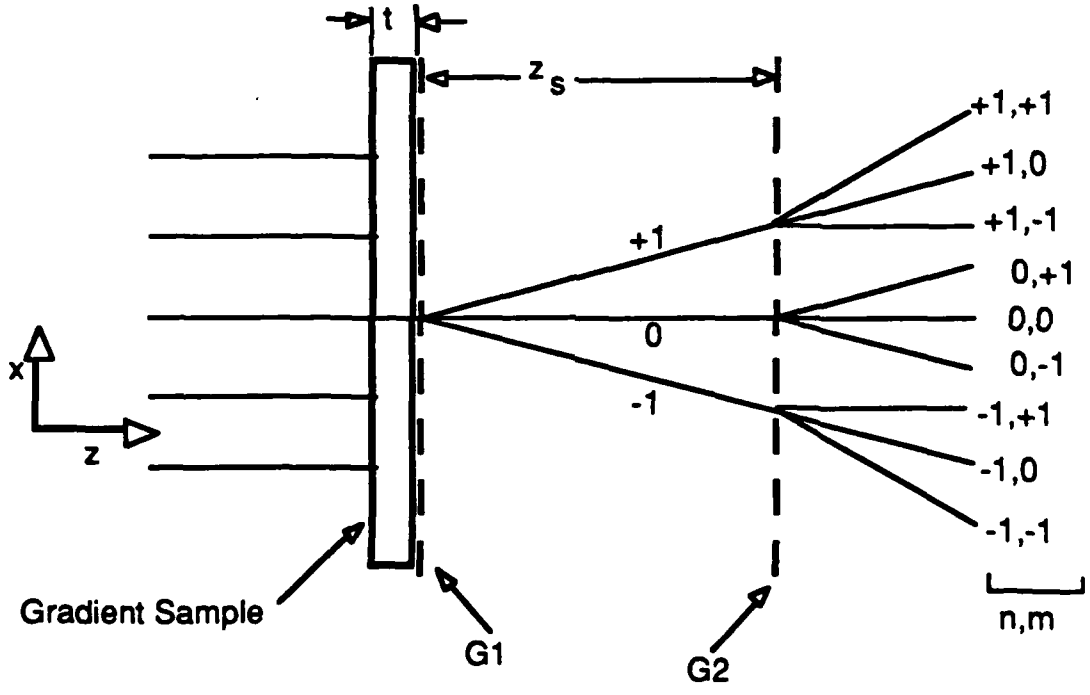

Figure 5.4
Cumulative effect of successive diffraction by the two gratings. A lens placed after the second grating can be used in conjunction with a spatial filter to select specific combinations of orders (the orders with the same sum n+m).

If some type of filtering operation takes place in the back focal plane of the imaging lens an even greater improvement in image quality can be made. D. Silva[12] has pointed out that the image contrast in Talbot interferometry can be improved by

optical filtering. What Silva does not state is that optical filtering can be used to remove the requirement that the grating separation be a multiple of the Talbot distance. This is a crucial point for multiple wavelength operation since the Talbot distance is linearly dependent upon the wavelength. Operation at different wavelengths requires changing the grating separation each time the wavelength is changed in order to preserve the image contrast. Changing the grating separation for each wavelength used changes the shear distance, Δ, and introduces another source of systematic error (to the extent that the grating separation is not exactly known). By optically filtering the output of the deflectometer, there is no longer a wavelength dependent contrast term in the detected intensity.

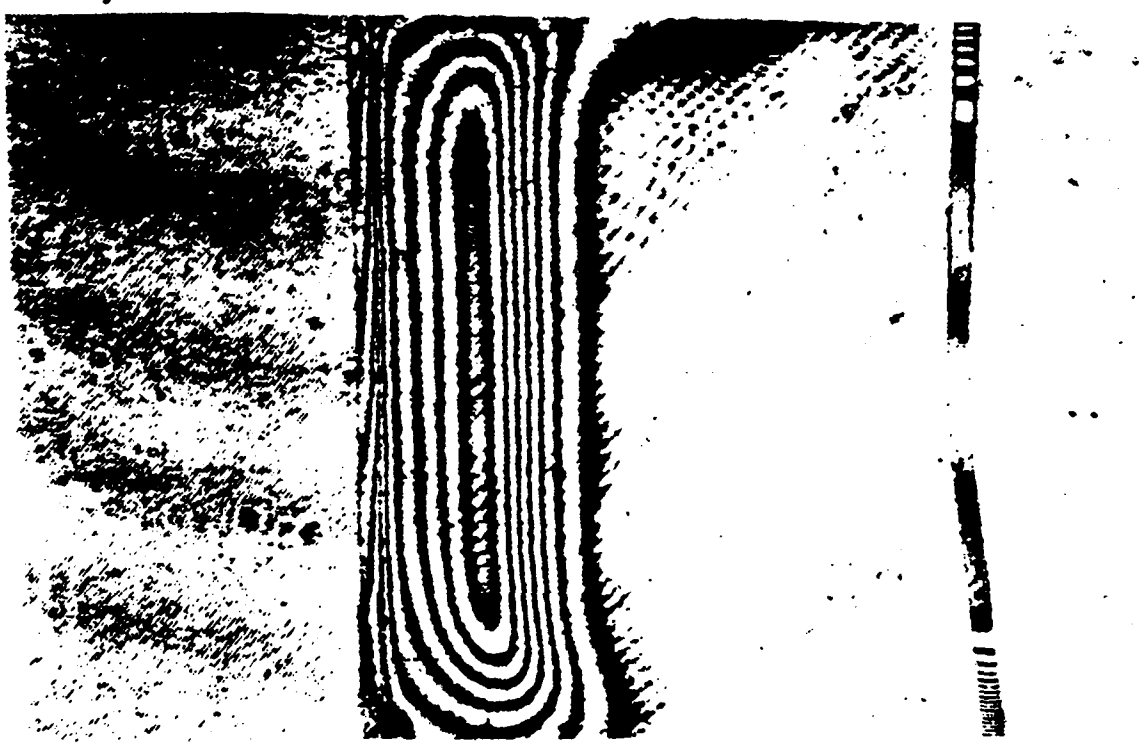

Figure 5.5
Photograph of filtered (+1) fringe pattern in the image plane of the deflectometer. Sample is DK85b, an ion-exchanged glass.

Other effects of selective filtering were also investigated by Silva, who used a spatial filter in the back focal plane of the imaging lens to allow only one order to pass on to the image. He showed that by filtering for specific orders the image can be interpreted as the first or second derivative of the index profile. This derivation is outlined in the next section and the importance of a time dependent phase shift, $\Psi = \Psi(t)$, is introduced.

5.2.2.3. Derivation of derivative relations for filtered images

If only the first order is allowed to pass on to the image it is equivalent to setting $n+m = \pm 1$ in eq. (5.15). Because only the odd diffraction orders exist, there are only four combinations of n and m such that $n+m = \pm 1$. These combinations are $n = 0$, $m = \pm 1$ and $n = \pm 1$, $m = 0$. The object is assumed to be a pure phase object that can be represented as

$$U_o(x,y) = exp\left(\frac{i2\pi}{\lambda} W(x,y)\right), \tag{5.19}$$

where $W(x,y)$ is the phase change experienced by light of wavelength λ in passing through the object. Using this expression while keeping only the terms $n+m = \pm 1$, gives an image intensity of

$$\left|v(x,y,0)\right|^2\Big|_{(n+m=\pm 1)} \equiv 2\left|C_0 C_1\right|^2\left[1+cos\left(\frac{2\pi}{\lambda}\left[W(x,y)-W(x\pm\Delta,y)\right]+\frac{2\pi}{p}\Psi\right)\right]. \tag{5.20}$$

Silva demonstrated that the filtering for the plus or minus first order as in eq. (5.20) yields approximately the first derivative of the object.

For the case $n+m = 0$ (zero order filtering) there are three combinations of n and m that contribute to the image: 1) $n = 0$, $m = 0$; 2) $n = 1$, $m = -1$; and 3) $n = -1$, $m = 1$. These three combinations give an image plane intensity of

$$\left|v(x,y,0)\right|^2\Big|_{(n+m=0)} \equiv \left|C_0{}^2\right|^2 + 2\left|C_1{}^2\right|^2 + 2C_0^2C_1^2\left\{cos\left(\frac{2\pi}{\lambda}[W(x,y)-W(x-\Delta,y)]+\frac{2\pi}{p}\Psi\right)+cos\left(\frac{2\pi}{\lambda}[W(x,y)-W(x+\Delta,y)]-\frac{2\pi}{p}\Psi\right)\right\} \quad (5.21)$$

Silva has shown that this zero order filtering leads to an intensity distribution that can be interpreted as the second derivative of the phase object (eq. (5.21)). This implies that if both the first and second derivatives of the phase object are non-zero the image could be very difficult to interpret for filtering allowing both zero and first orders to pass. One straight-forward solution is to filter for the first order alone. The intended use of the deflectometer at multiple wavelengths presents a problem in this case, however, because of the wavelength variation of the diffraction order position. Each time the wavelength is changed the position of the spatial filter would have to be changed. For this reason it is necessary to allow all three orders to pass.

Before determining how to overcome this limitation it is important to determine what form the field intensity takes in the image plane when all three orders, 0, +1, and -1 are allowed to pass. This is not the sum of the three intensities shown above but the sum of the three field amplitudes, in order to account for coherent interference. The intensity due to all three fields is

$$\left|v(x,y,0)\right|^2\Big|_{0,+1,-1} \equiv A + 2B\,cos\left(\frac{2\pi}{\lambda}\frac{2\Delta\partial W(x,y)}{\partial x}+\frac{4\pi\Psi}{p}\right) + 2C\,cos\left(\frac{2\pi}{\lambda}\frac{\Delta^2}{2}\frac{\partial^2 W(x,y)}{\partial x^2}\right)cos\left(\frac{2\pi}{\lambda}\frac{\Delta\partial W(x,y)}{\partial x}+\frac{2\pi\Psi}{p}\right) \quad (5.22)$$

where $W(x,y) \pm W(x \pm \Delta,y)$ has been expanded in a Taylor series and only the first two terms in the series have been retained. A, B, and C are functions of x that depend

on the grating period, the wavelength, and z_s, and have only high frequency terms with periods that are the same as the Ronchi grating. If the fringe pattern at the image is assumed to have only slowly varying spatial content relative to the grating period then A, B, and C can be assumed to be constant (the detector size can be chosen larger than the grating period but small enough to sufficiently sample the fringe pattern). Under these assumptions the fringe pattern consists of a constant term and two terms that depend on the first and second derivatives of the object's phase. A more elegant simplification can be made by making Ψ a function of time, say $\Psi = \Psi(t) = \omega t$. The first term of eq. (5.22) now oscillates with a temporal frequency of 2ω and the second term oscillates at the fundamental frequency ω. The two terms can be separated by electronically filtering the signal from a detector placed in the image plane. By examining the steps taken in deriving eq. (5.22) it can be seen that if the assumption that only the 0, -1, and +1 orders are present is removed then there is an infinity of terms present in the image field, oscillating at frequencies ω, 2ω, 3ω, etc. Electronic filtering can take the place of optical filtering by electronically isolating one component at a specific frequency[13]. The detected intensity, I_D, after filtering for the signal at frequency ω becomes

$$I_D \propto cos\left(\frac{2\pi}{\lambda}\frac{\Delta^2}{2}\frac{\partial^2 W(x,y)}{\partial x^2}\right)cos\left(\frac{2\pi}{p}(\Phi_D + \Psi(t))\right). \qquad (5.23)$$

The factor in front of the oscillating term has an argument that varies as a function of the second derivative of the object phase. While this does not affect the electronically measured phase, it does affect the contrast. If the second derivative is large the amplitude of the signal may go to zero. In this case the shear distance Δ can be changed to increase the signal level.

The detected phase is

$$\Phi_D = \frac{z_s}{p}\frac{\partial W(x,y)}{\partial x} . \qquad (5.24)$$

The component of the image intensity at frequency ω has a phase that is proportional to the derivative of the object phase and is independent of wavelength. This detected phase is identical in form to eq. (5.3) for the number of moiré fringes formed, if $W(x,y)$ is replaced by $t\, n(x,y,\lambda)$. This equation is an approximation in the sense that the terms of the Taylor series expansion of the index profile, beyond the first two terms, are assumed to be negligible, and the paraxial grating equation has been used (eq. (5.16)). In practice, these assumptions do not limit the accuracy of the deflectometer.

5.2.3. Source coherence considerations

Constraints on the source are mainly those of *spatial and temporal coherence* and are similar to constraints for other types of interferometry. If the source is resolvable by the collimating optics, the contrast across the pupil is reduced according to the Van Cittert-Zernike theorem[14]. The illumination must be coherent over a distance equal to or greater than the shear distance Δ for fringes to be visible. Using the pinhole size of 150 μm derived earlier from geometrical considerations (eq. (5.5)), and a collimating lens placed a distance of 300 mm away, the first zero of the coherence function for an incoherent source[15] is at approximately 1.2 mm, which was only twice the largest shear distance used in this research. For this reason the smaller pinhole size of 25 μm was used to insure adequate coherence over shear distances that were on the order of 1mm.

The temporal coherence required is such that the equivalent coherence length is less than the optical path length difference experienced by the fields passing through

two points on the sample separated by the shear distance. For a Hg arc lamp with a bandwidth $\delta\lambda$, the coherence length is $\delta l = \frac{\lambda^2}{\delta\lambda}$. For a filtered lamp with a bandwidth of $\delta\lambda$ = 10 nm at a wavelength of 315 nm, δl = 0.01 mm. For a sample with a thickness of 1 mm this result implies that an index change of 0.01 over the shear distance would be at the limit of the coherence length. Index changes of this magnitude are often fabricated[16], thus the shear, Δ, would have be reduced to accommodate steep index profiles.

5.3. Comparison of moiré deflectometry with shearing interferometry

5.3.1. Advantages

There are many advantages of using the moiré deflectometer over conventional interferometric measurement of the index of refraction. The first two major advantages are the ease in alignment of the components in the deflectometer and their low cost. The second advantage is the option of using a low coherence source such as an arc lamp in conjunction with narrow band filters to select the desired wavelength, in place of a larger and more expensive laser. The third advantage is that the fringe pattern is independent of wavelength. The fourth major advantage is that when a phase modulation method is used to recover the phase of the fringe pattern the phase can be modulated by moving one of the gratings. In addition, this modulation is independent of the illumination wavelength.

5.3.2. Disadvantages

The main disadvantages of moiré deflectometry are twofold. The first drawback is that deflectometry carries the same disadvantages as those of shearing interferometry, namely, reduced spatial accuracy and fewer fringes present in the fringe

pattern. The number of fringes present is shown in Chapter 6 to ultimately limit the accuracy of the determination of the index profile;

The second disadvantage is the possible decrease in sensitivity relative to shearing interferometry due to the longer "wavelength" used in deflectometry. The decrease in sensitivity is a function of the grating separation and the grating period. Trade offs can be made, however, between increased spatial accuracy and increased sensitivity by varying these two parameters.

5.4. Harmonic Phase Retrieval

In order to increase the accuracy with which phase data can be retrieved from any interference pattern, it is necessary to use some type of automated fringe detection scheme giving precise phase information. There are many schemes reported in the literature, the most common are the family of N-bucket techniques[17],[18] and variations on the heterodyne method[19]. Each has been applied most often to conventional interferometry and involves shifting the phase of a reference beam in a controlled manner and then interfering this beam with a test beam containing the wavefront to be measured. In the N-bucket techniques the phase of the reference beam (or equivalently, the fringe pattern) is stepped N times in equal increments of $2\pi/N$. After each step the intensity I_n is measured. The optical phase, θ, is extracted from the data through the following relation[20]:

$$\tan(\theta) = \frac{\sum_{n=1}^{N}\left[I_n \sin\left(\frac{n2\pi}{N}\right)\right]}{\sum_{n=1}^{N}\left[I_n \cos\left(\frac{n2\pi}{N}\right)\right]} \tag{5.25}$$

This method is accurate, typically on the order of $\frac{\lambda}{100}$, and lends itself well to 2-D calculations using data gathered in parallel with a CCD array and stored by a frame grabber. The main disadvantage of this technique is that the modulation amplitude must be at least $\frac{(N-1)}{N}\lambda$, where N is greater than 2. For a 25 μm pitch grating with N=3 this amplitude is greater than 17 μm, leading to problems in PZT performance (greater hysteresis errors and larger current drawn from the driving electronics).

The heterodyne method with two beam interference involves a constant shift in the frequency of the "test" beam relative to the reference beam. A stationary detector

placed in the fringe pattern then "sees" a sinusoidal modulation in time with a frequency equal to the optical beat frequency between the reference and test beams. The phase of the electrical signal from the detector is shifted in phase by an amount equal to the phase of the fringe pattern (plus some constant). A one dimensional profile of the sample phase can then be easily gathered by scanning the detector across the fringe pattern and recording the phase of the detected signal as a function of position using a standard phase meter or a phase sensing lock-in amplifier. Methods for shifting the frequency include Zeeman-splitting[21] and doppler shifting from a moving grating[22].

Methods of this second type, involving scanning a "point " detector across the image of the sample have been most useful for the measurement of gradient-index samples in the past. This is because the maximum measurable fringe density is not limited by the density of pixels in the detector (in for example, a CCD array) but instead by the scanning optics (by way of their magnification and resolution). While it is not expected that fringe densities are high in the deflectometer, there are other advantages in using a point scanning system. The primary advantage of point scanning is that if the detector is placed on the optical axis and the object itself is translated, there are no errors introduced due to lateral color aberration in the imaging optics. For these reasons a quasi-heterodyne method has been chosen to aid in accurate phase detection.

Translating the reference grating at a constant velocity gives a shift in frequency to the diffracted orders of:

$$\Delta\nu = \frac{mV}{p}, \tag{5.26}$$

where m is the diffraction order and V is the velocity of the grating. Unfortunately, in using this method, one would soon run out of grating unless it were very long! One scheme to overcome this limitation is to move the grating forwards and backwards at a

constant speed in a sawtooth type motion. Data would then be taken only during one direction of travel. Stricker[23] has implemented this type of detection using an electro-mechanical shaker on the second grating of a moiré deflectometer. Unfortunately, his method suffers due to nonlinearities in the motion of the grating. Discontinuous movement of this type is much more difficult to maintain than sinusoidal motion, especially at higher frequencies with large amplitude motion.

5.4.1. Harmonic modulation

A quasi-heterodyne method was discovered and analyzed by J. Miceli[24] . Miceli's method, which he termed harmonic modulation consists of modulating the phase of the reference beam at a fundamental frequency plus its first harmonic so that the phase modulation Ψ is:

$$\Psi(t) = A\,sin(\omega t) + B\,sin(2\omega t + \alpha) \tag{5.27}$$

Miceli has derived the relationships between A,B, and α, in order that the detected signal's phase (at the fundamental frequency, ω) is equal to the (optical) phase of the fringe pattern. There exists a continuum of solutions which includes amplitudes for A and B that are less than $\frac{\pi}{4}$, giving a total modulation amplitude of less than $\frac{\pi}{2}$, which makes it very attractive for systems where the "wavelength" is relatively large as in the deflectometer. It was decided that this type of quasi-heterodyne detection was ideally suited for the moiré deflectometer where the period of the gratings used is 25 μm and a reduction in the distance required to move the grating reduces systematic positional errors.

The derivation given by Miceli is quite long, as he analyzes the general case $A\,sin(n\omega t) + B\,sin(m\omega t + \alpha)$, for all integers n and m. The effect on the linearity of the relationship between the electrical phase and the optical phase of α is not discussed by

Miceli except as an experimentally determined parameter. Although his theoretical treatment does include α, the functional form α takes does not lend itself to easy analysis. In order to more fully understand the effects of variations in A, B, and α on the system linearity and, through them, the effects of non-ideal grating motion, it is necessary to rederive the harmonic interferometry equations into a form which lends itself to a more straightforward analysis.

5.4.2. Derivation of phase retrieval via harmonic modulation

This derivation is very general in nature and is applicable to any two beam interference in which the phase of one beam can be modulated. The derivation starts with the two beam interference equation and isolates components at the fundamental frequency. This derivation assumes that eq. (5.22) for the detected signal can be equivalently represented by (where the two beams are assumed to be of equal intensity and are normalized to one half):

$$I = \frac{1}{2}\left[1 + cos\left[\theta(x,y) + \Psi(t)\right]\right] \tag{5.28}$$

where $\Psi(t) = A sin(\omega t) + B sin(2\omega t+\alpha)$ and $\theta(x,y) = \frac{2\pi z_s}{p} W(x,y)$ (z_s is the grating separation, p is the grating pitch, and $W(x,y)$ is the phase change in traversing the sample). Factors affecting the contrast of the fringe pattern have been left out. The easiest method of simplifying this equation is to realize that the expansion of $cos(\Psi(t))$ consists of products of $sin(n\omega t)$ and $sin(m\omega t)$. These products consist of components that oscillate at frequencies $(n+m)\omega$ and $(n-m)\omega$. All terms that involve products where $|n-m| \neq 1$ can be dropped (i.e. drop products with either n and m odd or n and m even) since they are electronically filtered out.

The following identities are useful:

$$cos(A\,sin(\omega t)) = J_0(A) + 2\sum_{n=1}^{\infty} J_{2n}(A)cos((2n)\omega t) \quad , \qquad (5.28\ a)$$

and

$$sin(B\,sin(\omega t)) = 2\sum_{n=1}^{\infty} J_{2n-1}(B)sin((2n-1)\omega t) \quad . \qquad (5.28\ b)$$

Explicitly writing out $\Psi(t)$, the detected signal (eq. (5.28)):

$$I = \frac{1}{2}\left\{1 + cos\left\{A\,sin(\omega t) + B\,sin(2\omega t + \alpha) + \theta(x,y)\right\}\right\} . \qquad (5.29)$$

Expanding this equation gives

$$\begin{aligned} I = {} & cos(A\,sin(\omega t))cos(B\,sin(2\omega t + \alpha) + \theta) \\ & - sin(A\,sin(\omega t))sin(B\,sin(2\omega t + \alpha) + \theta) \ . \end{aligned} \qquad (5.30)$$

The second factor of the first term of eq. (5.30) can be further expanded using

$$\begin{aligned} cos(B\,sin(2\omega t + \alpha) + \theta) = {} & cos(B\,sin(2\omega t + \alpha))cos(\theta) \\ & - sin(B\,sin(2\omega t + \alpha))sin(\theta) \quad . \end{aligned} \qquad (5.31)$$

By examining eq. (5.31) in conjunction with the identities (5.28 a) and (5.28 b) it can be seen that the frequency content of the first line of eq. (5.30) is all either d.c. or higher harmonics of ω and thus are filtered out. This leaves the second line of eq. (5.30), so that after dropping constants of proportionality and d.c. terms the detected signal becomes:

$$I = -sin(A\,sin(\omega t))sin(B\,sin(2\omega t + \alpha) + \theta) \ . \qquad (5.32)$$

Using identities (5.28 a) and (5.28 b) again gives:

$$I = -2\left(\sum_{n=1}^{\infty} J_{2n-1}(A)\sin((2n-1)\omega t)\right)\times$$
$$\left(\cos(\theta)\left\{2\sum_{m=1}^{\infty} J_{2m-1}(B)\sin((2m-1)(2\omega t+\alpha))\right\}\right.$$
$$\left.+\sin(\theta)\left\{J_0(B)+2\sum_{m=1}^{\infty} J_{2m}(B)\cos(2m(2\omega t+\alpha))\right\}\right). \qquad (5.33)$$

To retain only those components of frequency ω in the product of the first term with the second term is equivalent to requiring that $|2n-1 - 2(2m-1)| = 1$. This implies either

$$\underline{n = 2m} \text{ or } \underline{n = 2m-1}$$

In the same way, retaining components at ω in the product of the first term with the third term means that $|2n-1 - 4m| = 1$, implying either

$$\underline{n = 2m} \text{ or } \underline{n = 2m+1}$$

Keeping only these components and making the appropriate changes in indices:

$$I = -2\cos(\theta)\left(\left\{\sum_{m=1}^{\infty} J_{4m-1}(A)J_{2m-1}(B)\cos(\omega t-(2m-1)\alpha)\right\}\right.$$
$$\left.+\left\{\sum_{m=1}^{\infty} J_{4m-3}(A)J_{2m-1}(B)\cos(\omega t+(2m-1)\alpha)\right\}\right)$$
$$+2\sin(\theta)\left(\left\{\sum_{m=1}^{\infty} J_{4m-1}(A)J_{2m}(B)\sin(\omega t+2m\alpha)\right\}\right.$$
$$\left.+\left\{\sum_{m=1}^{\infty} J_{4m+1}(A)J_{2m}(B)\sin(\omega t-2m\alpha)\right\}\right)$$
$$-2\sin(\theta)J_1(A)J_0(B)\sin(\omega t) \qquad (5.34)$$

It is not immediately obvious what the relationship is between the phase of the detected signal from the way the signal is represented above and the optical phase, θ. Further expansion of eq. (5.34) and then rearranging yields an expression for the filtered signal that can be written as:

$$I = X\cos(\omega t) + Y\sin(\omega t)\ , \tag{5.35}$$

where

$$\begin{aligned} X &= -2D\cos(\theta) + 2E\sin(\theta) \\ Y &= -2F\cos(\theta) + 2G\sin(\theta)\ , \end{aligned} \tag{5.36}$$

and the coefficients D, E, F, and G are

$$\begin{aligned} D &= \left\{ \sum_{m=1}^{\infty} J_{2m-1}(B)\left[J_{4m-1}(A) + J_{4m-3}(A)\right]\cos((2m-1)\alpha) \right\} \\ E &= \left\{ \sum_{m=1}^{\infty} J_{2m}(B)\left[J_{4m-1}(A) + J_{4m+1}(A)\right]\sin(2m\alpha) \right\} \\ F &= \left\{ \sum_{m=1}^{\infty} J_{2m-1}(B)\left[J_{4m-1}(A) - J_{4m-3}(A)\right]\sin((2m-1)\alpha) \right\} \\ G &= \left\{ \sum_{m=1}^{\infty} J_{2m}(B)\left[J_{4m+1}(A) - J_{4m-1}(A)\right]\cos(2m\alpha) \right\} - J_1(A)J_0(B) \end{aligned}\ . \tag{5.37}$$

The filtered detected signal is in the form:

$$I_D = K\cos(\omega t + \theta_D). \tag{5.38}$$

Equating eqs. (5.35) and (5.38) it is easily shown that

$$K = \left(X^2 + Y^2\right)^{\frac{1}{2}} \tag{5.39}$$

and

$$\theta_D = \tan^{-1}\left(-\frac{Y}{X}\right) = \tan^{-1}\left(\frac{-F\cos(\theta) + G\sin(\theta)}{D\cos(\theta) - E\sin(\theta)}\right). \tag{5.40}$$

The requirement for linearity between the detected phase and the optical phase can be stated as

$$\theta_D = \pm\theta + \delta\ , \tag{5.41}$$

where δ is some arbitrary phase shift.

Rewriting eq. (5.40) as

$$tan(\pm\theta+\delta)=\frac{\Omega sin(\theta+\eta)}{\Pi cos(\theta+\zeta)} \tag{5.42}$$

where

$$\Omega^2 = F^2 + G^2 \ , \tag{5.43}$$

$$\Pi^2 = E^2 + D^2 \ , \tag{5.44}$$

$$tan(\zeta)=\frac{E}{D} \ , \quad \text{and} \tag{5.45}$$

$$tan(\eta)=\frac{F}{G} \ . \tag{5.46}$$

Furthermore, the requirement of linearity forces $\Omega = \Pi$. Examining eqs. (5.40-5.44) in light of this, it can be seen that one obvious solution for the positive branch is to require that $D = \pm G$, $E = F = 0$ and $\delta = \zeta = \eta = 0$. This is the solution choosen by Miceli and is the one examined here. The equation $D = G$ can be used to derive the requirements on the amplitudes A and B for linearity. The existence of other solutions is not investigated here but their existence is investigation to carry out in order to determine if there are smaller amplitude solutions for A and B than those discussed here.

The condition that $E = F = 0$ can be very simply met by requiring that

$$\alpha = \kappa\pi \qquad \kappa = 0,1,\ldots \ . \tag{5.47}$$

(Note that if $\alpha = \kappa\frac{\pi}{2}$, where $\kappa = 1, 3, \ldots$ then $X = 0$ and the linearity requirement, eq. (5.41), cannot be met.) The condition $D = \pm G$ implies that:

$$\sum_{m=1}^{\infty} J_{2m-1}(B)\left[J_{4m-1}(A)+J_{4m-3}(A)\right](-1)^{(2m-1)\kappa}$$

$$\pm\left\{\sum_{m=1}^{\infty}\left[J_{2m}(B)\left[J_{4m+1}(A)-J_{4m-1}(A)\right]\right]+J_1(A)J_0(B)\right\}=0 \quad , \qquad (5.48)$$

which gives the conditions on A and B under which the detected signal's phase and the absolute value of the optical phase are identical.

Because of the way in which Bessel functions decrease in amplitude with increasing order and the nature of the summations in eq. (5.48) it is sufficient to examine only the first term in each summation (m=1). (Examination of the magnitude of the first few terms and later actual experimental use of the solutions found using only the first term have verified the correctness of this approximation.) Using only the terms corresponding to m = 1 eq. (5.48) becomes

$$J_1(B)\left[J_3(A)+J_1(A)\right]$$

$$\pm\left\{J_2(B)\left[J_5(A)-J_3(A)\right]+J_1(A)J_0(B)\right\}=0 \quad . \qquad (5.49)$$

The linearity requirement must now be expressed as

$$\theta_D=\pm(-1)^{\kappa}\theta \quad . \qquad (5.50)$$

Plotting the two equations corresponding to the positive and negative branches of the left side of eq. (5.49) graphically indicates the position of linear solutions as zero crossings. Figure 5.6 shows these two plots as a function of B for an arbitrarily chosen value of 1 rad. for A.

Once the amplitudes for A and B are chosen so that linearity is obtained, there are two values of κ that are interesting: $\kappa = 0$ or 1, corresponding to $\alpha = 0$ or π, respectively. In order to have $\theta = +\theta_D$ either the positive branch with $\kappa = 0$ (equivalently, $\alpha = 0$) can be used, or the negative branch with $\kappa = 1$ ($\alpha = \pi$) can be used. It is advantageous to use the solution with the smallest amplitudes for A and B

because limiting the distance the grating moves decreases systematic errors due to non-ideal behavior of the device used to move the grating. From the graph in 5.5 it can be

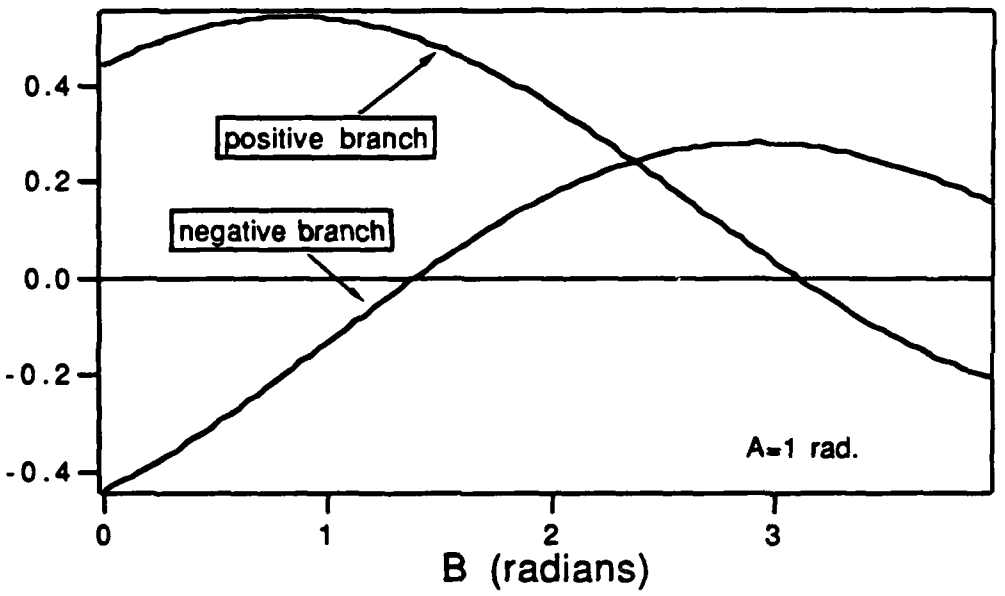

Figure 5.6
Graph of eq. (1.1) for m=1 and A=1 rad. Linear solutions correspond to the zero crossings of the two branches.

seen that linear solutions for the negative branch occur for smaller values of A and B. Thus choosing solutions corresponding to the negative branch and $\alpha = \pi$ gives the required linearity and smaller amplitude motion of the grating.

Finding the first zeros of the negative branch of eq. (5.49) as a two-dimensional function of A and B lends itself easily to numerical techniques on a microcomputer. A plot of the values of B that give linear solutions as a function of A for the negative branch are shown in figure 5.7.

Given the condition of linearity, it is interesting to note that the amplitude of the detected signal at frequency ω is

$$K = \left(D^2 + G^2\right)^{\frac{1}{2}}, \tag{5.51}$$

which is independent of both optical phase and time. This is an important point since a direct check of the linearity of the system is to vary the optical phase and determine whether or not the amplitude of the detected signal changes. This form for

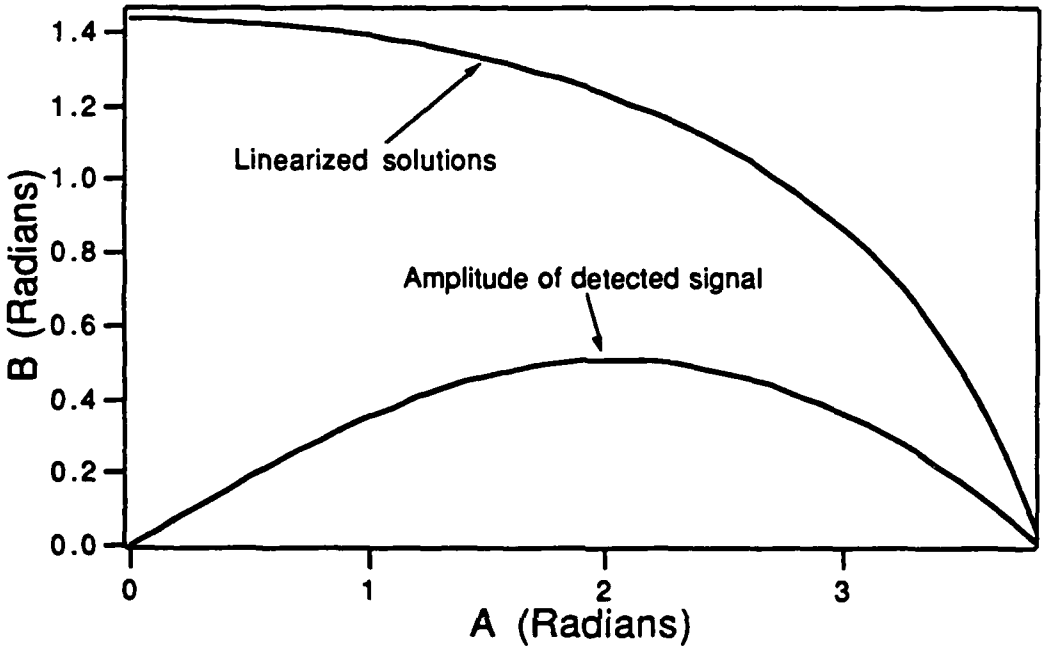

Figure 5.7
Graph of values of A and B giving linearized solutions to eq. (5.49) (After Miceli).

the amplitude neglects the contrast limiting factor derived in eq. (5.23) which depends on the second derivative of the wavefront.

One advantage of the derivation presented here is that it is in a form which allows the effects of non-ideal phase modulations to be examined in some detail. This analysis is necessary in order to understand what effects non-ideal system behavior or alignment have on the linearity of the detected phase.

Figure 5.8 shows plots of the detected phase versus the optical phase (or phase of the fringe pattern at the output of the deflectometer) for three different states of the modulating signal. The first plot shows a linear relationship between the detected phase and the optical phase. The second and third plots show the effects of an amplitude

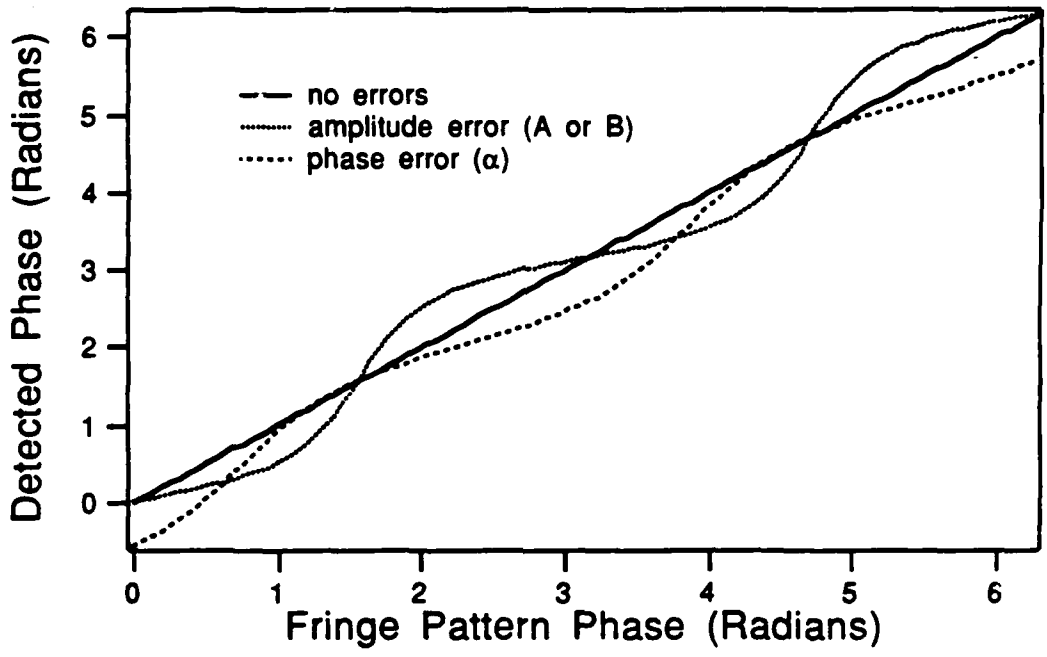

Figure 5.8
Effect of errors in the modulating signal's phase and amplitude on the linearity of the detected phase.

error of approximately $\frac{\lambda}{15}$ and a phase error of $\frac{\pi}{5}$, respectively. These plots are generated using eq. (5.40), which gives the relationship between the detected phase and the optical phase. Because the index change is proportional to the integral of the detected phase, the calculated index profile has periodic errors if either the amplitude (A or B) of the phase modulation is incorrect, or α is incorrect. The error in the index of refraction follows the phase error, being periodic and $\pi/2$ out of phase with the detected phase error. Neither of these types of errors is acceptable for precise determination of the index profile although their effects are mitigated for measurements over many periods.

5.4.3. *Effects of non-ideal modulation on linearity*

Miceli has demonstrated experimentally the errors introduced when α is not either 0 or π or when A or B are not set at the values which give linearity between the detected signal and the optical phase, showing results similar to those in fig. 5.8. He has also demonstrated the shift from positive linearity to negative linearity when α is changed from 0 to π , as predicted by eq. (5.50). It is interesting, however, to examine the tolerances on α if the values of A and B are used as compensating parameters.

Although the form for the detected phase (eq. (5.40)) is simple, it is not clear what effects changes in the amplitudes of the components of the driving signal from their ideal amplitudes have on the detected phase. An examination of the effects small changes of A, B, and α have on the detected signal suggests that the error in the detected signal ε_D, defined as

$$\varepsilon_D = \theta_D - \theta \quad , \tag{5.52}$$

can be written as

$$\varepsilon_D = \gamma + \beta sin(2\theta) + \xi cos(2\theta) \quad . \tag{5.53}$$

This can be seen by examining fig. 5.8. To prove that this is, in fact, an accurate expression for the error, the right hand side of eq. (5.40) for θ_D can be equated to ε_D + θ. Taking the tangent of both sides and cross multiplying while assuming that γ, β, and ξ are small yields

$$\begin{aligned} &[-F + G\,tan(\theta)][1 - tan(\theta)(\gamma + \beta sin(2\theta) + \xi cos(2\theta))] \\ &= [D - E\,tan(\theta)][tan(\theta) + \gamma + \beta sin(2\theta) + \xi cos(2\theta)] \quad , \end{aligned} \tag{5.54}$$

where D, E, F, and G are defined in eqs. (5.37). Expanding this and equating factors of $cos(\theta)$, $sin(2\theta)$, etc. gives

$$\xi = \frac{2(D+G)\left[(E-F)(D-G)+(E+F)(D+G)\right]-(E+F)\left[(D+G)^2+(E+F)^2\right]}{(D+G)\left[(D-G)^2+(E+F)^2-2(D+G)^3\right]}$$

$$\gamma = \frac{(E+F)+(G+D)\xi}{G-D}$$

$$\beta = \frac{(G-D)+(E+F)\gamma}{G+D} \quad . \tag{5.54}$$

These can be simplified somewhat by realizing that under certain conditions (E+F) may be small or (D+G) may be large, etc. Unfortunately, this type of simplification does not lead to a clearer understanding of the error, ε_D, or the interactions between A, B, and α. Figure 5.9 consists of contour plots of γ, β, and ξ as functions of α and B. (It is noted here that although each of γ, β, and ξ are functions of A, B, and α, it is sufficient for this analysis to assume that the functions D, E, F, and G take on all interesting values as B varies and A is held fixed.) It is evident from fig. 5.9 that β is essentially independent of variations in α while γ and ξ are independent of variations in B (or A). This is explicitly indicated by writing ε_D as

$$\varepsilon_D = \gamma(\alpha)+\beta(A,B)sin(2\theta)+\xi(\alpha)cos(2\theta) \; . \tag{5.55}$$

This means that errors in the phase of the driving signal for the grating modulation cannot be corrected through an adjustment of the amplitudes of the $sin(\omega t)$ or $sin(2\omega t)$ components and vice-versa. (On the more positive side, the rms error does not increase as the sum of γ, β, and ξ, but as the sum of γ and either β or ξ, which ever is greater, due to the orthogonality of $sin(2\theta)$ and $cos(2\theta)$.) This result has been experimentally verified on several dissimilar systems, all of which use the harmonic method of phase detection.

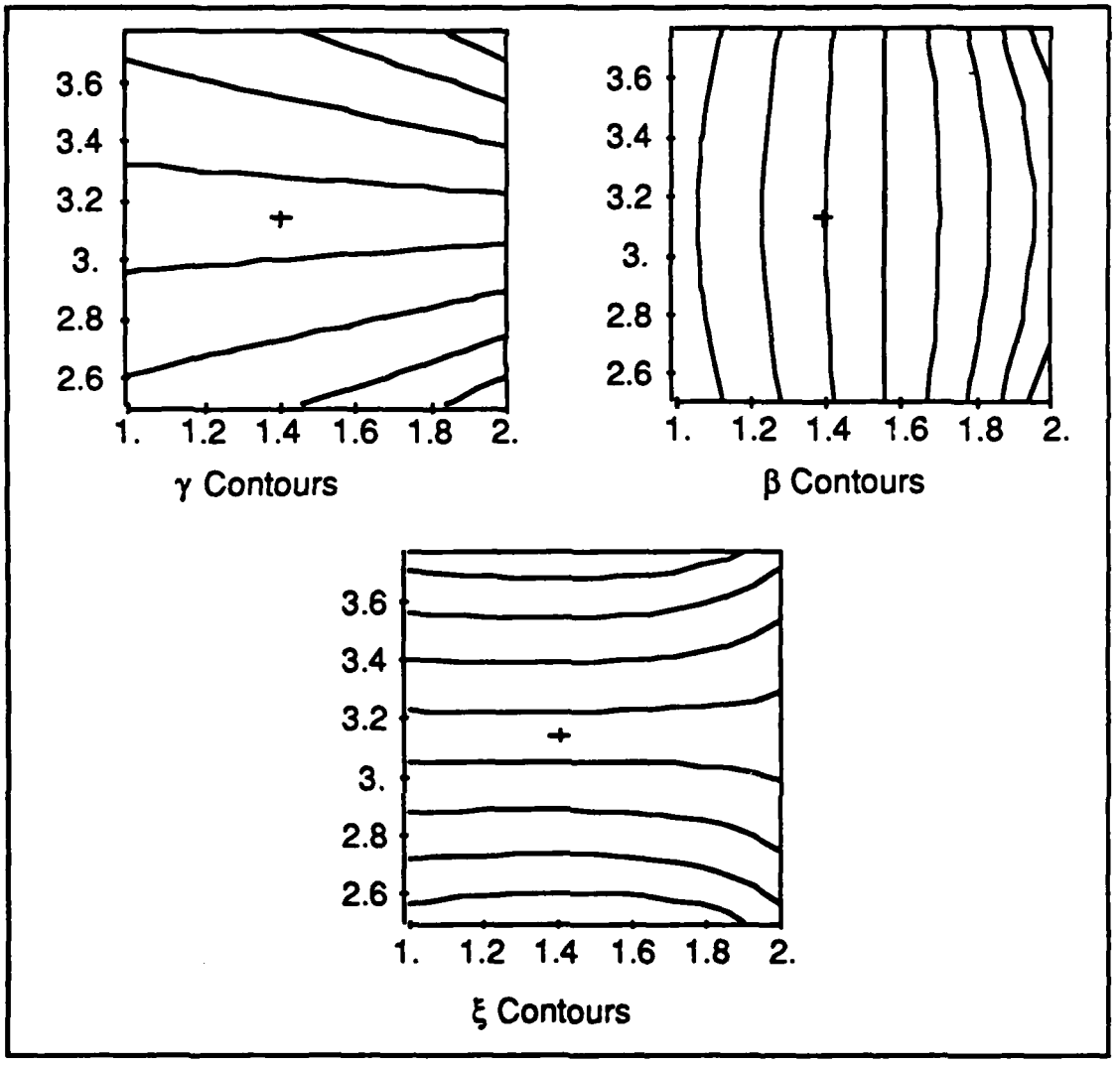

Figure 5.9

Plots demonstrating the relative independence of γ, β, and ξ from either α or B (A). For each contour plot the vertical axis is α and the horizontal axis is B (A). The small cross near the center of each plot represents the position of the linearized solution.

The above analysis and fig. 5.9 show that it is sufficient to examine the effects of errors in A and B separately from errors in α. Figure 5.10 shows the effect of errors in the amplitudes of A and B while α is held constant at its correct value (π, in this case). It is important to keep in mind that the derivation for the form of the error

assumes that the deviations from the correct values are small, so that the errors represented by contours far from the ideal values for A and B are certainly understated.

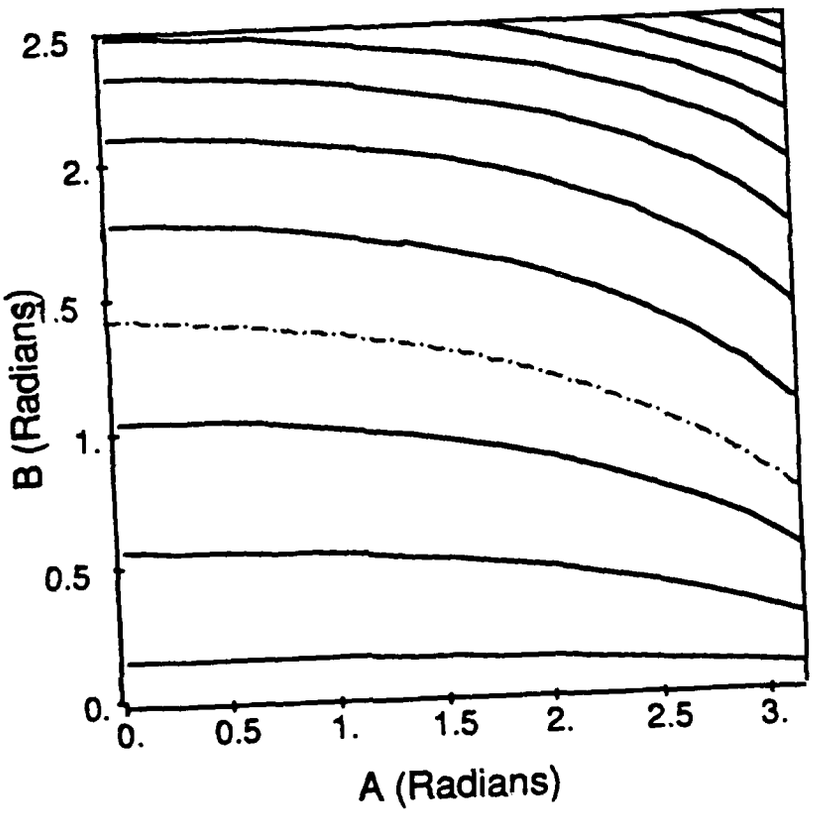

Figure 5.10

Plot showing error contours for β as a function of A and B with $\alpha = \pi$. Each contour line represents an error of 0.3 radians (1/20 of a fringe).

Figure 5.11 shows the magnitude of the errors induced when the phase, α, of the harmonic driving signal is in error.

The conclusion to be reached from the above analysis is that the harmonic modulation scheme for phase retrieval is relatively insensitive to small deviations in the driving waveform. However, the effects of these errors can be significant when there are few fringes and the desired quantity is recovered through an integration of the

phase. Furthermore, the errors due to deviations in A and B from their ideal values cannot be compensated for by an adjustment in α, and vice-versa.

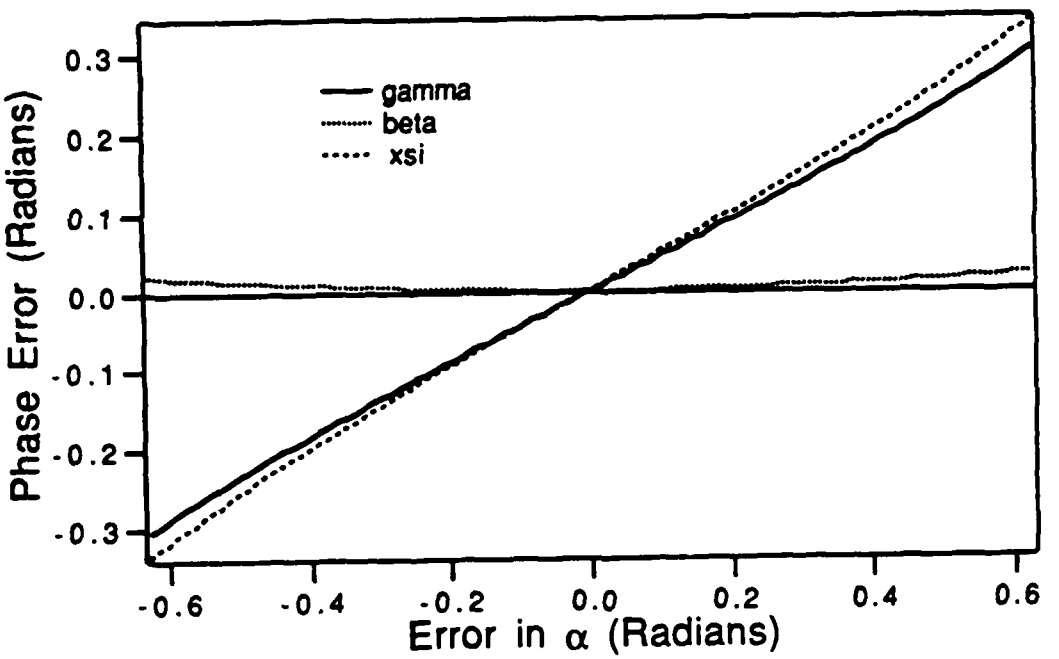

Figure 5.11

Plot of the error in the detected phase as a function of the error in α. (A=1 rad., B=1.39 rad.)

It can be seen from the above figures that there is a roughly linear variation of the error amplitude in the detected signal with either amplitude or phase errors in the modulation.

5.5. Summary

The use of a moiré deflectometer has been presented as an effective means for measuring the profiles of GRIN materials over a wide wavelength range.

The equations describing the intensity in the image plane have been derived and the advantages of optical filtering in conjunction with electronic filtering have been discussed.

The use of the harmonic phase modulation method has been shown to be applicable to the deflectometer with the added advantage of wavelength independent phase modulation.

The theory governing the harmonic phase retrieval method has been rederived and discussed with emphasis placed on the correction of errors introduced by non-ideal phase modulation.

References for Chapter 5.

[1]Y. Nishijima and G. Oster, "Moire Patterns: Their Application to Refractive Index and Refractive Index Gradient Measurements," JOSA **54** (1964) 1.

[2]F. Talbot, "Facts Relating to Optical Science. No. IV," Phil. Mag. **9** (1836) 401.

[3]Nishijima and Oster, op. cit.

[4]G. Oster, M. Wasserman, and C. Zwerling, "Theoretical Interpretation of Moire Patterns," JOSA **54** (1964) 169.

[5]O. Kafri, "Noncoherent method for mapping phase objects," Opt. Lett. **5** (1980) 555.

[6]L. Gregorka and D. T. Moore, "Chromatic Variation of Index of Refraction Gradients, Part 1," Appl. Opt. **19** (1980) 1096.

[7]*Optical Shop Testing*, D. Malacara (ed.), J. Wiley, New York (1978) 105.

[8]J.W. Goodman, *Introduction to Fourier Optics*, McGraw-Hill, New York (1968) 48.

[9]O. Kafri and I. Glatt, "Moiré Deflectometry: A Ray Deflection Approach to Optical Testing," *Opt. Eng.* **24** (1985) 944.

[10]K. Patorski, "Talbot Interferometry with Increased Shear: Further Considerations," Appl. Opt. **25** (1986) 1111.

[11]J. Stricker, "Diffraction Effects and Special Advantages in Electronic Heterodyne Moiré Deflectometry," App. Opt. **25** (1986) 895.

[12]D.E. Silva, "Talbot interferometer for Radial and Lateral Derivatives," App. Opt. **11** (1972) 2613.

[13]C. Koliopoulos, "Radial grating Lateral Shear Heterodyne Interferometer," App. Opt. **19** (1980) 1523.

[14]M. Born and E. Wolf, *Principles of Optics*, sixth ed.,Pergamon, New York (1983) 508.

[15]Reynolds, DeVelis, Parrent, Thompson, *The New Physical Optics Notebook: Tutorials in Fourier Optics*, SPIE Optical Engineering Press, Bellingham, WA (1989) 83.

[16]S. N. Houde-Walter, *Gradient-Index Profile Control by Ion Exchange in Glass*, Ph.D. thesis, University of Rochester, 1987.

[17]J. H. Bruning, D. R. Herriot, J. E. Gallagher, D. P. Rosenfeld, A. D. White, and D. J. Brangaccio, "Digital Wavefront Measuring Interferometer for Testing Optical Surfaces and Lenses," Appl. Opt. **13** (1974) 2693.

[18]J. C. Wyant, "Use of an ac heterodyne lateral shear interferometer with real-time wavefront correction systems," Appl Opt. **14** (1975) 2622.

[19]P. Harihan, "Quasi-heterodyne Hologram Interferometry," Opt. Eng. **24** (1985) 632.

[20]Ibid.

[21]L. Yao, Z. Zhiyao, and W. Runwen, "Optical Heterodyne Measurement of the Phase Retardation of a Quarter-Wave Plate," Opt. Lett. **13** (1988) 533.

[22]W. Stevenson, "Optical Frequency Shifting by means of a Rotating Diffraction Grating," App. Opt. **9** (1970) 649.

[23]J. Striker, "Electronic Heterodyne readout of Fringes in Moiré Deflectometry," Opt. Lett. **10** (1985) 247.

[24]J. J. Miceli, Infrared Gradient-Index Optics: Materials, Fabrication, and Testing, Ph.D. thesis, University of Rochester, 1982.

CHAPTER 6

Results of Measurements using the Moiré Deflectometer

6.1. Introduction

This chapter describes the experimental apparatus making up the moiré deflectometer and the measurements that have been made with it. The complete deflectometer can be divided into two subdivisions, one consisting of the optical apparatus (including the source) and one consisting of the electrical apparatus (including the detectors and the computer). The considerations made during the design of the deflectometer are presented along with detailed directions for the alignment and operation of the instrument.

Discussions in the literature of moiré deflectometry are seldom concerned with the type of illuminating source used. The widespread use of lasers as sources has removed most concerns in interferometry about source temporal coherence (wavelength bandwidth) and spatial coherence. On the other hand, the use of a laser generally limits the user to a few wavelengths, unless more than one type of laser is used. The broad coherence tolerance of the moiré deflectometer allows the use of a filtered incoherent source, in this case a mercury arc lamp. The mercury arc is attractive because it can provide illumination at many different wavelengths (approximately 7 spectral peaks in the visible and uv) and because the narrowness of the peaks reduces wavelength uncertainty errors in the calculation of the index dispersion.

The use of a broadband source put severe constraints on the type of optics available for collimation and imaging. Finding achromatic lenses for such a wide wavelength band was not possible. A lack of achromatism in the imaging optics would have led to lateral chromatic aberration in the image. This variation in magnification

with wavelength was not acceptable for the measurement of wavelength dependent data, hence the use in this work of all reflecting optics. The only exceptions to the use of reflecting optics were the gratings themselves, which were fabricated on uv grade fused silica blanks and the condenser optics for the arc lamp, which were also fused silica.

The implementation of a sample scanning stage is presented and the advantages over other methods of scanning the image are discussed. The most important of these advantages are the ability to use the imaging optics on-axis and the freedom from position dependent noise across the object field. One example of position dependent noise is non-uniformities in phase across the field caused by imperfections in the gratings or by aberrations introduced by the collimating optics.

The final sections of this chapter are devoted to discussing the data from the deflectometer and the various sources of error present in gathering and reducing the data. The effect of some of these errors on the calculated index of refraction is quite significant. It is interesting to note that most random temporal noise did not adversely affect the result. The largest sources of errors came from systematic errors during the reduction of the data. The accuracy and precision of the deflectometer are discussed and the results of measurements are presented and compared with measurements made using an a.c. Mach-Zehnder interferometer.

The achromatic operation of the deflectometer and the accuracy to which index profiles can be measured suggests that measuring the dispersion of GRIN materials may be possible. Several measurements have been carried out on both GRIN ion-diffused glass and GRIN fluoride crystals and are presented at the end of the chapter.

6.2. Deflectometer Apparatus

Figure 6.1 shows a schematic of the complete deflectometer with the division of the apparatus into two separate groups, optics and electronics, outlined. Apart from the modifications necessary for achromatic operation, the deflectometer optics are not fundamentally different from those of the Talbot interferometers reported in the literature.

6.2.1. Source and collimating optics

The source was a 100 W mercury arc lamp in an ORIEL lamp housing, model 66007. This arc (Osram HBO 100W/2) is the brightest Hg arc source available in the under 1000 W range. The arc brightness is 1700 CD/mm^2 and has a diameter of approximately 0.25 mm. The arc is collimated using an F/1.0 fused silica lens (F = 35 mm) and then is focused onto a 25 μm pinhole with another F/1.0 fused silica lens (F = 50 mm) for a total magnification of approximately 1.4.

The illumination from the pinhole is reflected onto a concave collimating mirror (F = 300 mm) positioned at the same height as the gratings but lower than the pinhole. The effect of this off-axis arrangement is to introduce a significant amount of astigmatism and coma (among other aberrations) in the image. Because the arrangement is off-axis in one plane, the effect of the aberrations is made negligible by orienting the gratings so that their planes are perpendicular to both the optical axis and the plane on which the projection of the mirror and arc are symmetrical. (See fig. 6.2.) Thus the only aberration in the x direction, the direction in which measurements are made, is the spherical aberration and defocus due to the collimating mirror.

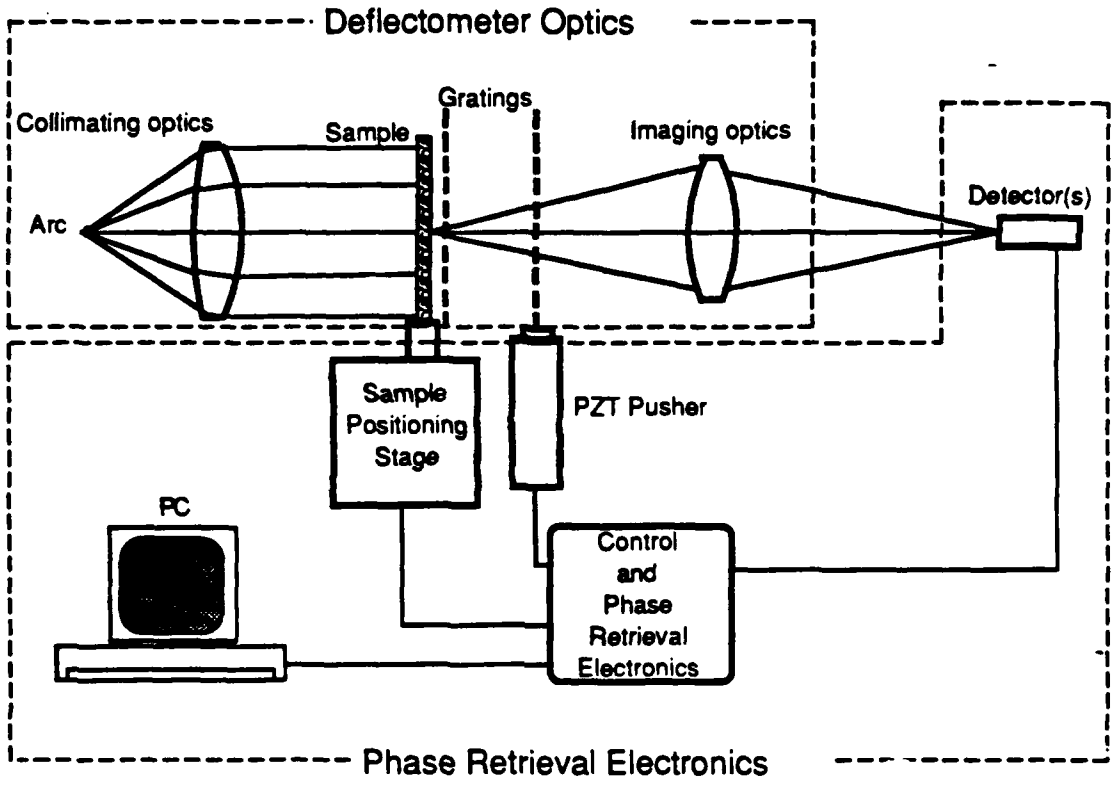

Figure 6.1
Schematic of the moiré deflectometer.

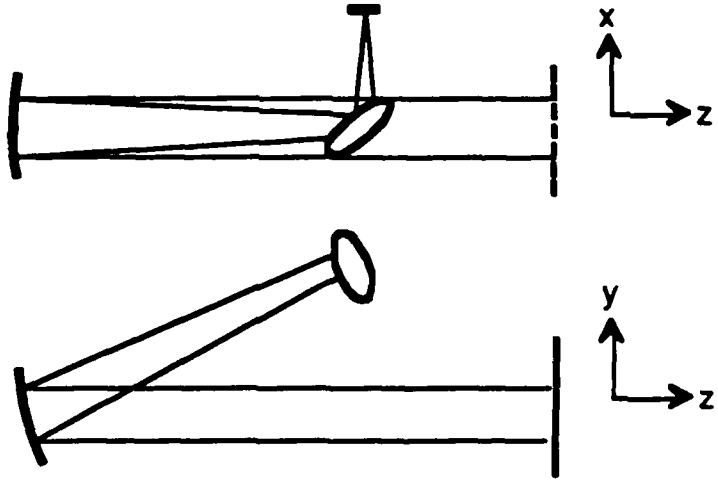

Figure 6.2
Top and side views of the orientation of the first grating relative to the collimating mirror and arc source. The grating lines are parallel to the y direction (out of the page).

6.2.2. *Gratings*

Gratings that were commercially available were supplied on glass substrates that do not transmit significant uv radiation below 365 nm. For this reason, it was necessary to fabricate gratings on fused silica substrates using a commercial grating as a mask. The gratings were purchased from Rolyn Optics and are stated as being 1000 line pairs per inch (25.40 μm grating period) and are 50 mm square. Measurements of the gratings gave a value of 25.45 μm for the period. These gratings were used as masks for the exposure of a photoresist film on a chrome coated fused silica substrates. After the excess chrome and photoresist were removed the resultant gratings had a ratio of opaque bar width to space width of approximately 40:60 (estimated visually by examination through an optical microscope).

The ability to check one grating against another by observing the moiré fringes formed when they are placed on top of each other provides a sensitive test of the quality of both the replication process and of the original gratings. No moiré fringes were observed under these conditions for either the masters or the replicas, indicating that any non-symmetrical cumulative errors in the position of the gratings' lines were less than 5 μm (assuming that the threshold for the observation of a fractional fringe is 0.2 fringes).

It was important to be able to align both gratings parallel to each other and perpendicular to the illumination. The second grating was held in a rigid mount that allowed the grating to move only in the plane of the grating. This was accomplished by placing opposite edges of the grating on two shallow lips machined into the mount.

The first grating needed to be positioned very accurately relative to the second grating. If the plane of the first grating were not parallel to the second grating, a variable shear could exist across the field and measuring the grating separations would

become very difficult. In order to provide 4 axis positioning ability (x-y plane, z axis, and rotation about the z axis) the first grating of the deflectometer was mounted on a small rotation stage with the axis of rotation oriented in the z direction (see fig. 6.3). The rotation stage was in turn attached to a micrometer driven kinematic mount providing tilt of the x-y plane. The whole assembly was then placed on a manual slide for z axis positioning. The manual slide was anchored to the mount for the second grating and provided the ability to adjust the separation of the gratings.

6.2.3. Alignment of the gratings

The alignment of the deflectometer is quite simple in comparison to the alignment procedure required for a Mach-Zehnder interferometer. Once the pinhole is illuminated and the beam is fairly well collimated the reference grating is positioned in the beam. Because the opaque bars on the grating are chrome, the back-reflected diffraction orders are easily visible on the surface of the pinhole mount. The position of these back reflections can be used as a guide in adjusting the beam until it is perpendicular to the reference grating. In the same way the first grating (or sample grating) can be aligned until its back-reflected diffraction orders overlap the reference grating's orders on the pinhole mount. Ideally, the two zeroth orders should be coincident with the pinhole.

6.2.4. Scanning the object

The method of scanning the image across the detector can have a very large effect on the accuracy of the deflectometer. Because the index profile is recovered from the phase data through numerical integration (eq. (5.7)), spatial errors in the phase versus position profile are translated into errors in the index profile. For this reason it is very important to minimize spatial registration errors, especially cumulative ones. This is discussed in detail later in this chapter.

There are many ways to scan the image of the object under test across a point detector. One method is to insert a mirror mounted galvanometer in the imaging optics so that the image is swept across the detector. This method is prone to errors from two sources: position errors due to angular positioning inaccuracies of the galvanometer and angular image distortion errors due to the effects of wavelength dependent field aberrations of the imaging optics, especially lateral color. To eliminate the effects of lateral color the detector can be placed on the optical axis of the imaging system. Scanning the image can then either be accomplished by translating the detector and optics together so that the object is scanned[1] or by translating the object itself[2,3]. It is the latter option that was chosen for this moiré deflectometer since the object is relatively small compared to the imaging optics/detector combination and is more easily mounted on a translation stage. Because the position of the stage and object can be directly read from the stage controller any systematic errors due to calculation of the optical magnification or distortion are eliminated.

An additional and important advantage of translating the object is that any spatially dependent noise, such as that caused by dust or a relative tilt or rotation of the gratings, does not affect the accuracy of the measurement. Other noise sources of this type include aberrations induced by the collimating optics and local variations in the period of the gratings. Again, these do not introduce position dependent errors in the measurement if the sample is translated.

An ORIEL Encoder-Mike model 18268 motorized micrometer was used to translate the stage on which the sample holder was mounted. The sample holder provided manually adjustable vertical positioning (y axis). The extension of the micrometer was translated by a shaft mounted encoder into electrical pulses with a resolution of 0.1 μm per pulse. The speed and direction of the micrometer was

controlled by an ORIEL controller, model 18007. Manual control of the micrometer was overridden by the computer during actual measurements.

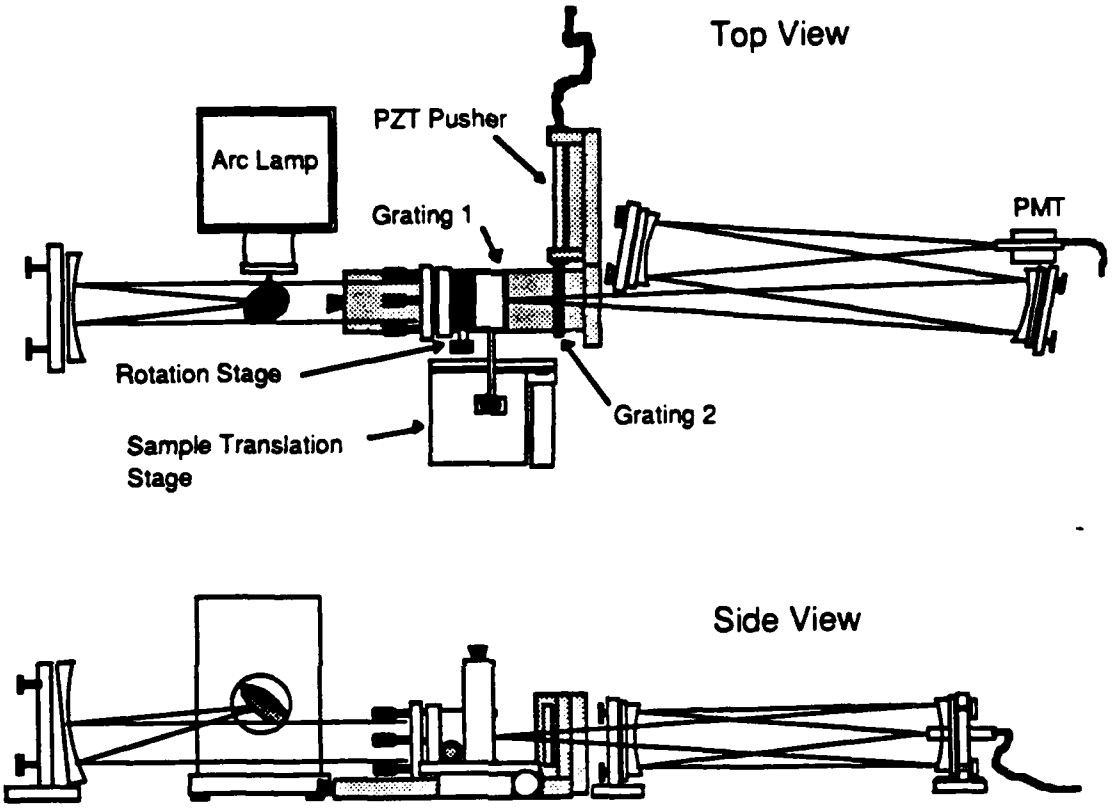

Figure 6.3
Two views of the layout of the deflectometer

6.2.5. Imaging Optics

For imaging the fringe pattern onto the detector two concave spherical mirrors were used which eliminated all chromatic aberrations. The focal lengths of the two mirrors were 400 mm and 120 mm The overall magnification was approximately 5.0. There were no errors from image distortion due to lateral chromatic aberration but the aberrations due to the off-axis Z configuration used were sizeable. Off-axis coma, astigmatism, and spherical aberration all contributed to a spot size that was

approximately 175 μm in the plane perpendicular to the grating's lines. The resolution at the object was thus 35 μm.

6.3. Deflectometer Apparatus: Electronics

6.3.1. Modulation electronics and PZT

As is discussed in chapter 5, to accurately measure the phase a psuedo-heterodyne method known as harmonic phase modulation is implemented. This method involves modulating the position of the second grating with a sine wave plus its first harmonic. Modulation of the position of the reference grating (the second grating) is provided by a Burleigh PZT pusher model PZ-40 which has a maximum travel of 40 μm. The pusher was mounted in an aluminum frame which also held the reference grating. Positive contact between the edge of the grating and the pusher end cap is maintained by a small steel spring.

The PZT was driven by a Burleigh high-voltage amplifier, model PZ-70, which provided gain and offset to a low voltage input. The required phase modulation was of the form:

$$\Psi(t) = A\,sin(\omega t) + B\,sin(2\omega t + \alpha) \quad . \tag{6.1}$$

It was necessary to have the amplitude and phase of either the ω component or the 2ω component adjustable so that the correct values could be set for A, B and α. Once the phase and the ratio A/B had been set correctly, the gain on the Burleigh amp. could be adjusted until the system was linearized. This was the point at which the detected phase was equal to the optical phase. The ability to adjust the relative amplitude and phase of the two components of the phase modulation was also necessary in order to determine the effects of non-ideal modulation and to compensate

for any frequency dependent phase shifts or amplitude errors introduced by the amplifier or by non-ideal response of the PZT.

To generate the phase modulation signal (eq. (6.1)) the sine wave output from the lock-in amplifier oscillator was amplified and then was used as the input to an electronics board manufactured by Evans Electronics (model 4114). The output of this board was a square wave that was locked in phase to the input wave and was the first harmonic of the input signal. The phase of the output was adjustable by ± 180 deg. relative to the input using an on-board potentiometer. The 2ω square-wave was low pass filtered to yield a 2ω sine wave which was then summed using a variable gain circuit with the original signal. This signal was amplified by the Burleigh HV amplifier to drive the PZT.

The fundamental frequency, ω, is chosen to be as far from sources of electrical noise as is possible. This could be accomplished by choosing ω to be several kilohertz or higher. Unfortunately, a PZT acts as an almost purely capacitive load to the amplifier. High frequencies require large currents from the amplifier. The Burleigh amp. has a current limit of 22 mA. Knowing the current limit, I_{max} and the capacitance of the PZT, C the maximum operating frequency can be calculated using[4]:

$$f_{max} = \frac{I_{max}}{2\pi CV} \quad , \tag{6.2}$$

where V is the peak-to-peak driving voltage for the PZT. Using this equation and assuming operation near the peak signal to noise ratio for the harmonic modulation scheme, a value for f_{max} can be calculated to be approximately 105 Hz. In actual tests the current limit for the amplifier is somewhat higher (or the capacitance of the PZT is higher) than that stated by the manufacturer. A fundamental frequency of 95.6 Hz. is

used as the best compromise between the components available and the maximum driving frequency possible.

Figure 6.4 shows a schematic of the electronic layout for the deflectometer. The only component not discussed here is the computer, which is an IBM PC-AT. The lock-in amplifier provides the ability to communicate with any device using either an IEEE-488 or an RS-232 communications protocol. Commands can be sent to the lock-in to control the output of up to 2 D/A's and read the input of up to 4 A/D's in addition to reading the value of the detected signal's phase and amplitude.

6.3.2. Detection: PMT's and Lock-In Amplifier

Detection was accomplished using Hamamatsu end-on photomultiplier tubes, type R960. A slit with a length of 10 mm and a width of 100 μm was used to limit the effective detector size of the signal PMT. Gain voltage for the PMT's was provided by a Bertan model PMT-20A d.c. to d.c. converter. The output current from the signal PMT was fed directly into the current input of the lock-in amplifier without any pre-amplification.

The lock-in amplifier (LIA) amplifies signals that are coherent with the reference signal while filtering out any signals that are not coherent with the reference and are more than a few millihertz away in frequency. This is accomplished by generating a precision sine wave using a phase-locked-loop that is locked to the reference signal's phase and frequency. Next the signal is isolated by mixing (multiplying) the input voltage containing noise and the signal to be detected with the precision sine wave. The d.c. component of the mixed signal results entirely from the product of the signal to be detected and the reference sine wave and has an amplitude proportional to $\sin(\theta)$, where θ is the phase of the signal. A low pass filter (the "pre-filter") then removes all a.c. noise. This scheme is extremely effective in removing any noise that is not at the same

frequency as the reference. This procedure is carried out simultaneously in two parallel channels with one channel using a precision cosine wave instead of a sine wave, which results in a d.c. signal proportional to cos(θ). The arctangent of the ratio of the outputs of these two channels is then equal to the phase of the input signal.

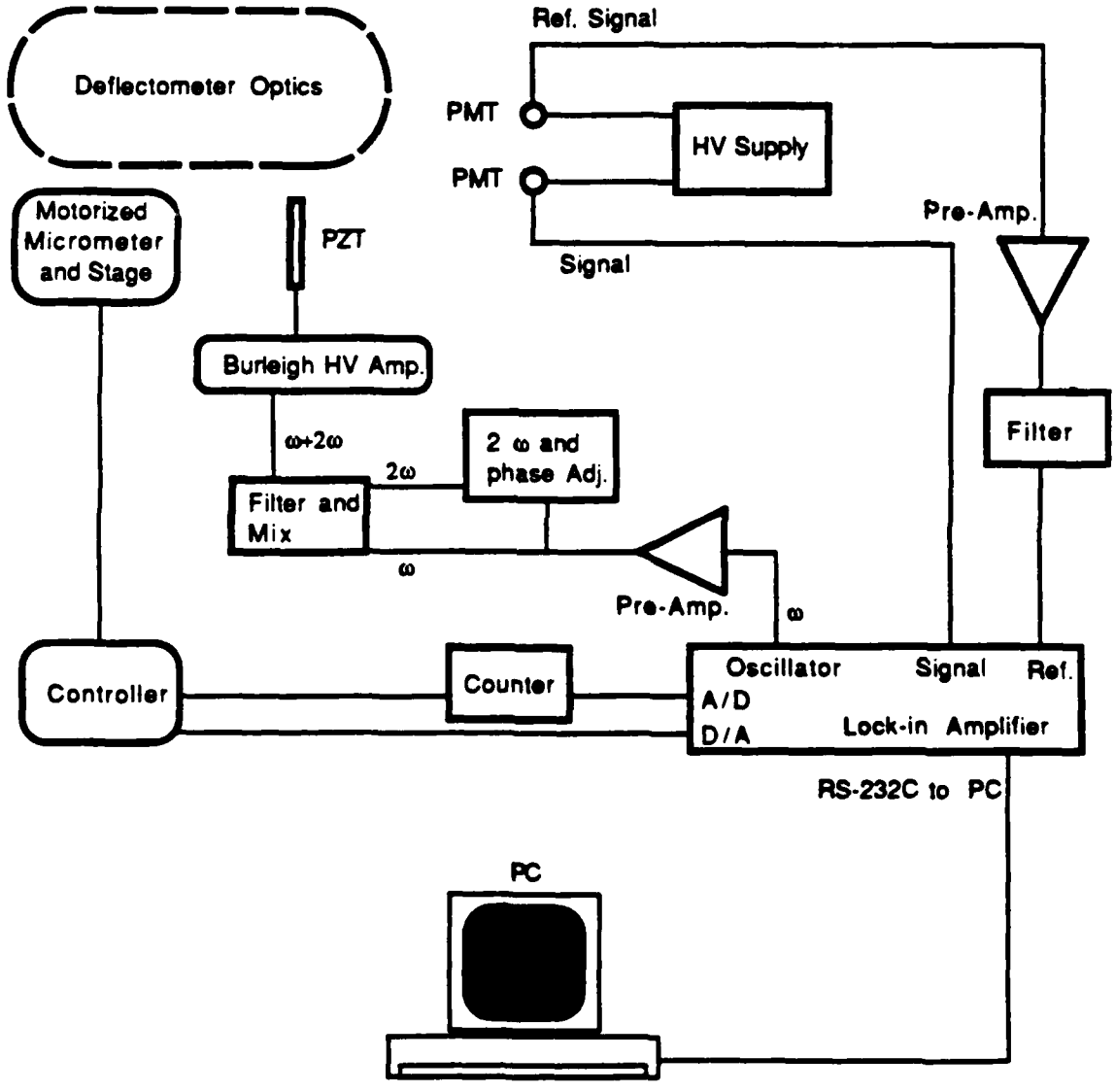

Figure 6.4
Electrical schematic for the phase retrieval electronics.

Because the LIA provided isolation of the signal from any coherent noise more than a few millihertz away in frequency, the phase of signals with amplitudes as small as 3.0 pA. were detectable. The reference signal was taken directly from the oscillator signal used to drive the PZT. Ideally the reference signal should be taken directly from an unobstructed (by the sample) portion of the image field. Unfortunately, due to the size of the sample and the fact that the sample was translated across the field, it was not feasible to do this.

6.4. Error sources and their correction

6.4.1. Random noise

Sources of error can be divided into two categories, either random or systematic, and then further subdivided into spatial and temporal categories. Systematic error sources include non-linearities between the detected phase and the optical phase, and a large class of errors involving translation of the raw phase data into index of refraction. Random error sources included noise from mechanical vibrations, spatial noise caused by inhomogeneities in the sample, thermal air currents, and electrical noise such as fluctuations in the PZT and PMT supply voltages. Random temporal noises with time constants less than the pre-filter time constant were eliminated by the lock-in amplifier. Time constants for the pre-filter were either 300 ms. or 1 s. Thus the above mentioned temporal noise sources, with the exception of noise from mechanical vibrations that occurred at the fundamental frequency,were eliminated. Random noise sources with time constants greater than the prefilter time constants such as fluctuating thermal currents in the air, and variations in the PMT and PZT driving voltages, resulted in a randomly varying phase noise with peak-to-peak amplitude of approximately 3 degrees (0.008 fringes). By placing the deflectometer apparatus on a vibration isolation table the noise could be reduced to approximately 2 deg. (0.003 fringes) This advantage was not sufficient to warrant the use of an optical table and indicated that most sources of noise were not mechanical in nature.

Translating random phase noise into index of refraction errors is straightforward. An error in the detected phase, ε_p, that arises at one datum point is translated into an error in the index profile, ε_i through the relation

$$\varepsilon_i = \frac{p\delta x}{t z_s}\varepsilon_p \tag{6.3}$$

(from eq. (5.7) for the calculation of the index of refraction), where the distance between measurements is δx. Using typical parameter values of $\delta x = 0.030$ mm, p = 25.4 μm, $z_s = 20$ mm, and t = 3 mm, a phase error of 20 deg. (0.055 fringes) leads to an error in the index profile of 7×10^{-7}. This is an order of magnitude less than the error in index that would arise in a Mach-Zender interferometer under the same conditions (at a wavelength of 500 nm.). From this example it can be seen that the effect this type of random noise has on the index profile is negligible. Noise that exists over some longer period of time that includes more than one datum point is not so easily dismissed. Noise of this type has a cumulative effect on the index profile that can quickly add up to a significant value. An example of this type is thermal fluctuations in the air. A spatially dependent thermal fluctuation of the ambient room air could cause phase shifts that, if they existed for long enough, would contribute to a phase error over some distance on the face of the sample.

To determine the magnitude of random temporal errors, sets of three identical scans were made over a sample at the same wavelength, with each scan separated in time from the next by approximately 10 minutes. The difference between any two scans in a set was roughly 0.006 fringes (rms). Figure 6.5 shows a plot of the phase difference between two successive scans. Also included in the figure is the index of refraction errors that arise from these phase errors. From this it can be concluded that random temporal errors are not sources of significant phase error.

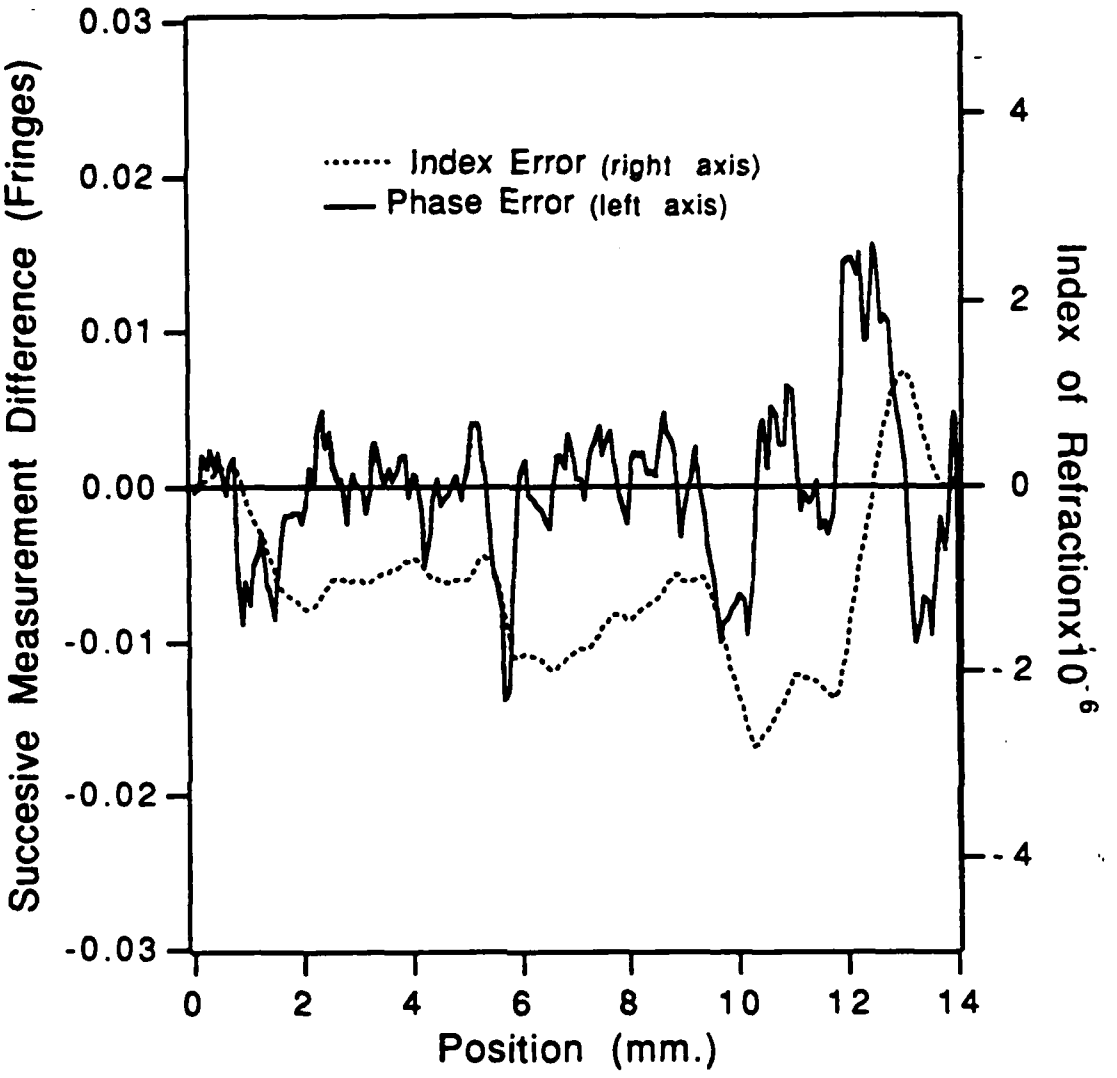

Figure 6.5
Plot of the difference between two scans of a sample separated in time by approximately 10 minutes and the associated index of refraction error. The measurements were made at a wavelength of 577 nm. (Sample MH721)

6.4.2. Systematic errors

It was found that the sources of error that lead to significant errors in the index of refraction profile all came under the category of systematic errors. Some examples of systematic error are nonlinearities in the relationship between the detected phase and

the optical phase, errors in locating the zero delta-n region, and spatial registration errors between scans made at different wavelengths.

Although the index error due to a phase error at one data point may be small, because the calculated index of refraction is a cumulative value, errors that are correlated over several data points can sum to a significant index error. This applies to random errors as well as systematic errors and is the major source of index of refraction error in the deflectometer. The most obvious source of systematic error is an error in the modulation of the grating position. This could be caused by either errors in the driving voltage itself or errors in the PZT response to the driving voltage. The effect of this type of error is to introduce a non-linear relationship between the detected phase and the optical phase, as was demonstrated in chapter 5. The systematic errors in the detected phase then have a period that is twice that of the phase of the fringe pattern. This means that the index errors are also periodic, with a period that is twice that of the fringe pattern. The index error due to a sinusoidal phase error with an amplitude of 0.05 fringes, using the numbers from the previous example, results in a maximum cumulative error in the index of approximately 2×10^{-6}, which is not very large. Fortunately, whether their effect is large or not, the repeatability of these errors allows their removal.

In previous work by Miceli[5] the nonlinearities in the system were characterized by first scanning tilt fringes and then recording the point by point difference between this result and the expected result, a straight line. This information was then used to generate a look-up table which was used to transform data as the sample was scanned. This method had one flaw, in that any random errors particular to the first scan of tilt fringes were then replicated in all successive data.

Figure 6.6 shows a plot of detected phase versus optical phase for a non-ideal phase modulation of the moiré deflectometer. It can be seen in the figure that the phase error is periodic with a frequency that is twice that of the fringe pattern. This error is the same for each 2π cycle of fringe phase and is assumed to be due to drive voltage errors or hysteresis in the PZT response to the drive voltage. This type of curve is easily generated in a system that scans across the object by adding "tilt" fringes to the field without the sample in place and then scanning the field. Because the moiré deflectometer used in this work does not scan across the field a satisfactory method of generating a known phase is to translate the first grating (object grating) in a direction perpendicular to the grating lines, in the plane of the grating.

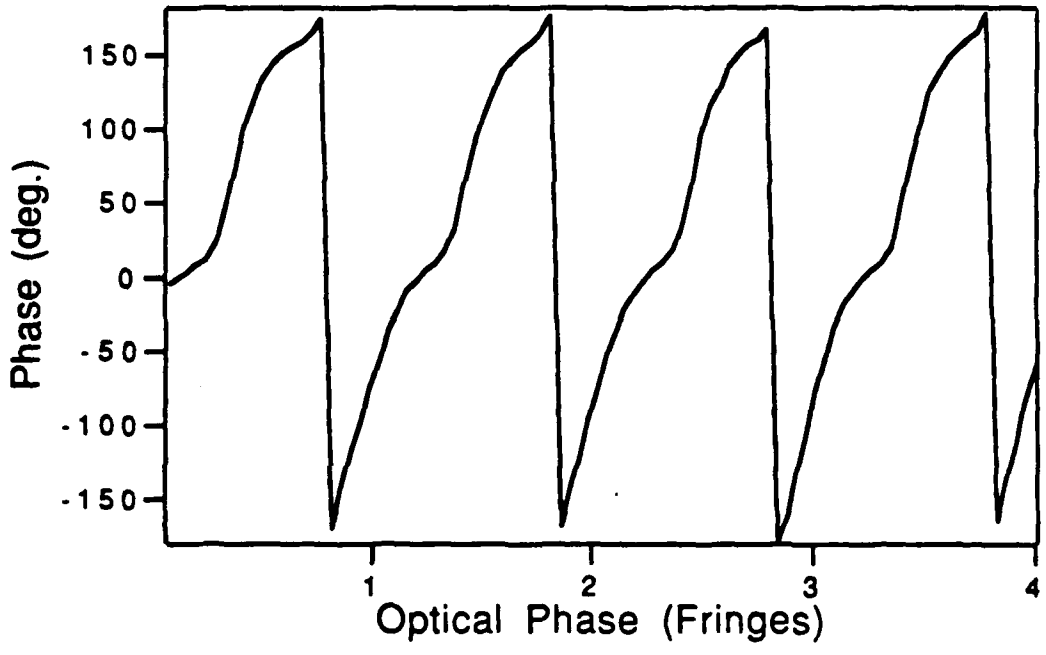

Figure 6.6.
Plot of the detected phase vs optical phase showing exaggerated nonlinearities.

The phase of the fringe pattern then shifts 2π each time the grating is translated a distance equal to one grating period. Distance is converted into optical phase by dividing the distance traveled by 25.4 $\mu m/2\pi$.

In order to quantify and remove these errors an iterative curve fitting routine is used to fit the coefficients of the equation

$$\varepsilon_{pm} = \beta sin(4\pi\theta + \phi) + \xi cos(4\pi\theta + \phi) \tag{6.3}$$

to the phase error. The form this equation takes is derived in chapter 5, eq. (5.50). The values for the coefficients β, ξ, and ϕ are then used to generate a look-up table. The measured phase is corrected point by point by finding its value in the look-up table and substituting the corresponding corrected value for it. Using this type of fit and not the actual data means that any other errors are not replicated (or corrected) in later data transformed using the look-up table.

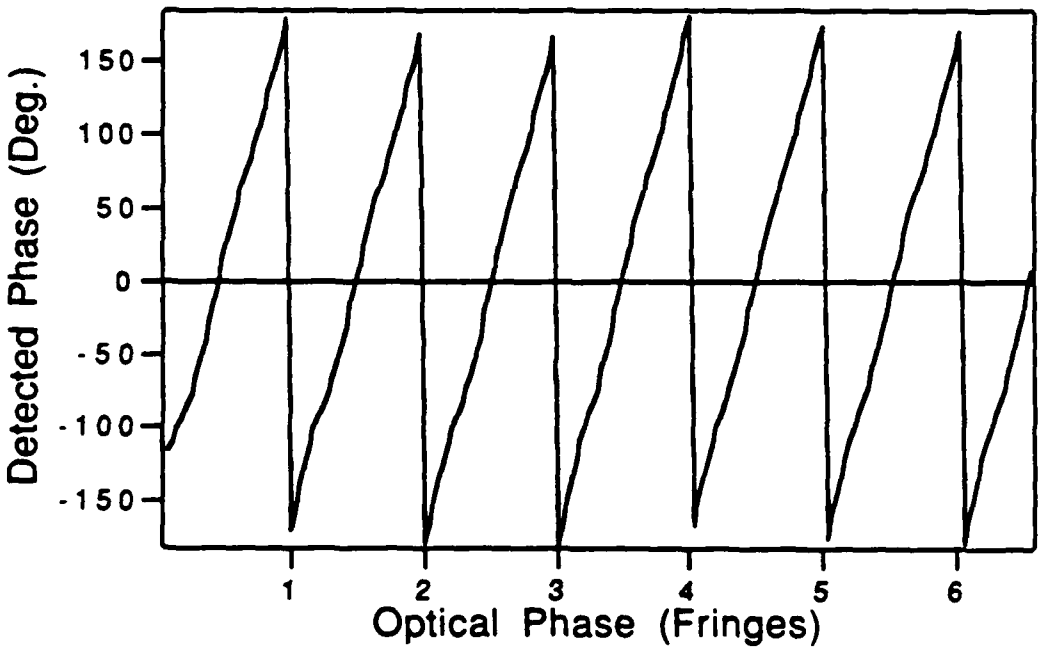

Figure 6.7
Wrapped phase as detected while translating the first grating.

The actual magnitude of the drive nonlinearities before the 2π phase jumps were removed is shown in fig. 6.7. The result of correcting the error is shown in fig. 6.8 as a plot of the phase error between the optical phase and the detected phase before and

after correction. It should be noted that the original data had a large period variation (approx, 0.03 fringes amplitude with a period of approx. 5 fringes) on top of the other errors. The large period variation was assumed to be due to local variations in the grating period from manufacturing errors and as such they did not affect the precision of the phase measurement. These were subtracted from the data before being plotted in fig. 6.8. The corrected error had an rms value of approximately 0.006 fringes which is roughly the same value as was arrived at for the effects due to random temporal noise.

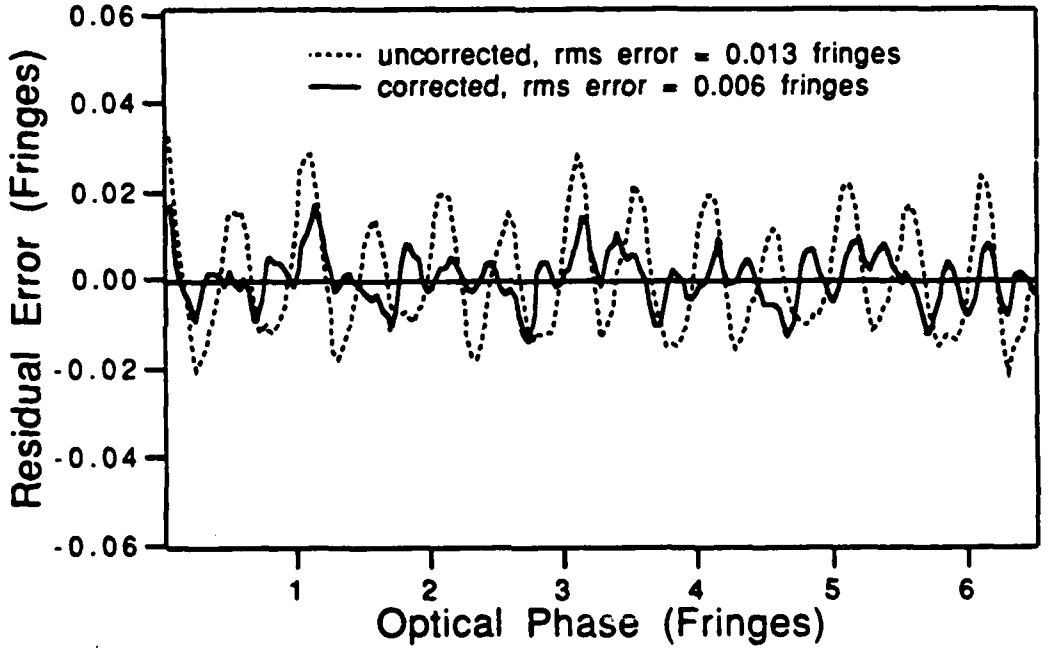

Figure 6.8
The effect of correcting the phase errors due to non-linearities in the phase modulation is shown. Typically, the errors before correction were 2-3 times larger than those shown here, which were the smallest achieved during this research.

Previous to this point in this discussion all the sources of error have been shown to be either insignificant or identifiable and removable. This is not the case for errors in determining the "zero point" for the delta-n or for errors in spatial registration from one scan to the next. Because the deflectometer only measures relative index

changes it is important that one part of the sample be homogeneous and that there not be any discontinuities in the index profile. The value of the phase in the homogeneous region of the sample is taken to be an arbitrary phase offset and is subtracted from the phase before the data is integrated to recover the delta-n. Errors in determining accurately this arbitrary offset, or "zero point", lead to an error term that is linear in the spatial coordinate. For example, an error in offset of 0.02 fringes leads to a total error in index of refraction of 8×10^{-5} over a scan with a length of 10 mm. To avoid this error care should be taken in determining where the homogeneous region is and then all the phase data should be offset by the mean value of the phase in this region. This is equivalent to removing slope errors in delta-n space.

Spatial registration errors, or shifts in the spatial coordinate from one scan to another, are particularly damaging when scans made using several wavelengths are used to calculate a dispersion number for the gradient.

6.5. *Results*

6.5.1. *GRIN Delta-n measurements*

In order to check the accuracy and precision of the deflectometer, measurements were made first on a gradient-index glass sample fabricated by Bausch and Lomb[6] using the ion exchange method. The ion exchange was an Ag^+ for Na^+ exchange in a Bausch and Lomb research glass, denoted BL2406. The total change in index in the sample measured, BL15a, was 0.013 at a wavelength of 633 nm. over a depth of approximately 8 mm. After aligning the deflectometer using a grating spacing of 17.20 mm with a He-Ne laser as a light source, the index gradient was measured.

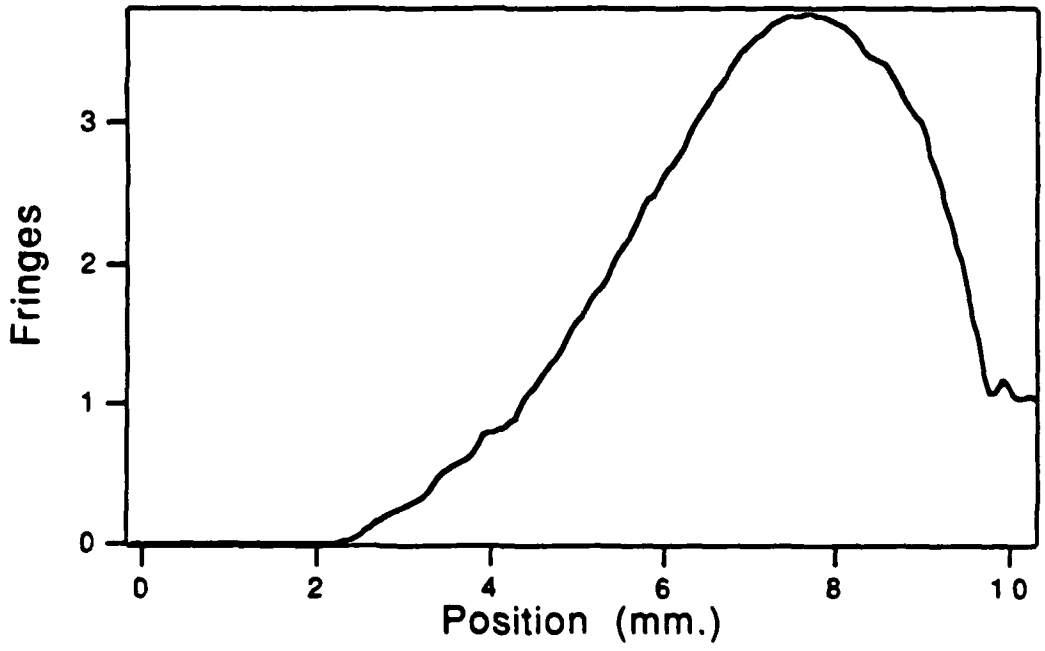

Figure 6.9
Unwrapped phase data for sample BL15a taken using the moiré deflectometer with a wavelength of 632.8 nm.

Figure 6.9 shows the phase data after 2π phase jumps and systematic nonlinearities have been removed. There are relatively few fringes when compared with the approximately 37 fringes present when the sample is placed in a Mach-Zehnder interferometer.

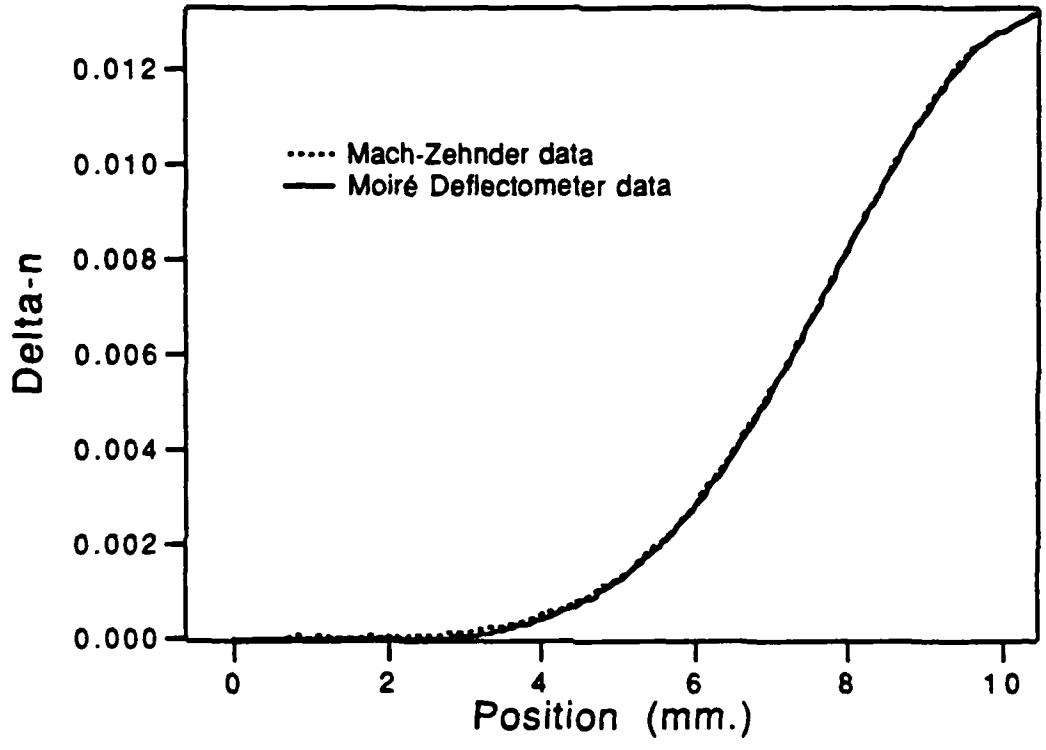

Figure 6.10
Delta-n profile for sample BL15a showing scans from both the moiré deflectometer and the Mach-Zehnder interferometer. The profile from the deflectometer is calculated from the data shown in figure 6.9.

The results of integrating the phase and scaling by the appropriate factors (see eq. (5.7)) are shown in fig. 6.10. The difference between this calculation and calculations made using data from a Mach-Zender interferometer, also operating at a wavelength of 633 nm. is shown in figure 6.11. The maximum difference between the two measurements is 8×10^{-5} in index.

On this scale the differences between the integrated deflectometer data and the more directly measured index of refraction are almost indiscernible. This is an impressive demonstration of the precision with which the deflectometer can measure small index changes. Better results in terms of the accuracy of the measurement would be obtained if there were more fringes present, due to a steeper index of refraction profile or a thicker sample.

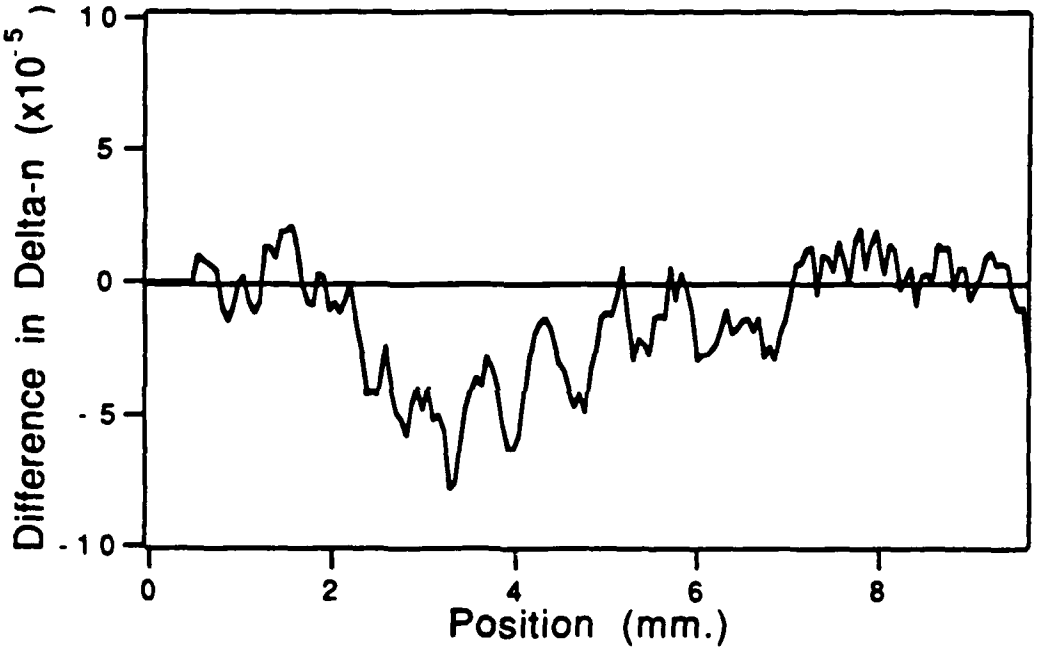

Figure 6.11
Difference between the Mach-Zehnder profile and the Moiré deflectometer data.

Figures 6.12 and 6.13 show a similar comparison of measurements for a GRIN Ba/CaF_2 crystal, sample MH721. This sample had approximately four fringes present at a wavelength of 632.8 nm. in the Mach-Zehnder interferometer and approximately one half of a fringe present in the moiré deflectometer.

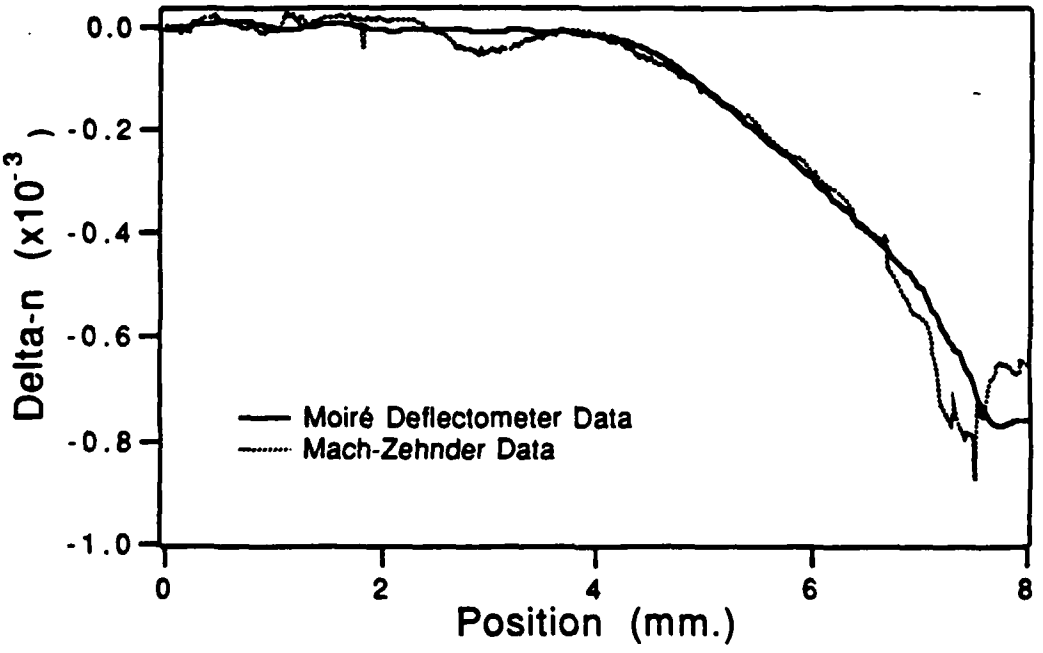

Figure 6.12
Index of refraction profiles calculated from deflectometer data and interferometer data for sample mh721, a GRIN fluoride crystal. The wavelength is 632.8 nm.

Interferometric scans of the GRIN crystal along scan lines separated by 50 μm on the sample face showed some small variations in delta-n. This could be also observed qualitatively in interferograms of the crystal. These variations were caused by spatial variations in the growth rate of the crystal across the growth interface, and were described in Chapter 4. The point to be made is that scans made with different instruments are not necessarily coincident to better than 50 μm. With this in mind it was decided to compare consecutive interferometric scans with each other and then also with the data from the deflectometer. These results are shown in fig. 6.13.

It can be seen that the accuracy of the deflectometer is only slightly less for the measurement of the crystal than in the measurement of the GRIN glass (fig. 6.11).

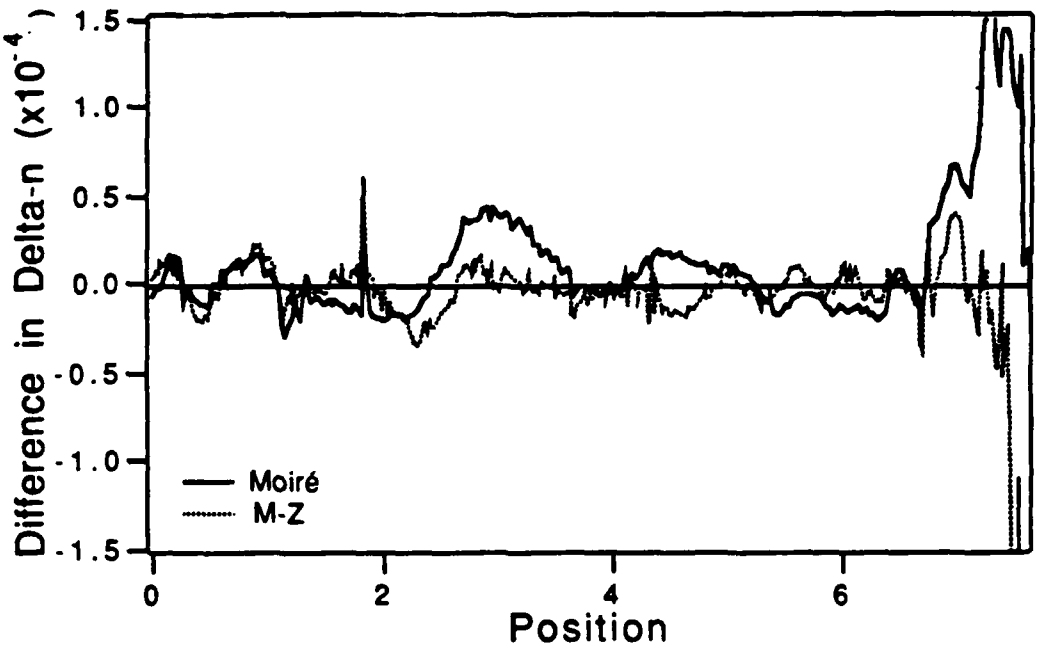

Figure 6.13
Difference between consecutive spatially separated Mach-Zehnder scans and the difference between a M-Z scan and a moiré deflectometer scan.

This is due to the fact that even though the change in the index of refraction is very different for the two materials, the derivative of the index is much closer in magnitude and it is the derivative that the deflectometer measures directly.

6.5.2. Dispersion measurements

The ability to measure the index profile at many wavelengths coupled with the inherent achromatism of the moiré deflectometer raises the possibility of measuring the gradient dispersion.

The gradient Abbe number, or the dispersion measured relative to the d, F, and C spectral lines, is defined for gradient material as

$$V_{GRIN} = \frac{\Delta n_d}{\Delta n_F - \Delta n_C} \quad . \tag{6.5}$$

Theoretical predictions of the dispersion values for GRIN glasses have been made based on a composition model by Ryan-Howard[7]. The gradient dispersion has been measured by several different methods[8, 9, 10]. All of these method have suffered from a lack of accuracy due to the difficulty in accurately measuring the delta-n.

Because the dispersion calculation is proportional to the inverse of a small difference, small errors in the measurement of Δn at any wavelength are greatly magnified. The relative uncertainty in the V number, δ_V, can be written as:

$$\delta_V = \delta_{\Delta n} V\sqrt{2} \quad , \tag{6.6}$$

where

$$\delta_{\Delta n} = \frac{\sigma_{\Delta n}}{\Delta n} \quad . \tag{6.7}$$

It has been assumed in the derivation of this relation that the error in measurement of the delta-n, $\sigma_{\Delta n}$, *is independent of wavelength and that the* Δn is roughly the same at all wavelengths. From eq. (6.6) it can be seen that GRIN materials with large values of the dispersion require much higher accuracy in the measurement of the delta-n relative to those with a smaller V number. For a given requirement on the accuracy of the dispersion measurement the requirements on the accuracy of the delta-n measurements are quite high. Figure 6.14 shows a plot of $\delta_{\Delta n}$ as a function of V for an error of 20 % in dispersion. The curves for other errors in the dispersion can be scaled linearly from this graph, so that to have an error of less than 2 % with a V number of 20, errors in the delta-n measurement would have to be less than 0.07 %. For a delta-n of 0.005 this implies an error of less than 3.5×10^{-6} in index, which is quite small. This type of accuracy is beyond the ability of the deflectometer for samples like those measured and shown above.

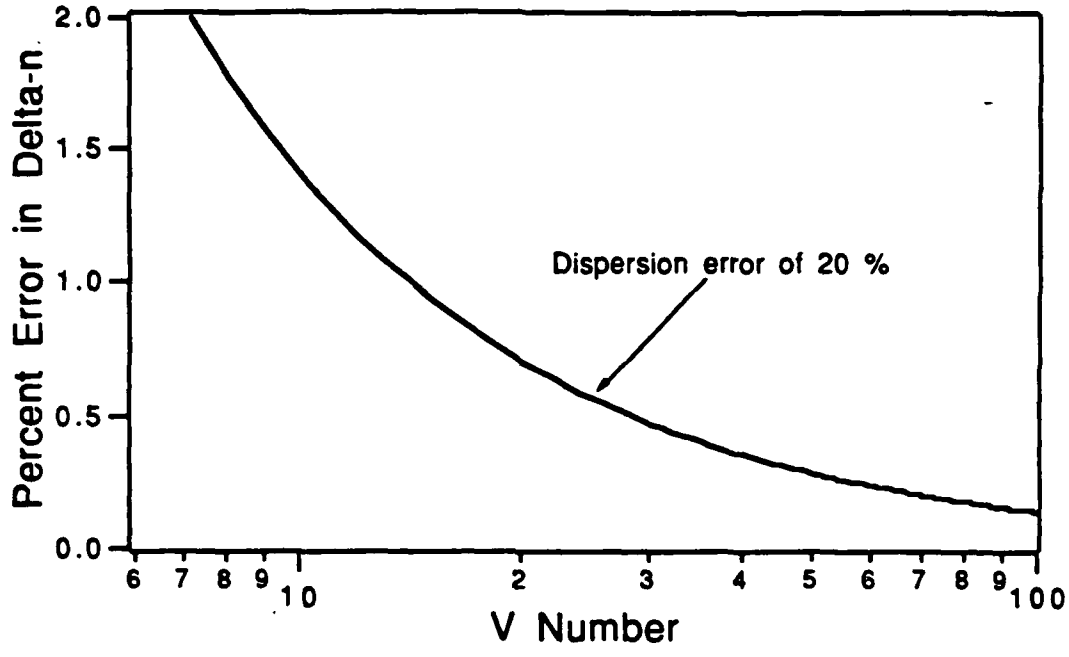

Figure 6.14
The accuracy needed in delta-n to achieve a dispersion error of 20 % .

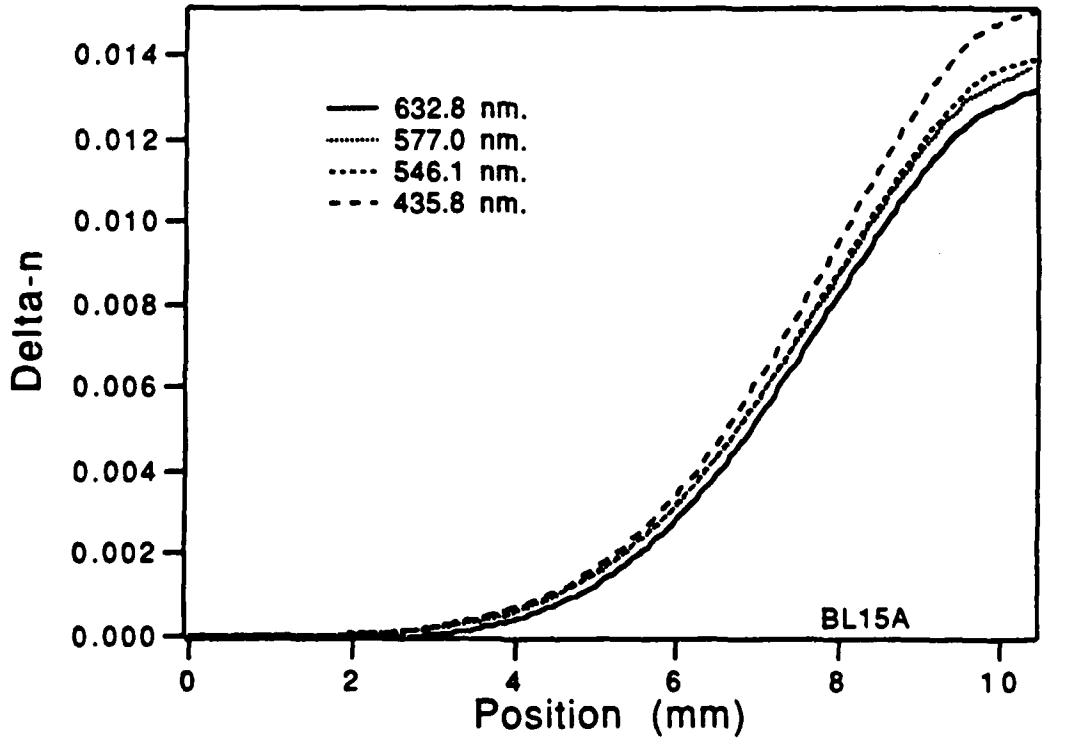

Figure 6.15
Measurement of the delta-n for GRIN glass BL15a at four wavelengths.

Sample BL15a was measured at four wavelengths using a He-Ne laser and the first three high intensity lines of a Hg arc. The results of the index calculation using this data is shown in fig. 6.15. The three Hg lines were then used to calculate the relative dispersion of the gradient using eq. (6.5). A theoretical estimate of the gradient dispersion for these wavelengths was calculated using the dispersion model and data from Ryan-Howard. The result was a value of approximately 13.2. It was not known what the uncertainty is in this value. However, data presented by Saxer[11] for measurements of the Abbe number of BL15a confirm the validity of the dispersion model to at least ±2 in dispersion number.

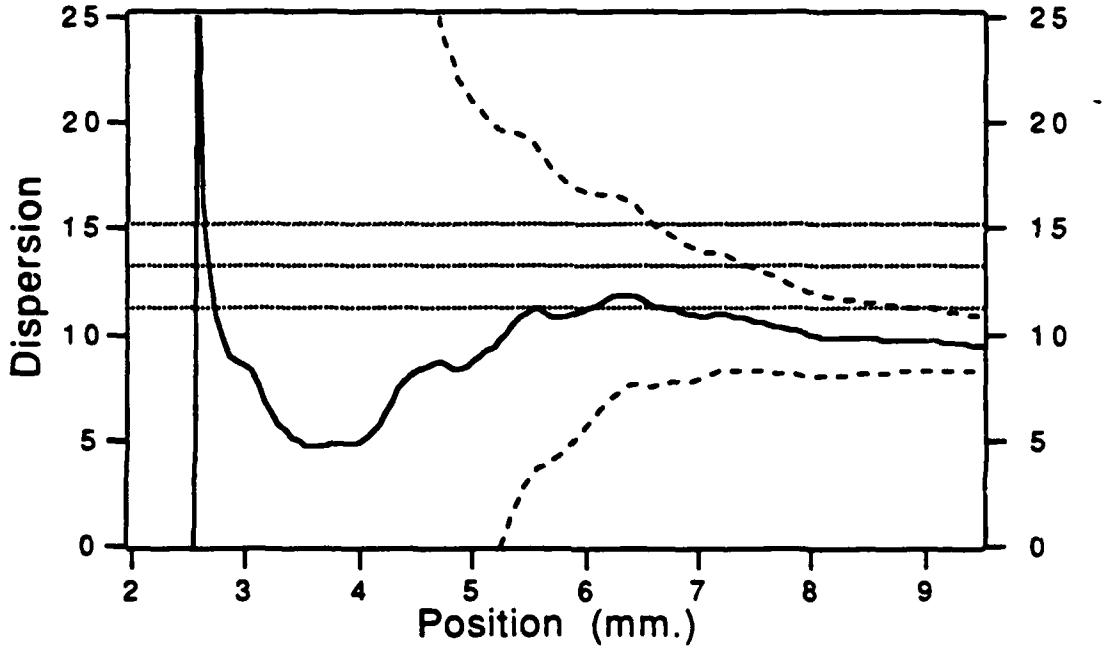

Figure 6.16
Dispersion measurement for BL15a. Wavelengths used are 577, 546.1, and 435.8 nm. The central dotted line represents the theoretical value of 13.2.

Figure 6.16 shows the result of the dispersion calculation using wavelengths of 546.1 nm., 435.8 nm., and 577 nm. The three horizontal dotted lines represent the nominal value and ±the uncertainty. The dashed lines represent an error of 1 percent in

delta-n. It can be seen that the dispersion data is in general too low relative to the nominal value. This could be caused by any of the systematic errors discussed earlier. In general the accuracy is too low for measurements of fringe patterns consisting of so few fringes.

Measurements of the GRIN crystal mh721 were also carried out using all the major Hg arc lines from 546.1 nm. down to 314 nm. in the mid ultraviolet. Each measurement was made with an interference filter in front of the arc lamp. The filters had a nominal FWHM of 10 nm. Measurements using the 250 nm line were not possible due the weakness of the signal, most likely caused by the reduced reflectivity of the mirror coatings at that wavelength, in conjunction with the low transmittance of the interference filter (approx. 14 %). The results of all measurements are shown in fig. 6.17. The grating separation was 24.65 mm for each measurement.

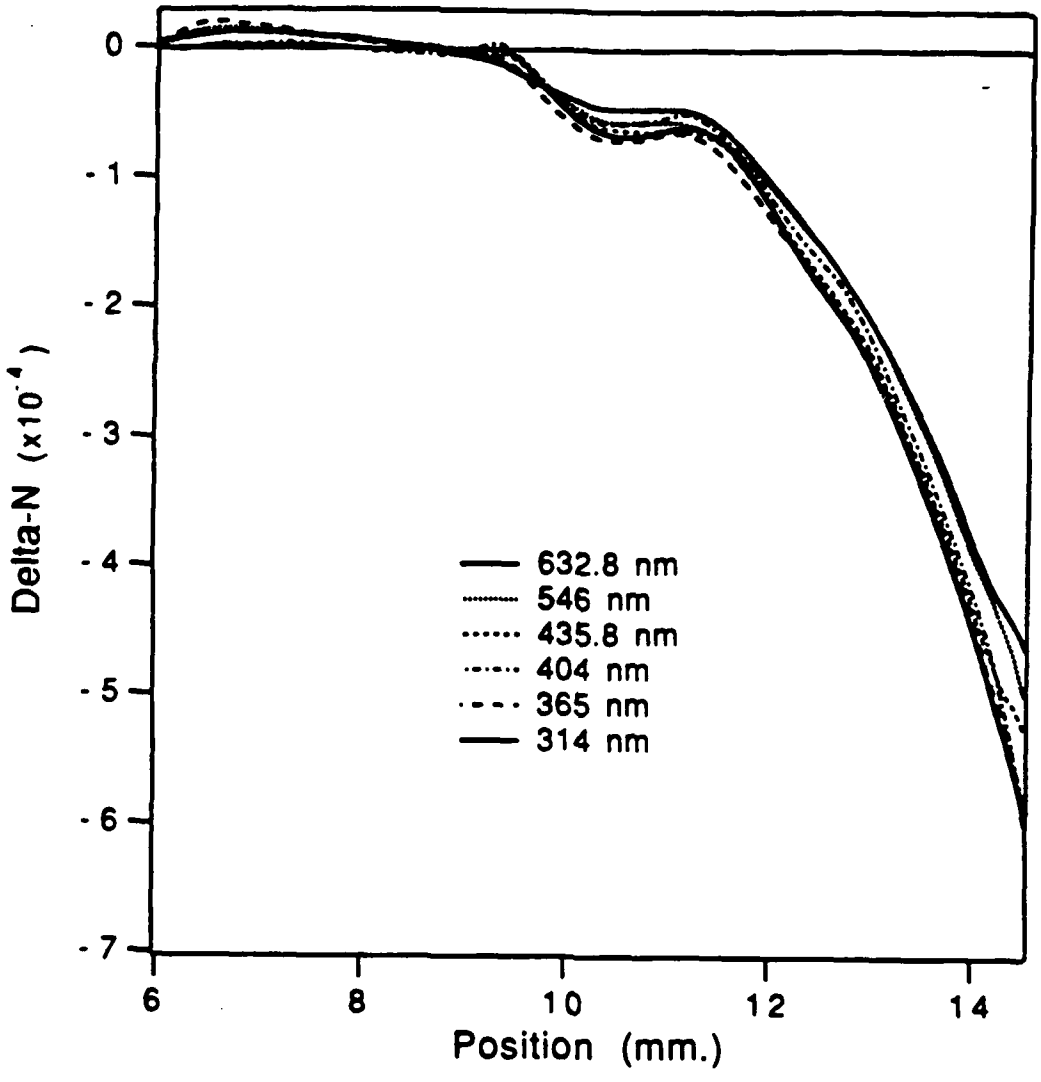

Figure 6.17
Results of calculations of the delta-n for crystal mh721 from deflectometer measurements at six wavelengths.

As can be seen in the figure there are variations in the delta-n at each wavelength that at some points cause the curves cross each other. In order to more accurately calculate the dispersion in the presence of these variations, the delta-n as a function of wavelength was fit to a curve using a chromatic coordinate representation (a description of this is given in Appendix B). This is done at intervals along the spatial coordinate. The curve

fit at each spatial point is then used to interpolate the delta-n at the desired wavelength(s).

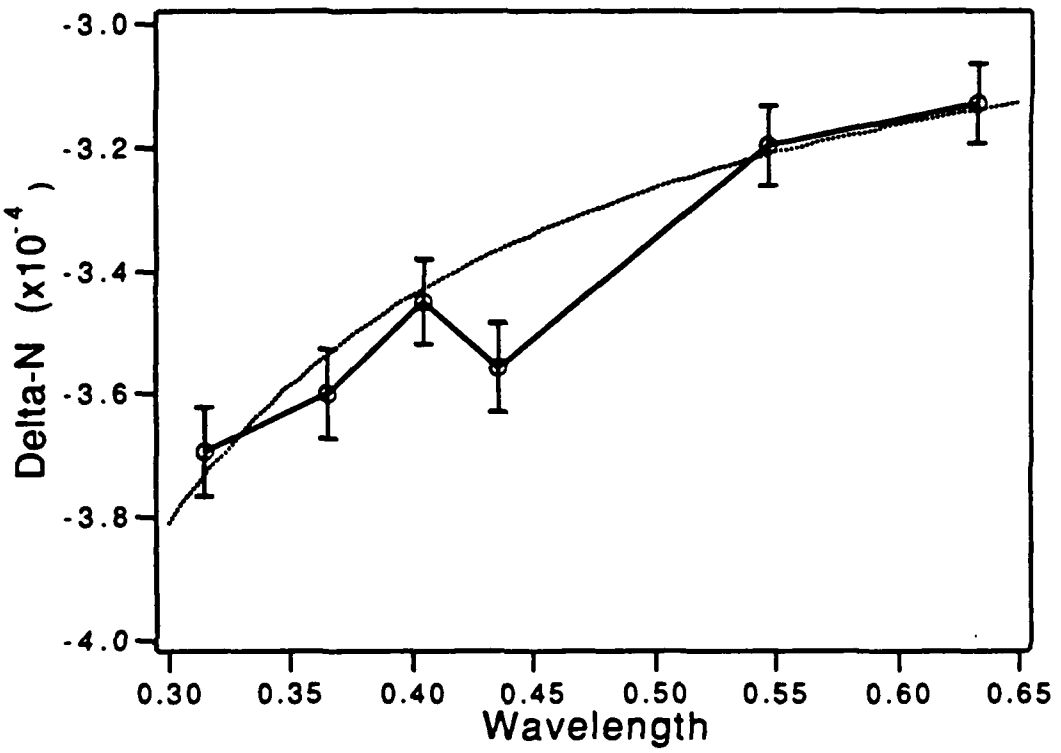

Figure 6.18
Plot of the delta-n as a function of wavelength for MH721 at a position of 14 mm The error bars represent a 2 % error in the delta-n.

Figure 6.18 shows the data from measurements at 6 wavelengths along with the curve that was fit to the data. The data for a wavelength of 435.8 nm is consistently out of the expected ordering and is not used for the calculation of the dispersion. The expected dispersion using wavelengths of 404, 365, and 314 nm is calculated to be 13.5 (coincidentally, almost the same value as for the previous example). The error bars represent an error of 2 % in the delta-n.

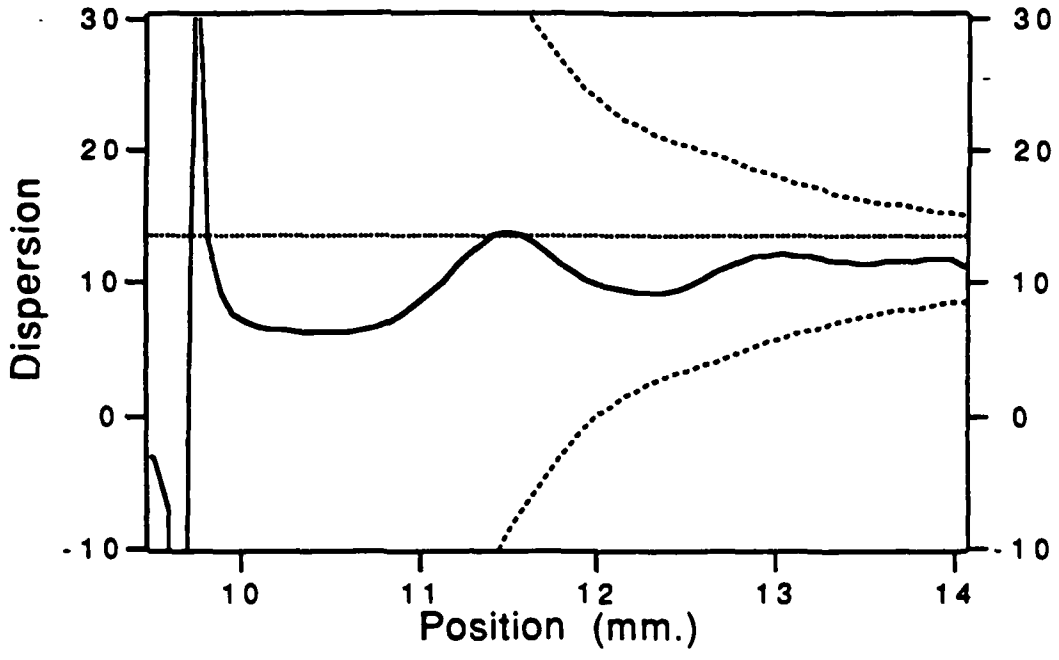

Figure 6.19
Dispersion data for MH721. Calculated using interpolated values at wavelengths of 404, 365, and 314 nm.

Figure 6.19 shows the result of the dispersion calculation. The horizontal line represents the theoretical value and the dashed lines represent the envelope of uncertainty due to delta-n errors of 5 $x10^{-6}$, calculated using eqs. (6.6) and (6.7). Relatively long scans were made to include a large part of the homogeneous region of the GRIN crystal to aid in a more accurate determination of the arbitrary baseline phase offset which was subtracted from the phase data before any calculations were carried out.

6.6. Summary

The harmonic phase modulation method has been successfully applied to the measurement of the phase of the moiré fringe pattern in order to match the accuracy reached in conventional interferometric phase measurement. Random noise was approximately 0.01 fringes in magnitude and did not significantly affect the accuracy of the deflectometer. Systematic errors introduced when locating the homogeneous region of the index profile were found to be a larger source of error and accounted for as much as 0.02 fringes of error.

Non-linearities in the detected phase due to non-ideal phase modulation were successfully characterized and removed using the equations derived in Chapter 5.

Measurement were made of the index gradients in a GRIN glass and in GRIN crystals grown for this thesis over a wavelength range that extended from 633 nm in the visible to 314 nm in the near uv.

V numbers were calculated for both types of GRIN material using the deflectometer data. The values calculated were close to the theoretical values, to within the predicted systematic error, for the crystals but not for the GRIN glass. This was due to systematic errors which differed from one wavelength to the next and did not cancel when the dispersion was calculated. A larger homogeneous region would eliminate the major source of error, the determination of the phase offset. This was successfully done during the measurement of the GRIN crystal.

References for Chapter 6.

---

[1]Masataka Shiba, Hitachi Corp.,unpublished work (carried out at the University of Rochester, 1987).

[2]G.E. Sommargren and B.J. Thompson, "Linear Phase Microscopy," Appl. Opt. **12** (1973) 2130.

[3]L.R. Gardner, *Studies in Gradient-Index Polymer Materials*, Ph.D thesis, University of Rochester, 1989.

[4]*The Piezo Book*, Burleigh Instruments, Inc. Burleigh Park, Fishers, NY.

[5]J.J. Miceli, *Infrared Gradient-Index Optics: Materials, Fabrication, and Testing*, Ph.D. thesis, University of Rochester, 1982.

[6]*Gradient-Index Optical Glass Lenses, Annual Report: June, 1975 through July*, 1976, NSF Research Contract ENG. 74-11993-A01, Principal Investigator: D. T. Moore.

[7]D.P. Ryan-Howard, *Chromatic Properties of Index of Refraction Gradients in Glass*, Ph.D. thesis, University of Rochester 1983.

[8]Ibid.

[9]L. Gregorka and D.T. Moore, "Chromatic Variation of Index of Refraction Gradients. Part 1," Appl. Opt. **19** (1980) 1096.

[10]C.E. Saxer and D.T. Moore, "Measurement of Chromatic Properties of Gradient-Index Glasses: Method and Results," presented at the 8th Topical Meeting on Gradient-Index Optical Imaging Systems, paper G16, Tokyo, Japan (1989).

[11]Ibid.

CHAPTER 7

Conclusions and recommendations for future work

7.1 Crystal Growth

The first goal of this thesis was to find a group of materials that transmitted ultraviolet light in which index gradients could be fabricated. Fluorides of barium and calcium were found to be ideal materials because of their transparency, index of refraction difference, and phase properties that allow the formation of a solid solution under the proper conditions. There are many other materials that meet the criterion of forming a solid solution while not meeting some of the other criteria. Another combination of materials that shows promise is strontium fluoride with barium fluoride. The index difference between these two is not very large but the region of solid solution is much larger than for Ba/CaF_2.

Mixed crystals of Ba/CaF_2 were successfully grown using Czochralski's method. Several other methods exist in which it may be feasible to fabricate controlled solid solutions. One possibility is to use the zone melting method with a sharply defined zone and a pre-doped charge, or to let the number of passes of the zone define the concentration gradient.

Actively doping the melt was found to be an effective method of increasing the concentration of the dopant in the crystal beyond the effects due to segregation. Adapting the crucible to this method was a key point. The use of a crucible with a coaxial design was used to limit the flow of dopant until it had thoroughly mixed with the melt, reducing problems associated with spatially fluctuating melt concentrations. Other configurations of crucible, crystal, and doping crystal may prove to be more controllable. Although it was not directly observed in this work, the existence of time

varying flow and spatial concentration variations in the melt may be reduced by using a crucible with a smaller central chamber where the crystal is being pulled.

A numerical method for predicting the concentration in the grown crystal, based on the growth parameters has been presented. This was partially successful, to the extent that the concentration changes could be predicted when the growth rate was known. In general, control of the growth was too dependent on operator skill. A means for diameter control is needed if profile control is to be obtained. Weighing systems for diameter control are described in the literature and would be ideal for this purpose.

The model for the crystalline index of refraction as a function of composition was found to be correct, within the limits of uncertainty for the concentration data.

7.2 Moiré deflectometer

The moiré deflectometer has been shown to be a sensitive instrument for the measurement of index gradients. Although its use was limited to the visible and the ultraviolet, relatively little work would have to be done to adapt it for use in the infrared region of the spectrum. The equations modelling the intensity in the image plane were useful in determining the effect of optical and electronic filtering on the detected intensity. This filtering was effective in increasing the signal contrast in conditions under which it would otherwise have been low or zero.

The harmonic phase modulation method was effective in recovering the phase of the moiré fringe pattern. An investigation into the effects of non-ideal phase modulation showed that the modulation amplitude errors and modulation phase errors can not be used to cancel each other, as had been previously thought, but instead induce orthogonal nonlinearities in the detected phase. Further investigation into other solutions for the amplitude of the phase modulation might yield solutions involving

lower amplitudes. This would be very interesting from a practical point of view, since small amplitude modulations are easier to achieve with current piezo technology.

The overall process of scanning the pattern point by point was rather slow. Using an N-bucket type method of phase retrieval in conjunction with a linear CCD array to "scan" across the whole sample at once would allow a quick measurement. This would lose the advantages of translating the object but would gain the advantage of a reduced number of mechanical elements. Another idea along these lines to be used in conjunction with a 2-D CCD array would be to use orthogonal pairs of gratings to produce the index gradient in both x and y directions simultaneously over the whole sample.

Dispersion measurements are easily made with the deflectometer. The parameter limiting the accuracy of the deflectometer is the number of fringes present. This could be increased by fabricating gradients with a large slope to increase the number of fringes. The advantages of using the deflectometer over an optical interferometer to make dispersion measurements increases in direct proportion to the optical wavelength used. This would make the deflectometer very attractive for far infrared measurements where the wavelength of the illumination approaches the period of the gratings.

APPENDIX A

Growth procedures using the CG800

The purpose of this appendix is to outline in detail the steps taken to grow a crystal using the Kayex CG800. The steps given here are not detailed anywhere else to the knowledge of the author, although the user's manual for the grower and discussions in the literature are helpful. The following steps do not replace a thorough knowledge of the materials involved or replace the experience necessary to grow good crystals with this system. They do give helpful details and minutia that otherwise might not be learned. Most of the comments in parenthesis refer to the growth of Si, while the rest is specific to fluoride crystals with the exception of any references to the diameter controller, which will not function when growing non-reflective materials.

A.1. Materials and grower preparation

Hot zone and crucible should have been previously baked out. Make sure interior of chamber is clean and free of deposits from previous use.

Jog crucible until top of crucible is level with top of heater. Note this position on crucible height indicator (steel rule on side of chamber).

Charge crucible, clean O-ring seal with iso-propyl alcohol and close lower furnace tank cover.

Fix seed in seed chuck using molybdenum wire (0.5 mm. is appropriate).

Clean the seed and the upper chamber seals carefully with alcohol.

Close upper chamber. Hand tighten lower ch. bolts. Use a wrench on the upper ch. to ensure a good seal.

Pump down to 50mT. Out-gassing will occur. Pump stays on throughout growth.

Turn on gas flow to pressure in chamber of 20 Torr (approximately 30-40 cfh)

Close valves on vacuum gages to protect them from fumes.

Set CL/SL ratio.

A.2. Melt

Turn on chilled water and check flow rate to crucible shaft (50 -60 gph).

Set Crucible Rotation (CR) to 2 rpm.

Set temperature controller to zero (0) output.

Turn on heater power. Set output to 20 (percent), until heater is visibly glowing approximately 500° C, then up power to 35 percent.

After charge has melted, set the Temperature Controller (TC) to Auto and lower the set point until the chamber temperature is slightly above the melting point of the charge (as experience dictates (AED)).

Note height of melt rel. to top of crucible and use this to determine the depth of the liquid, or use the weight of charge and density of the liquid to determine the depth (knowing the crucible dimensions). The sharp temperature gradient in the hot zone requires that the melt level be maintained from one run to another if repeatability of TC setpoint is desired.

Set CR and Seed Rotation (SR) to desired values (8 and 15 resp. for Si).

A.3. Growth of the crystal:

A.3.1. Neck

Lower seed into contact with melt. Start seed lift at a low rate (0.2 iph) Watch the meniscus. If it does not move outward indicating growth, lower the power.

Gradually increase seed lift (SL) until diameter is reduced to approx. 2-3 mm. (13 in/hr. for Si at 13.50mV on pyrometer). While carefully monitoring the meniscus diameter and adjusting the SL to keep dia. constant, grow a thin neck of 2-3 mm. length (approx. 10 cm. for Si).

A.3.2. Crown and Shoulder

Set seed travel indicator to zero.

Set SL to SL TRANS(fer) and reduce set point temp by approx. 5-25 or AED. Crown should start to form. To increase growth put Growth Control on Manual and adjust for a Temperature Rate of approx 0.5 set points/min. (ea. division = 0.25). (For a 2 in. dia. Si crystal the crown growth should take approx. 0.5 hr.)

(With photocells seeing melt surface only, use the Diameter Zero Adjust pot until the red pen is on line 10 (ref. point for dia. control).)

NOTE: For a melt back return CR to 1 rpm, raise temp 10-20 percent,jog SL down to melt off grown crystal and neck to desired point, then lower temp to previous set point, and start with new neck growth.

A.3.3. Body

When desired diameter is reached, set CL to CL/SL and control SL manually to maintain the desired diameter.

Position photocells onto the center of the meniscus, just outside of the brightest ring.

When the signal from photocells is approx. constant,or oscillating about a constant value (red pen), set SL to SL/TRANS and put Diameter Controller on Auto (the set point should be the value the photocell signal is oscillating about!!). This will automatically control the SL to maintain a constant reading from the photocells and hence a constant diameter crystal.

After 1-2 in. have been grown, and the seed lift is approx. constant (green pen), a seed lift set point close to that value should be chosen on the growth control panel (in 100ths of an inch) and the growth control set to Auto. The remainder of the crystal will now be grown automatically.

The growth control adds or subtracts signal from the temperature controller output (which remains constant), the rate is indicated on the GC meter (and the blue pen), until the seed lift set point is reached and maintained. Meanwhile, the diameter controller varies the seed lift in order to keep a constant signal from the photocells. Fortunately this two way battle for control of the growth rate is damped and a constant SL is reached, presumably that set on the GC panel.

For crystals which cannot be seen by the photocells (transparent or non-reflective) the operator will have to continuously visually monitor the diameter and adjust the heater temperature or SL appropriately.

A.3.4. Tail

As bottom of crucible is approached, the SL pen (green) will deviate more and more from the average rate. Shut off the CL.

Set Diameter Controller to Manual and SL to MAN, adjust to value set by DC.

Put GC panel in Manual. Adjust temperature rate to value set by GC auto.

Increase the temperature rate slightly, AED.

The crystal will now lift out of the crucible at the SL rate (reduces thermal shock). Adjust temp rate or SL to increase or decrease tail formation.

A.4. Shutdown

After crystal has pulled out of the melt, move through predetermined cool down cycle depending on crystal's thermal robustness. (For Si set SL to 20 in/hr. and shut off power after 1 hr.)

Set TC to Manual and adjust Output to zero.

Shut off Heater Power.

Run gas until temp. is well below melting point of charge.

Run cooling water until chamber temp. is <150 Celsius.

For Si, when viewing port glass has cooled enough to touch, chamber may be opened (shattering your silica crucible, naturally!).

In general, the main power to the control panel should be left on unless the grower is not going to be used for an extended period. The life of the relays in the panel is considerably shortened when they are cycled often.

APPENDIX B

The Use of Chromatic Coordinates in Describing the Chromatic Properties of GRIN Materials

B.1. Introduction

The purpose of this appendix is to present the rationale behind using a chromatic coordinate representation for the index of refraction of GRIN materials and to show some advantages in addition to the accuracy obtained with this representation. Most of this material was presented in a slightly different form at the 6th Topical Meeting on Gradient-Index Optical Imaging Systems, Palermo, Italy, 1985. A short discussion is included on the assumptions under which the gradient V number can be considered to be independent of composition.

Traditionally the dispersion of an optical material has been specified by its Abbe number, which gives knowledge of the slope of the index of refraction as a function of wavelength. First order theory then gives the appropriate lens powers to achieve the desired chromatic properties of the lens system. Knowledge of the Abbe number alone, however, is not sufficient to accurately describe the dispersion of most optical materials. A partial dispersion number is used to further specify the wavelength dependence. Together these two numbers give knowledge of the index of refraction at three wavelengths.

Unfortunately, since the index is not a linear function of wavelength, an assumption of linearity can lead to considerable errors in the regions between the known wavelengths, resulting in an unacceptable design. This is especially true in regions near an absorption peak where for most optical materials the index tends to be

highly nonlinear. This is the case for most optical materials when they are used in the ultraviolet region of the spectrum.

For the case of the common optical glasses, the Abbe numbers and partial dispersions, along with years of experience, have told the optical designer which glass combinations are effective in cases such as doublets and triplets. However, in investigating components fabricated of other materials, or in regions outside the visible, the optical designer does not have this experience as a guide. More recently Herzberger and McClure[1] have given algorithms for choosing achromatic combinations of glasses based on their abbe number and partial dispersion. At best these equations guarantee achromatization at a few discrete wavelengths and no information is obtained about the performance at wavelengths lying between these points.

Figure B.1 is a plot of index vs. wavelength for barium fluoride in the near ultraviolet, where most optical glasses have large absorptions. It is evident from this diagram that a linear approximation to the index in the uv is insufficient even for this material, which has absorptions much farther in the uv than most glasses. A prerequisite for any representation of the index of refraction is that it provide accurate index information while allowing a theory of the chromatic performance of any optical system to be concisely derived.

B.2. Representation of the index of refraction

Many different representations of the index of refraction as a function of wavelength have been proposed and used for interpolation of refractive indices. Some of the more prevalent include the Sellmeier equation,

$$N^2 = a + \frac{b\lambda^2}{c-\lambda^2} + \frac{d\lambda^2}{e-\lambda^2} + \ldots \qquad \text{(B.1)}$$

and the Schott equation,

$$N^2 = A_0 + A_1\lambda^2 + A_2\lambda^{-2} + A_3\lambda^{-4} + A_4\lambda^{-6} + A_5\lambda^{-8} \qquad (B.2)$$

These equations can be quite accurate. The Schott equation has a stated accuracy of better that 5 parts in the sixth decimal place[2]. Unfortunately, these expressions are rather unwieldy when used to derive a model for the chromatic properties of optical systems.

Buchdahl addressed the problem of obtaining a tractable series expansion for the chromatic properties of an optical system by introducing a variable transformation from λ to a "chromatic coordinate", $\omega(\lambda)$. The required properties of this transformation were that the index be representable as a polynomial series, ie.

$$N(\lambda) = \sum_{i=0}^{\infty} \upsilon_i \omega^i \qquad (B.3)$$

and that the series converge quickly. Buchdahl found that a transformation of the form

$$\omega = \frac{\lambda - \lambda_0}{1 + \alpha(\lambda - \lambda_0)} \quad , \qquad (B.4)$$

where α and λ_0 are constants, converged rapidly. He found that after three or four terms the series was accurate to better than 5 in the fifth decimal place.

The choice of variable transformation given by the coordinate is dependent on the material and the region of the spectrum over which the index is to be approximated. Forbes[3] has proposed other forms of this coordinate, the particular form used depending on the aforementioned parameters, and also computational methods[4] for calculating them.

The index of refraction of an optical material can be expressed as

$$N(\lambda) = N_0 + \upsilon_1\omega + \upsilon_2\omega^2 \qquad (B.5)$$

where N_0 is the index at the base wavelength, λ_0, with negligible loss in accuracy. Fitting the coefficients v_1 and v_2 of eq. (B.5) and α of eq. (B.4) to optical glasses using the same base wavelength λ_0, Buchdahl found that for the majority of optical glasses α was in the range of 2.3 to 2.7 μm^{-1}. He found that choosing α to be 2.5 μm^{-1} and refitting the index polynomial gave good approximations to the index of refraction for a large class of optical glasses while producing a tractable polynomial expansion for theoretical calculations. Mercado and Robb[5] have published results giving coefficients of the index expansion to second order in ω, for $\lambda_0 = 0.5461$ μm, which are sufficient to give the index accurately in the visible to 1 part in 10^5 for the majority of the commercially available optical glasses.

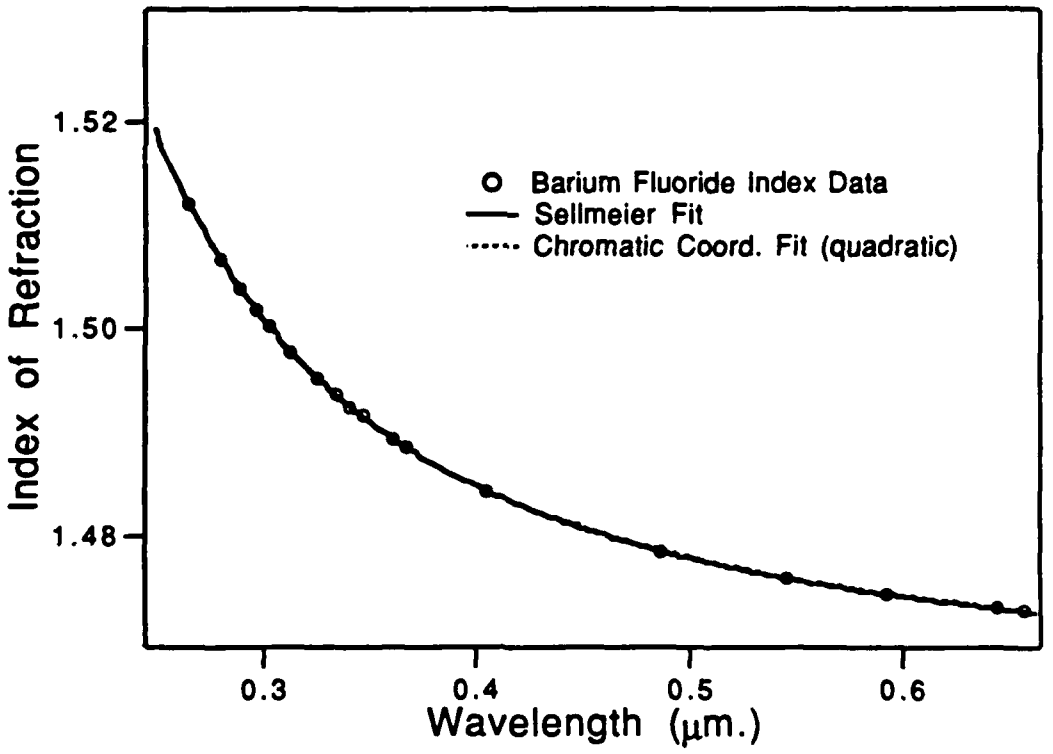

Figure B.1
Plots of index data and various representations of the index data.

A quadratic chromatic coordinate fit was used to match index data for fluoride crystals using Buchdahl's coordinate. The reference wavelength and α were chosen to give the best fit over the visible and uv portions of the spectrum for both BaF_2 and CaF_2. Figure B.1 shows a plot of the index data[6] for BaF_2 along with the Sellmeier representation[7] of this data, which has a stated accuracy of 1 in the fifth decimal place. Also plotted is the calculated index using the quadratic chromatic coordinate representation. It can be seen from the figure that both representations fit the index data well, and to the scale shown, lie on top of each other. Figure B.2 shows the actual difference between the Sellmeier representation and the quadratic chromatic coordinate fit. For most purposes the differences are negligible.

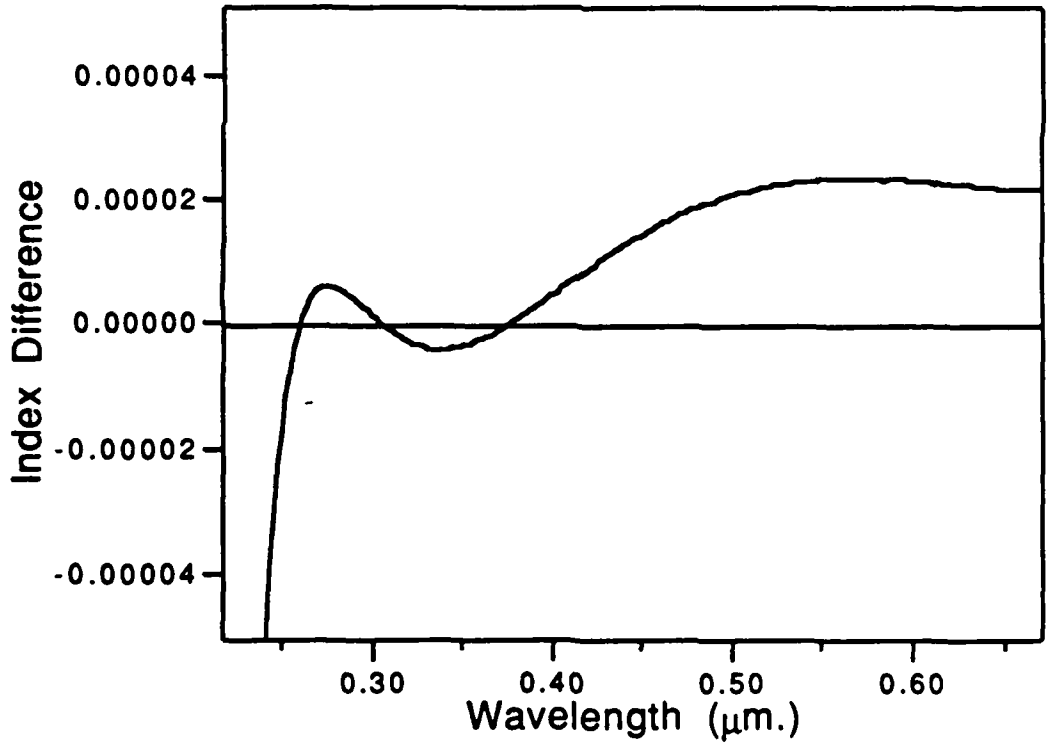

Figure B.2
Plot of the difference between the Sellmeier representation and a quadratic fit using Buchdahl's chromatic coordinate.

Because this index representation is very accurate, predictions of chromatic performance based on it are also very accurate, especially when compared with the three point accuracy of the traditional representation. Robb has published a graphical method for choosing optical glasses for achromatizing doublets[8] using the first two coefficients of the chromatic coordinate fit. He demonstrated that this method is superior over the older methods involving the Abbe number and partial dispersion by showing that the glass pairs chosen using his method give correction at four or even five wavelengths. This is in contrast to the two or at most three corrected wavelengths achieved using other methods. Buchdahl[9] comments that counting the number of corrected wavelengths is a rather arbitrary way of expressing the goodness of the fit. The correction is in fact perfect, to the extent that the fit coefficients accurately represent the index of refraction.

B.3. Chromatic coordinate representation of GRIN profiles

It would be hoped that this same type of representation and the optical system design methods using it would be applicable to GRIN materials. Generally, a process involving the addition of a gradient changes the dispersive qualities of the base material. It is of importance to determine what form this change takes, and to also determine what type of gradient dispersion is effective in correcting chromatic aberrations. Sands[10,11] has developed formulas based on a chromatic coordinate representation that include the chromatic behavior of GRIN materials. The purpose of the following derivation is to show that this representation allows the application of Robb's method involving the coefficients of the chromatic coordinate fit.

Explicitly including the wavelength dependence, the index representing a radial gradient can be written as:

$$N(\lambda) = N_{00}(\lambda) + N_{10}(\lambda)\rho^2 + N_{20}(\lambda)\rho^4 + \ldots \quad , \tag{B.6}$$

where ρ is the radial coordinate. Each coefficient of the radial coordinate can be expanded in a form similar to eq. (B.5):

$$\begin{aligned} N_{00}(\lambda) &= N_{00} + \nu_{00,1}\omega + \nu_{00,2}\omega^2 + \ldots \\ N_{10}(\lambda) &= N_{10} + \nu_{10,1}\omega + \nu_{10,2}\omega^2 + \ldots \\ N_{20}(\lambda) &= N_{20} + \nu_{20,1}\omega + \nu_{20,2}\omega^2 + \ldots \end{aligned} \quad , \tag{B.7}$$

where N_{ij} is the index at the reference wavelength and $\nu_{ij,k}$ is the coefficient of the index expansion in ω. Here ij refers to the coefficient of the index expansion as a function of ρ, while k indexes the coefficient of the kth power of ω. Note that only ω is a function of wavelength.

At this point the third order and higher terms in ω are dropped, as the first two are sufficiently accurate, and develop the aberration theory in terms of the coefficients $\nu_{ij,k}$.

Using Sands' notation, the equations for the chromatic aberration coefficients for a meridional ray in a cylindrical GRIN medium as a function of chromatic coordinate can be written as:

$$F_a = \sum_{k=1}^{m} F_{ak}\omega^k \qquad F_{ak} = \sum_{\text{all surfaces}} f_{ak} + \sum_{\text{all media}} f^*_{ak} \quad . \tag{B.8}$$

This form is the same as for the monochromatic aberrations of an inhomogeneous optical system given by Moore and Sands[12]. The chromatic aberration is made up of both a sum of surface contributions similar to the homogeneous ones, and a sum of transfer contributions unique to inhomogeneous media. Sands has given the form of these aberration coefficients to first order in ω (m=1). To fully utilize the power of

Robb's graphical method the second order terms (ω^2) need to be derived or at least approximated.

The first order surface contribution for a radial gradient is (Sands' eq. V (34))

$$f_{a1} = N_{00} y_a i_a \Delta\left(\frac{v_{00,1}}{N_{00}}\right) , \tag{B.9}$$

and the transfer contribution is (Sands' eq. II (35))

$$f_{a1}^{*} = -\nabla\left(y_a u_a v_{00,1}\right) + v_{00,1}\int_0^t u_a^2 v_{00,1}\,dz + 2v_{10,1}\int_0^t y_a^2 v_{10,1}\,dz , \tag{B.10}$$

where the ray has traversed a medium of thickness t in the z direction (parallel to the optical axis). y_a, u_a, and i_a are the paraxial meridional ray height, angle and incidence angle, respectively, evaluated at the reference wavelength. Quantities in the transfer equation refer to values in the medium only. ($\Delta(Q)$ is the change in Q across a surface while $\nabla(Q)$ is the change in Q from one side of a medium to another.)

Sands has also given the form of the second order chromatic surface contribution (Sands' eq. V (34)), as

$$\begin{aligned} f_{a2} &= N_{00}' y_a i_a \kappa_2 + \left(F_1 | i\right)\kappa_1 \\ \kappa_0 &= \frac{N_{00}}{N_{00}'} \\ \kappa_1 &= -\kappa_0 \Delta\left(\frac{v_{00,1}}{N_{00}}\right) \\ \kappa_2 &= -\kappa_0 \Delta\left(\frac{v_{00,2}}{N_{00}}\right) - \frac{v_{00,2}'}{N_{00}'}\kappa_1 \end{aligned} , \tag{B.11}$$

and the form of the second order transfer contribution (Sands' eq. V (35)), as

$$f_{a2}^{*} = -\nabla\left(y_a u_a v_{00,2} + y_a v_{00,1}\left(\bar{F}_1/u\right)\right)$$

$$+\int_0^t \left[u_a^2 v_{00,2} + y_a^2 v_{10,2} + u_a v_{00,1}\left(\bar{F}_1/u\right) + 2y_a v_{10,1}\left(\bar{F}_1/u\right)\right]dz \quad . \qquad \text{(B.12)}$$

From this equation it can be seen that the second order coefficients are dependent on the the first order contributions. In order to compare the results arrived at by applying these equations with the results of Robb's work with homogeneous achromatic doublets, a GRIN singlet is used as an example. This singlet is comprised of a radial gradient media with two spherical surfaces, with the object at infinity and the aperture stop in contact with the first surface.

The sum of the first order surface contributions for a singlet with its two surfaces denoted A and B is

$$f_{a1} = v_{00,1}[S]$$

$$\left[(y_a i_a)_B - (y_a i_a)_A\right] = [S] = \text{Surface Contribution} \quad . \qquad \text{(B.13)}$$

The corresponding first order transfer contribution is

$$f_{a1}^{*} = 2\left(v_{10,1} - v_{00,1}\frac{N_{10}}{N_{00}}\right)[T]$$

$$[T] = \text{Transfer Integral} \quad , \qquad \text{(B.14)}$$

where the transfer integral consists of integrations over the gradient media of ray heights and angles. The exact form of this factor is not important and will not be given here (see Sands' eq. II (35)). It has been assumed in deriving the above and following equations for the contributions that the chief ray height is zero on both surfaces and that the change in meridional ray height across the gradient region is negligible. These assumptions are based on the the lens being "thin" relative to the focal length and the diameter. The range of validity of this last assumption has been

discussed by Wang[13] and is applicable in this situation. In addition, because index profile is independent of z, $\nu_{ij,k}$ must also be independent of z, and since the variations in meridional ray height are small, so then are the variations in $\nu_{ij,k}$ and it can be factored out of the integrals over the inhomogeneous media.

The form of the second order contributions is quite complex even for a lens with only two surfaces. Another simplification that will be used is based on the assumption that the chromatic coefficients for a gradient are small. This is reasonable under the assumption that the absolute index variation is small compared to one and that the variation in index due to wavelength is even smaller. Measurements carried out in Chapter 6 showed that $\nu_{01,1}$ was on the order of $3 \times 10^{-4}\ \mu m^{-1}$. With this in mind, only terms to first order in chromatic coefficient are retained and the second order surface contribution can be written as

$$f_{a2} = \nu_{00,2}[S] \quad . \tag{B.15}$$

The second order transfer contribution can be written as

$$f^*_{a2} = 2\left[\nu_{10,2} - \nu_{00,2}\frac{N_{10}}{N_{00}}\right][T] \quad . \tag{B.16}$$

It is possible at this point to formulate the conditions under which achromatization will be achieved. The condition for achromatization is

$$F_a = \sum_{k=1}^{m} F_{ak}\omega^k = 0 \quad . \tag{B.17}$$

Using this expression with k=1,2 and substituting in eqs. (B.13) through (B.16), eq. (B.17) can be written in matrix form as

$$\left([S] - 2\frac{N_{10}}{N_{00}}[T] \quad 2[T]\right)\begin{bmatrix}\nu_{00,1} & \nu_{00,2}\\ \nu_{10,1} & \nu_{10,2}\end{bmatrix}\begin{pmatrix}\omega\\ \omega^2\end{pmatrix} = 0 \quad . \tag{B.18}$$

For this to be true at all wavelengths (for all values of ω) it is necessary that the determinant of the chromatic coefficient matrix be equal to zero, ie.,

$$\begin{bmatrix} \nu_{00,1} & \nu_{00,2} \\ \nu_{10,1} & \nu_{10,2} \end{bmatrix} = 0 \quad . \tag{B.19}$$

Alternatively, this can be expressed as

$$\frac{\nu_{00,1}}{\nu_{00,2}} = \frac{\nu_{10,1}}{\nu_{10,2}} \quad . \tag{B.20}$$

This is the same result as that obtained by Robb for homogeneous doublets, with the first element being analogous to the base glass and the second element being analogous to the radial gradient. That this result should parallel its homogeneous counterpart is not entirely surprising considering the work of Ryan-Howard in which the traditional achromatization formulas, adapted slightly for index gradients, were used to predict the performance of gradient-index optics.

The impact of the simplicity eq. (B.20) is more fully realized when the accuracy to which the index profile is represented is taken into account. Using Robb's method, eq. (B.20) is the graphical equivalent of requiring that the points corresponding to the dispersions of the base material and the gradient lie on a straight line through the origin when $\nu_{ij,1}$ is plotted versus $\nu_{ij,2}$ for each material. Materials chosen from such a plot will have perfect wavelength correction, to the extent that their dispersions are represented accurately by $\nu_{ij,1}$ and $\nu_{ij,2}$, and to the extent that the assumptions used in the derivation hold.

To check the validity of this relationship several radial GRIN lenses were designed using the CODEV lens design program. The lenses were singlets and were designed for achromatic imaging in the ultraviolet, from 300 nm to 435 nm, where most materials, even if they transmit in this region, have very nonlinear dispersive

properties. The EFL was 100 mm and the F/no. was 10. No constraints were placed on the values that were used for the index gradient. The optimized achromatic singlets had no axial chromatic aberration within the specified spectral region. The lenses were analyzed at six wavelengths distributed across this spectral region. The chromatic coefficients for the quadratic gradient coefficient (N_{10}) were determined from this data using a least squares fit. The dispersion using this fit for a singlet with a base index of refraction equal to that of BaF_2 is shown in fig. B.3. It can be seen from this figure that the chromatic coordinate representation can be used to very accurately fit the dispersion of the index profile for this type of gradient.

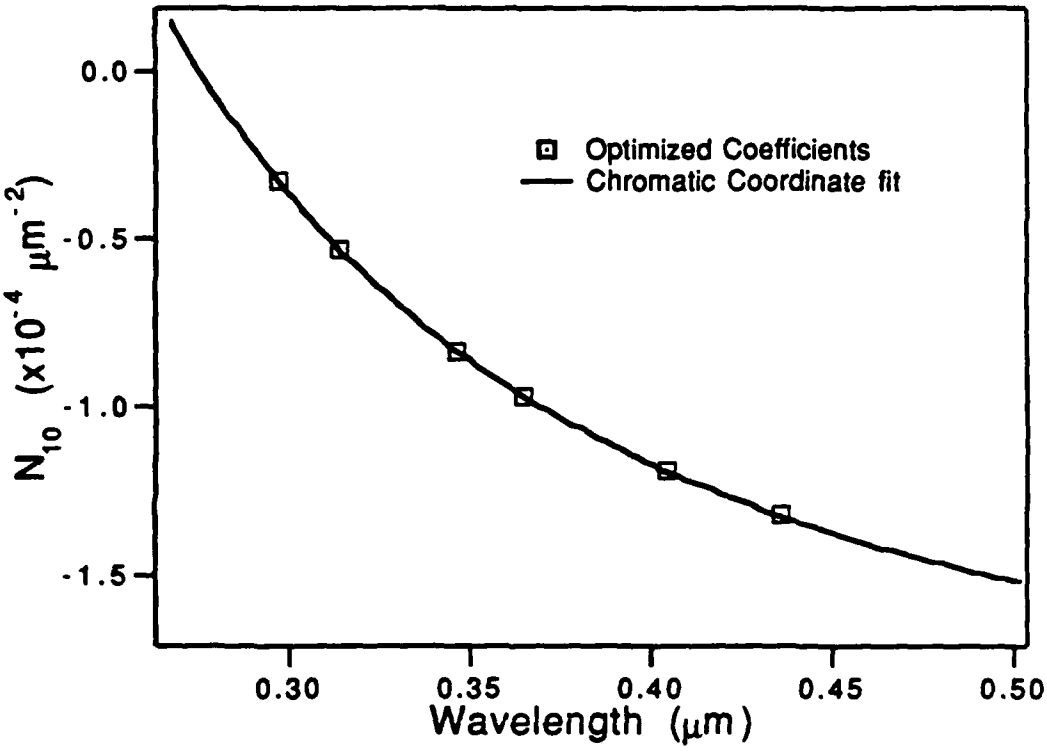

Figure B.3.
Optimized GRIN quadratic coefficients as a function of wavelength for a lens with a thickness of 2 and a focal length of 100.

To verify the relationship between the dispersion of the designed lenses and eq. (B.20), the coefficients were plotted as $\nu_{ij,1}$ versus $\nu_{ij,2}$. This is shown for one lens in figure B.4. The data included in this figure are the base index of refraction (BaF_2) and the coefficients of the fit for N_{10}. As predicted, the coefficients lie along a straight line through the origin. (The values for some coefficients were scaled to make them more easily visible.) As an additional exercise an N_{20} term was added to the gradient and, without allowing the curvatures or N_{10} coefficients to change, the lens was reoptimized to remove spherochromatism. The resultant values for N_{20} as a function of wavelength were fit and their coefficients are also plotted in fig. B.4. Interestingly, this value also lies on a line that includes the base index dispersion and the N_{10} dispersion. It raises some interesting questions but it is beyond the scope of this work to comment further on this.

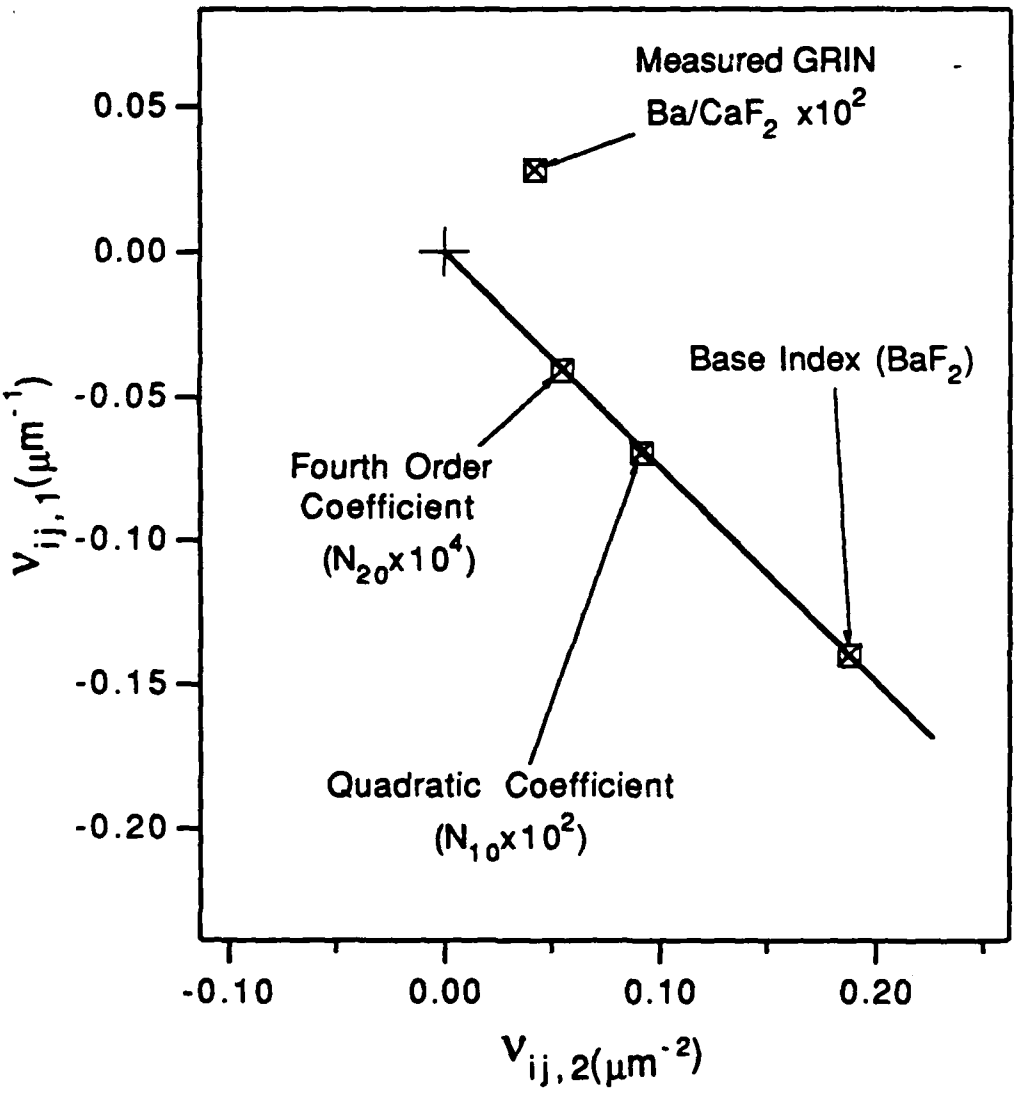

Figure B.4.
Plot of the chromatic coefficients fit to the dispersion of various gradient coefficients for a GRIN achromatic singlet.

The one point included in fig. B.4 that does not lie on a line including the other points is the point representing the chromatic coefficients fit to the measured data for the GRIN fluoride crystals grown for this thesis. In order to predict the usefulness of a material in conjunction with others it is necessary to be able to predict the form that the chromatic coefficients will take as a function of composition.

B.4. Model for GRIN chromatics as a function of composition

Huggins[14] proposes the use of the Gladstone-Dale (G-D) model for predicting the index as a function of composition for optical glasses. This model is a variation of the Lorenz-Lorentz (L-L) model and uses a weighted sum of the constituents of the glass based on their mole proportion and their molar volume. Huggins shows that the G-D model is more accurate than the L-L model for the wide range of silicate glasses he tests. He also applies this model successfully to several oxide crystals. Both the G-D model and the L-L model are used to make predictions of the index of refraction for mixtures of barium fluoride and calcium fluoride. No discernable difference is found between the two models in the predicted curves for index as a function of composition. This is in spite of the expectation that the L-L model, being based on an oscillator model of the medium, would provide a better model for ionic crystals. In light of this and the somewhat simpler form of the G-D model, the G-D model is used in the following discussion. It is expected that results using the L-L model follow these results closely.

The Gladstone-Dale model for a media consisting of several components is

$$N(\rho,z,\lambda)-1=\frac{R(\lambda)}{V}=\frac{\sum_{j=1}^{m}C_j(\rho,z)R_j(\lambda)}{\sum_{j=1}^{m}C_j(\rho,z)V_j} \qquad (B.21)$$

where for constituent j, R_j is the "molar refractivity", V_j is the molar volume, and $C_j(\rho,z)$ is its percent concentration as a function of the radial and axial coordinates, ρ and z, respectively.

Expanding eq. (B.21) for a two component system, where the subscripts Ba and Ca refer to BaF_2 and CaF_2, respectively, the index can be written as

$$N(\rho,z,\lambda) = 1 + \frac{R_{Ba}(\lambda) + C_{Ca}(\rho,z)\left(R_{Ca}(\lambda) - R_{Ba}(\lambda)\right)}{V_{Ba} + C_{Ca}\left(V_{Ca} - V_{Ba}\right)} \tag{B.22}$$

The molar refractivity for the two fluorides can be replaced by (from eqs. (B.7) and (B.21))

$$R_{Ba}(\lambda) = \left(N(\lambda) - 1\right)V_{Ba} = \left[N_{Ba} + \nu_{Ba,1}\omega(\lambda) + \nu_{Ba,2}\omega(\lambda)^2 - 1\right]V_{Ba} \tag{B.23}$$

where the only wavelength dependence is in the chromatic coordinate, ω, while N_{Ba} and N_{Ca} are the indices of refraction evaluated at the reference wavelength.

The change in index relative to the base index, or Δn (delta-n), is defined here as

$$\Delta n(\rho,z,\lambda) = N(\rho,z,\lambda) - N(0,0,\lambda) \tag{B.24}$$

Assuming that the base index is that of BaF_2, by substituting eqs. (B.22) and (B.23) into eq. (B.24) the delta-n can be written as

$$\Delta n(\rho,z,\lambda) = \frac{C_{Ca}(\rho,z)V_{Ca}}{V}\left[\left(N_{Ca} - N_{Ba}\right) + \left(\nu_{Ca,1} - \nu_{Ba,1}\right)\omega(\lambda) + \left(\nu_{Ca,2} - \nu_{Ba,2}\right)\omega(\lambda)^2\right] \tag{B.25}$$

where V represents the denominator in eq. (B.22).

From eq. (B.25) it can be seen that the delta-n takes the same form as it does for the homogeneous representation, ie. the delta-n can be represented as a base index plus a polynomial in ω. Furthermore, the coefficients of the polynomial in ω are scaled linear combinations of the coefficients of the base glasses, and the only dependence on position is in a multiplicative factor of the whole expression. Figure B.5 shows a plot of the delta-n as a function of composition for a wavelength of 632.8 nm. This

functional form was used to convert the electron microprobe (concentration) data into index data for direct comparison with Mach-Zehnder data. (see Chapter 4, figs.4.4a-4.4c.)

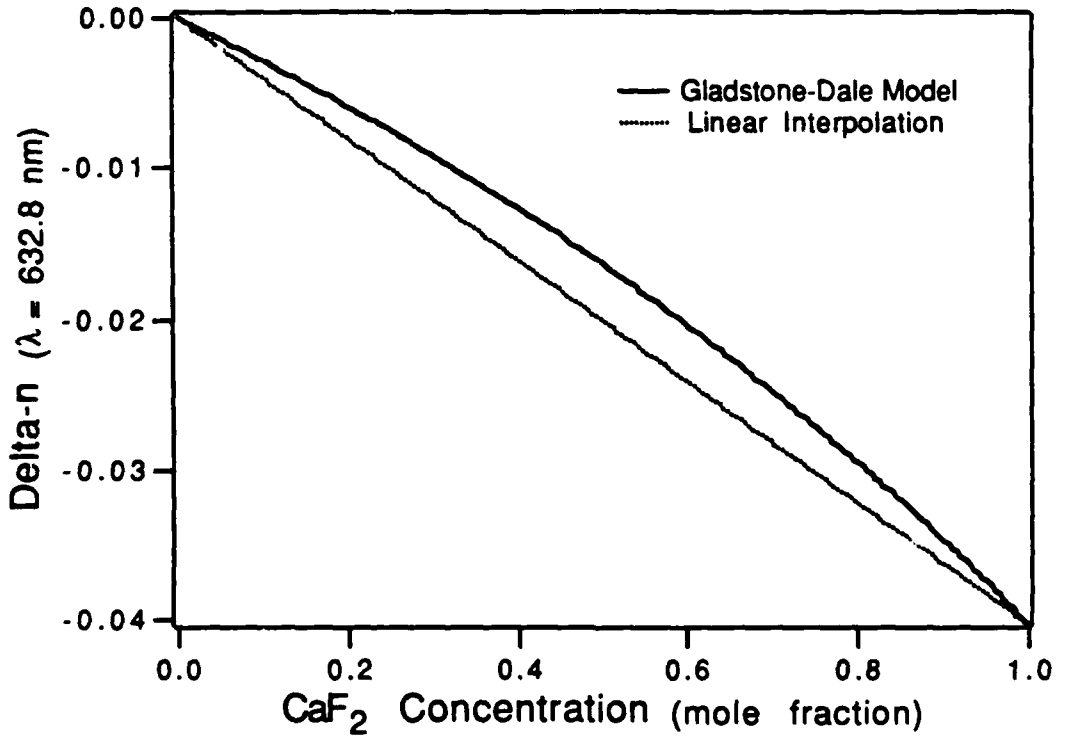

Figure B.5.
Comparison of the Gladstone-Dale model and a linear interpolation. The difference between the G-D model and a Lorentz-Lorenz model was less than 1.5 % in delta-n.

B.5. Conclusions

Several conclusions can be drawn from the above derivations. The first is that a gradient V number, defined as the ratio of a linear combination of delta-n's at different wavelengths, is independent of position. This is born out experimentally[15] for some ion-exchanged glasses, and qualitatively by the measurements made during the course of this thesis research and presented in Chapter 6. In general it is expected that for any GRIN material for which the delta-n can be expressed as a linear function of the indices

of its constituents the gradient V number is a constant. While this is not shown above, the derivation of this generalization follows the same form as for the explicit G-D example given here. With respect to the graphical method of Robb for choosing achromatizing combinations of glasses, the above equations show that the ratio of $v_{ij,1}$ to $v_{ij,2}$ for GRIN materials is independent of composition.

The second conclusion that can be arrived at is that when a chromatic coordinate representation accurately describes the wavelength dependence of the homogeneous components of a GRIN media, which in turn has an index that is a linear function of composition, then a chromatic coordinate representation also accurately describes the GRIN media.

References for Appendix B.

---

[1]M. Herzberger and N. McClure, "The Design of Superachromatic Lenses," Appl. Opt. **2** (1963) 533.

[2]*Optical Glass Catalog*, Schott Glass Technologies, Inc., Duryea, Pa.

[3]G. W. Forbes, "Chromatic Coordinates in Aberration Theory," JOSA A **1** (1984) 344.

[4]G. W. Forbes, "Weighted Truncation of Power Series and the Computation of Chromatic Aberration Coefficients," JOSA A **1** (1984) 350.

[5]P. N. Robb and R. I. Mercado, "Calculation of Refractive Indices Using Buchdahl's Chromatic Coordinate," Appl. Opt. **22** (1983) 1198.

[6]*Handbook of Chemistry and Physics*, 57th Ed., CRC Press, Cleveland, OH (1977) 7-83.

[7]Harshaw Crystal Optics, Data Booklet, Englehard Corp., (1988)

[8]P. N. Robb, "Selection of Optical Glasses. 1: Two Materials," Appl. Opt. **24** (1985) 1864. (See also R. Sigler, "Glass Selection for Airspaced Apochromats using the Buchdahl Dispersion Equation," Appl. Opt. **25** (1986) 4311.)

[9]H. A. Buchdahl, "Many-color Correction of Thin Doublets," Appl. Opt. **24**, (1985) 1878.

[10]P. J. Sands, "Inhomogeneous Lenses, II. Chromatic Paraxial Aberrations," JOSA **61** (1971) 777.

[11]P. J. Sands, "Inhomogeneous Lenses, V. Chromatic Paraxial Aberrations of Lenses with Axial or Cylindrical Index Distributions," JOSA **61** (1971) 1495.

[12]D. T. Moore and P. J. Sands, "Third-Order Aberrations of Inhomogeneous Lenses with Cylindrical Index Distributions," JOSA **61** (1971) 1195.

[13]D. Wang, "Third Order Aberration Theory for Weak Gradient-Index Lenses," submitted for publication to Appl. Opt. (1990).

[14]M. Huggins, "The Refractive Index of Silicate Glasses as a Function of Composition," JOSA **30** (1940) 495.

[15]D. S. Kindred, University of Rochester, private communication.